

Investigations of the asymptotic suction  
boundary layer

by

Jens H. M. Fransson

September 2001  
Technical Reports from  
Royal Institute of Technology  
Department of Mechanics  
SE-100 44 Stockholm, Sweden

Akademisk avhandling som med tillstånd av Kungliga Tekniska Högskolan i Stockholm framlägges till offentlig granskning för avläggande av teknologie licentiatexamen torsdagen den 27:e september 2001 kl. 10.15 i seminarierum 40, Teknikringen 8, KTH, Stockholm.

©Jens H. M. Fransson 2001

Unversitetsservice US AB, Stockholm 2001

## Investigations of the asymptotic suction boundary layer.

**Jens H. M. Fransson 2001**

Department of Mechanics, Royal Institute of Technology  
SE-100 44 Stockholm, Sweden

### Abstract

An experimental and theoretical study on the effect of boundary layer suction on the laminar-turbulent transition process has been carried out. Both experiments on the development of Tollmien-Schlichting (TS) waves and boundary layer disturbances introduced by free stream turbulence were carried out. In the study an asymptotic suction boundary layer was established in a wind tunnel. Uniform suction was applied over a large area and the boundary layer was nearly constant over a length of 1800 mm. Measurements were made both with and without suction so comparisons between the two cases could easily be made. Measurements of the development of the mean velocity distribution showed good agreement with theory. In connection to the TS-wave experiments spatial linear stability calculations, where the wall-normal velocity component is accounted for, were carried out for comparison with the experiments. This comparison shows satisfactory agreement even though the stability of the asymptotic suction profile is somewhat overpredicted by the theory. Free stream turbulence was generated by three different grids giving turbulence intensities at the leading edge of the plate between 1.4 % and 4.0 %. The free stream turbulence induces disturbances into the boundary layer and it was shown that for the suction case the disturbance level inside the boundary layer saturates at a level which is proportional to the free stream turbulence intensity. In all cases transition was prevented when suction was applied although without suction the two highest levels of grid turbulence gave rise to transition. Despite a twofold reduction in the boundary layer thickness in the suction case compared to the no suction case the spanwise scale of the streaky structures was almost constant.

**Descriptors:** asymptotic suction boundary layer, laminar-turbulent transition, Tollmien-Schlichting waves, free stream turbulence



# Contents

<b>Abstract</b>	iii
<b>Chapter 1. Introduction</b>	1
1.1. Laminar-turbulent transition scenarios	2
1.2. Previous work on suction	3
<b>Chapter 2. Boundary layer evolution and stability concepts</b>	6
2.1. Governing equations	6
2.2. Boundary layer equations	7
2.3. Evolution equation	8
2.4. Stability equations	9
2.5. Numerical methods	14
2.6. Theoretical results	16
2.7. Model problem	29
<b>Chapter 3. Experimental design and set-up</b>	38
3.1. Leading edge	38
3.2. Porous material	42
3.3. Plate construction	45
3.4. Experimental set-up	47
3.5. Measurement techniques	49
<b>Chapter 4. Experimental results</b>	51
4.1. TS-waves in a Blasius boundary layer	52
4.2. TS-waves in an asymptotic suction boundary layer	62
4.3. Free stream turbulence experiments	73
<b>Chapter 5. Summary</b>	92
<b>Appendix A. Inaccurate determination of the shape factor</b>	94

vi CONTENTS

A.1.	Effect of inaccurate determination of the wall position	94
A.2.	Effect of inaccurate determination of the free stream velocity	95
<b>Appendix B.</b>	<b>Active turbulence generating grid</b>	97
B.1.	Design	97
B.2.	Characteristic data of the active grid	98
<b>Acknowledgment</b>		107
<b>References</b>		108
<b>Paper 1.</b>	<b>Growth and breakdown of streaky structures in boundary layer transition induced by free stream turbulence</b>	113
<b>Paper 2.</b>	<b>Errors in hot-wire X-probe measurements induced by unsteady velocity gradients</b>	123



## CHAPTER 1

# Introduction

Fluid dynamics is encountered in many industrial applications which makes it highly interesting as a research area. One area of significant interest is the aerodynamic performance of aircrafts in general and laminar flow control (LFC) in particular. LFC is usually associated with uniform suction and a definition of this control method is given in Joslin (1998), where it is pointed out that LFC is a method to delay the laminar-turbulent transition and not to relaminarize the flow. The energy cost is typically one order of magnitude higher in the latter case, which makes the definition appropriate since the optimal performance is not obtained (as one may believe) when the suction completely absorbs the boundary layer. The more suction that is used the steeper becomes the velocity gradient in the boundary layer implying an increase in skin-friction. Therefore, the balance between keeping the flow laminar and keeping a low energy consumption is actually the optimal performance. In optimal control theory there is always a cost function present that is to be minimized.

This thesis is a work on the laminar-turbulent transition scenario on a flat plate boundary layer when uniform suction through the surface is applied. A special case is when the so called asymptotic suction profile is obtained. This flow condition is obtained at some distance downstream the leading edge of a flat plate when uniform suction is applied over a large area. An interesting feature is that an analytic solution of the uniform suction problem may be derived from the boundary layer equations resulting in an exponential profile (the asymptotic suction profile). The suction has a similar influence on the profile as a favorable pressure gradient and makes the profile in the fully developed asymptotic region much more stable than the Blasius profile.

The asymptotic boundary layer flow has been dealt with extensively in text books, see for instance Schlichting (1979), and the theory for the mean flow is straightforward. One can easily show that the boundary layer profile  $u(y)$  becomes

$$u/U_\infty = 1 - e^{-yV_0/\nu}$$

where  $U_\infty$ ,  $V_0$  and  $\nu$  are the constant free stream velocity, the suction velocity and the kinematic viscosity, respectively. This expression was first derived by Griffith and Meredith (1936) according to both Crabtree *et al.* (1963)

and Schlichting (1979). The asymptotic boundary layer thickness can be shown to be directly proportional to  $\nu/V_0$ . The Reynolds number ( $R_\delta$ ) based on the boundary layer thickness ( $\delta$ ) can then be shown to be proportional to

$$R_\delta \sim U_\infty/V_0.$$

To obtain the stability characteristics of the suction boundary layer the normal velocity component of the mean flow, i.e. the suction velocity at the wall, can be incorporated in the disturbance equation and this gives a slightly modified Orr-Sommerfeld equation. Also the boundary condition of the normal fluctuation velocity, due to pressure fluctuations above a porous plate, need to be considered. This gives rise to an additional equation that has to be satisfied at the wall, but which reduces to the standard boundary condition in the limit when the permeability approaches zero, see Gustavsson (2000). Hocking (1975) showed that the critical Reynolds number for two-dimensional waves increases with two orders of magnitude as compared to the Blasius boundary layer.

## 1.1. Laminar-turbulent transition scenarios

### 1.1.1. Tollmien-Schlichting wave dominated transition

For low environmental disturbances the transition scenario from laminar to turbulent flow on a flat plate boundary layer is rather well understood. This class of transition starts with instability waves that are generated in the receptivity process taking place close to the leading edge. The initial growth of these waves may be described by Fourier modes, which when implemented into the linear stability equation gives rise to the well known Orr-Sommerfeld equation. These waves grow/decay exponentially in space and the least stable mode (which according to *Squire's theorem* always is two-dimensional) is called a Tollmien-Schlichting (TS) wave. For high enough amplitude of a TS-wave, roughly 1% of the free stream velocity, three-dimensional waves and vortex formations develops (still laminar) that causes the appearance of turbulent spots which joins and brings the whole flow into a fully turbulent one. The first successful windtunnel experiment on TS-waves was carried out and reported by Schubauer & Skramstad (1948). However, these results were not in fully agreement with theory and for long the discrepancy between linear parallel stability (LPT) theory and experiments were believed to be due to the non-parallel effect of a growing boundary layer. However, this effect turned out to be very small (see e.g. Fasel & Konzelmann (1990)) and a final experiment putting an end to the discussion was carried out by Klingmann *et al.* (1993), who with a special designed asymmetric leading edge (in order get rid of the appearing pressure suction peak) could show good agreement with LPT. Well described guidelines for performing a successful TS-wave experiment in a windtunnel was put forward by Saric (1994).

### 1.1.2. *By-pass transition and streaky structure*

It is well known that for the Blasius boundary layer free stream turbulence induces disturbances into the boundary layer which give rise to streamwise oriented structures of low and high speed fluid (see e.g. Kendall (1985), Westin (1997), Jacobs & Durbin (2001) and Matsubara & Alfredsson (2001) and paper 1 of the present thesis for thorough investigations of such a flow). These structures grow in amplitude and establish a spanwise size which is of the order of the boundary layer thickness far away from the leading edge. When the streaks reach a certain amplitude they break down to turbulence, probably through a secondary instability mechanism (see e.g. Andersson *et al.* (2001)). This type of boundary layer transition was denoted as by-pass transition by Morkovin (1969) since it is a relatively rapid process by-passing the traditional TS-wave dominated transition process resulting in breakdown to turbulence at subcritical Reynolds numbers when compared with the predicted value by traditional theory. Nonlinear theories were tested (see e.g. Orszag & Patera (1983)) in order to find a theory that matched experimental results. However, the nonlinear terms of the Navier-Stokes equation can be shown not to be part of the growth mechanism (see Drazin & Reid (1981)). The mechanism that today is believed to govern this type of transition scenario is the transient growth. An explanation of this mechanism is given in e.g. Schmid & Henningson (2001) and arises due to the non-orthogonality of the Orr-Sommerfeld and Squire eigenmodes. Superposition of such decaying modes may first experience an algebraic growth followed by an exponential decay, denoted as transient growth. The "lift-up" mechanism proposed by Landahl (1980) is the cornerstone contributing to the algebraic growth in the study of transient growth. Small perturbations in the wall-normal direction induces large disturbances in the streamwise direction due to the lift-up of low speed velocity that originally maintains its horizontal momentum. The presence of viscosity will eventually damp the growth and finally make the disturbance decay. Some recent publications on the by-pass transition and the transient growth mechanism are given below; Luccini (2000), Reshotko (2001), and Andersson *et al.* (2001).

## 1.2. Previous work on suction

Experimental work on the asymptotic suction boundary layer has to some extent been done earlier, but mainly devoted to determination of the mean flow (see Schlichting (1979) and references therein). TS-wave as well as FST experiments in a fully asymptotic suction boundary layer, that will be presented in this thesis, have not been carried out earlier. However, in connection to drag reduction experiments (by means of LFC) suction through spanwise slots, porous panels and discrete holes have been carried out (see e.g. Pfenninger & Groth (1961), Reynolds & Saric (1986), and MacManus & Eaton (2000), respectively). A general review of various types of surface and of the results achieved in wind tunnel tests is given by Gregory (1961), where pros and cons

for practical applications on aircrafts are discussed. The flow characteristics through laser drilled titanium sheets were investigated by Poll *et al.* (1992*b*) and was shown to be laminar, incompressible and pipe like. Poll *et al.* (1992*a*) conducted a cylinder experiment made of a similar laser drilled titanium sheet. The effect of suction was found to have a powerful effect upon cross-flow induced transition. An interesting result by MacManus & Eaton (2000), who both performed an experimental and an computational investigation on the flow physics of discrete boundary layer suction, shows that the suction may destabilize the flow by introduction of co-rotating streamwise vortices when suction is applied through discrete holes. However, the investigated ratios of the perforation diameter to the displacement thickness ( $d/\delta_1$ ) was quite large, around unity.

Applying suction uniformly over a large area may not be the optimal way of performing active control practically, since the energy consumption becomes relatively high. Another approach would be to use selective suction to control the growth of unstable fluctuations. This type of control must be done on a detectable parameter, such as e.g. low speed streaks. The appearance of streaks with alternate low and high speed velocity observed in a laminar boundary layer subjected to high levels of free stream turbulence are also found in the near-wall region of a turbulent boundary layer. Together with the intermittent bursts or turbulence production events these are ususally referred to as coherent structures. Controlled experiments have been performed, see e.g. Myose & Blackwelder (1995) and Lundell (2000), in order to reduce the instability and delay the breakdown of the low speed streaks in laminar flows. Myose & Blackwelder (1995) achieved successful control on the breakdown of Görtler vortices, by pointwise suction of low speed momentum from the low speed streak and in that manner delay the transition by producing a fuller profile in the normal direction and by eliminating the difference between low and high speed regions in the spanwise direction. A similar technique was used by Lundell (2000) who generated streaks in a plane channel flow by applying suction through streamwise slots. Secondary instabilities were then forced randomly by speakers and was then successfully controlled by localized suction some distance downstream.

#### 1.2.1. *Present work*

In chapter 2 the boundary layer equations for the evolution of the asymptotic suction boundary layer is derived as well as the stability equations when the normal velocity is taken into account. Some stability results are given for the asymptotic boundary layer as well as for a model problem consisting of a channel with two porous walls with suction and blowing respectively. The design philosophy of the leading edge of the experimental plate is described in chapter 3 together with characterization of the porous material and the detailed construction of the flat plate. In chapter 4 the experimental results are given both for the Blasius flow above the porous plate and the streamwise base flow of

the suction case as well as the corresponding TS-waves results. Furthermore, results of the disturbance evolution in both the no suction and suction cases are given and compared in detail. It is clearly shown that suction dramatically can change the disturbance growth rate and that transition to turbulence can be prevented. Appendix A gives an error analysis of the determination of the boundary layer parameters, whereas appendix B gives a thorough description of the active grid which is used to generate free stream turbulence in the experiments. Also included is paper 1 which describes free stream turbulence induced disturbances in a Blasius boundary layer and paper 2 where some problems associated with X-probe measurements in flows with strong unsteady spanwise velocity gradients.

## CHAPTER 2

### Boundary layer evolution and stability concepts

This chapter will give some theoretical background to boundary layers over a porous surface with continuous suction. Both the mean flow field as well as small finite wave disturbances will be studied. Starting from the governing equations the boundary layer evolution equation from the Blasius- to the asymptotic suction profile will be derived. From the boundary layer equations one can derive an analytic expression of the asymptotic suction profile, which turns out to be exponential. The suction has the same influence on the profile as a favorable pressure gradient and makes it in the fully developed asymptotic region much more stable than the Blasius profile. Derivation of the classical linearized stability equations together with a modified version, where the assumption of strictly parallel flow is not needed, will be performed. Some features of the asymptotic suction profile and numerical results regarding the mean flow evolution and stability will then be discussed. The chapter will end with a model problem, where the effect of a continuous cross flow in a plane Poiseuille flow will be analysed.

#### 2.1. Governing equations

The governing equations describing an incompressible flow are based on the conservation of mass and momentum. The second set of equations are known as the Navier-Stokes equations, i.e. the momentum equation, which together with the continuity equation (conservation of mass) constitutes a complete set of equations giving us a full description of the flow of motion. When written by use of Einsteins summation convention in dimensional form the continuity and the momentum equations read

$$\frac{\partial u_i^*}{\partial x_i^*} = 0, \quad (2.1)$$

$$\frac{\partial u_i^*}{\partial t^*} + u_j^* \frac{\partial u_i^*}{\partial x_j^*} = -\frac{1}{\rho} \frac{\partial p^*}{\partial x_i^*} + \nu \frac{\partial^2 u_i^*}{\partial x_j^{*2}}, \quad (2.2)$$

where  $u_i^*$  is the  $i$ :th component of the velocity vector,  $x_i^*$  is the  $i$ :th component of the space vector,  $p^*$  the pressure,  $\rho$  the density and  $\nu$  the kinematic viscosity.

## 2.2. Boundary layer equations

In a steady two-dimensional flow over a flat surface where the assumption that variations normal to the surface are much larger than those along the plate is fulfilled, further simplifications can be made and we end up with the boundary layer equations. This assumption reads  $|\frac{\partial u}{\partial x}| \ll |\frac{\partial u}{\partial y}|$  and implies that  $\delta \ll L$ , where  $\delta$  and  $L$  are the wall-normal and streamwise length scales respectively. From the streamwise momentum equation dimensional analysis reveals that this condition is satisfied for large Reynolds numbers. A well studied flow case is the zero pressure gradient boundary layer ( $\frac{dp}{dx} = 0$ ) and what then is left of equations (2.1) and (2.2) are simply

$$\frac{\partial u^*}{\partial x^*} + \frac{\partial v^*}{\partial y^*} = 0, \quad (2.3)$$

$$u^* \frac{\partial u^*}{\partial x^*} + v^* \frac{\partial u^*}{\partial y^*} = \nu \frac{\partial^2 u^*}{\partial y^{*2}}, \quad (2.4)$$

where  $u^*$  and  $v^*$  are the streamwise and wall-normal velocity components whereas  $x^*$  and  $y^*$  are the corresponding space directions. For a boundary layer flow over a solid surface the no-slip condition has to be fulfilled at the surface and the free stream velocity has to be reached by the streamwise velocity component outside the boundary layer. These boundary conditions are mathematically written as

$$y^* = 0 : \quad u^* = v^* = 0 \quad \text{and} \quad y^* \rightarrow \infty : \quad u^* \rightarrow U_\infty. \quad (2.5)$$

### 2.2.1. Boundary layer properties

The characteristics of the mean velocity profile are of great importance since information such as separation, wall friction, stability features, laminar or turbulent flow can be achieved simply from the shape of the velocity profile. Hence, measures of the scale and shape is appropriate. According to the second boundary condition of equation (2.5)  $u^*$  reaches  $U_\infty$  asymptotically as  $y^* \rightarrow \infty$ . In practice this limit is finite and the boundary layer thickness ( $\delta$ ) is usually defined as the distance from the surface where  $\frac{u^*}{U_\infty} = 0.99$ . For experimentalists this definition is not precise enough to be used as the boundary layer scale since difficulties in determining  $\delta$  will appear due to the fact that  $\frac{du^*}{dy^*}$  is small in that region.

Since the governing equations of motion (2.1) and (2.2) are based on the conservation of mass and momentum it would be natural to involve these physical quantities when defining boundary layer scales. A further aspect when looking for proper scaling would be the viscosity, since without it the boundary layer would not be present. Keeping these arguments in mind the following two well known scale definitions are not surprisingly

$$\text{displacement thickness} \quad \delta_1 = \int_0^\infty \left[ 1 - \frac{u^*(y)}{U_\infty} \right] dy, \quad (2.6)$$

$$\text{momentum thickness} \quad \delta_2 = \int_0^\infty \frac{u^*(y)}{U_\infty} \left[ 1 - \frac{u^*(y)}{U_\infty} \right] dy. \quad (2.7)$$

These scales correspond to the distance the surface has to be moved towards the free stream in order to maintain the same flux of mass and momentum, respectively, in the inviscid flow case compared to the viscous case. The ratio between these two length scales is called the shape factor ( $H_{12}$ ) and is a non-dimensional quantity that exposes the shape of the velocity profile,

$$H_{12} = \frac{\delta_1}{\delta_2}. \quad (2.8)$$

The calculation of equations 2.6 and 2.7 using experimental data is sensitive for small changes regarding the wall position as well as the free stream velocity. In order to estimate the accuracy an error analysis on these length scales with a Blasius profile as reference is given in Appendix A.

In turbulent boundary layers other scales are used complementary, such as the viscous- or ‘wall-region’ scales. These are determined by the wall friction and kinematic viscosity, which are the leftovers when a simple analysis with no-slip condition is applied to the governing equation. The viscous velocity and length scales are used to scale the dimensional quantities to what is known as the (+)-units and are defined as

$$u_\tau = \sqrt{\frac{\tau_w}{\rho}}, \quad \text{and} \quad \ell = \frac{\nu}{u_\tau}, \quad (2.9)$$

where  $\tau_w$  is the wall shear stress defined as  $\tau_w = \mu \left( \frac{\partial u^*}{\partial y^*} \right)_{y=0}$ .

### 2.3. Evolution equation

When suction is applied over a large area the well known asymptotic suction profile will be reached after some evolution region. If an impermeable area is considered from the leading edge to where the suction starts the boundary layer will be allowed to grow and a Blasius velocity profile will be developed for a zero pressure gradient flow. During the evolution region the profile will then undergo a transformation from the Blasius state to the asymptotic suction state. This spatial evolution can from a simple approach be described through a non-dimensional evolution equation. The first step is to introduce an indirect

$x$ - and  $y$ -dependent stream function according to

$$\psi = \sqrt{\nu x U_\infty} f(\xi, \eta), \quad (2.10)$$

where

$$\xi = x \frac{V_0}{U_\infty} \sqrt{\frac{U_\infty}{\nu x}}; \quad \eta = y \sqrt{\frac{U_\infty}{\nu x}}. \quad (2.11)$$

The streamwise and normal velocity components are recovered through

$$u(\eta) = U_\infty \frac{\partial f}{\partial \eta} \quad \text{and} \quad v(\eta) = \sqrt{\frac{U_\infty \nu}{4x}} \left( \eta \frac{\partial f}{\partial \eta} - \xi \frac{\partial f}{\partial \xi} - f \right),$$

respectively. When applied to the boundary layer equations (2.3) and (2.4) we get the following third order non-linear partial differential equation

$$\frac{\partial^3 f}{\partial \eta^3} + \frac{1}{2} f \frac{\partial^2 f}{\partial \eta^2} + \frac{1}{2} \xi \left( \frac{\partial f}{\partial \xi} \frac{\partial^2 f}{\partial \eta^2} - \frac{\partial f}{\partial \eta} \frac{\partial^2 f}{\partial \eta \partial \xi} \right) = 0, \quad (2.12)$$

with the corresponding boundary conditions

$$\left. \begin{array}{l} f = \xi \text{ (suction)} \\ \frac{\partial f}{\partial \eta} = 0 \text{ (no-slip)} \end{array} \right\} \text{ at } \eta = 0 \quad \text{and} \quad \frac{\partial f}{\partial \eta} \rightarrow 1 \text{ as } \eta \rightarrow \infty. \quad (2.13)$$

The first solution from such an evolution equation with an impermeable entry length was obtained by Rheinboldt (1956) through series expansion. The ansatz of a stream function and non-dimensionalized variables for deriving the evolution equation are not to be confused with similarity solutions. The stream function is dependent on two variables and becomes ‘similar’ when the asymptotic suction state is reached.

From an experimentalists point of view important information can be obtained when solving the evolution equation. For a wind tunnel experiment on the asymptotic suction boundary layer there are a number of parameters that has to be chosen correctly relative to each other in order to achieve the asymptotic suction boundary layer within the restriction of a finite test section.

## 2.4. Stability equations

The Reynolds number ( $R$ ) defined as the ratio of a characteristic velocity times a characteristic length to the viscosity may also be seen as the ratio of the inertia term to the viscosity term in most flow cases. When viscosity is absent the viscous term disappears, i.e. goes to zero, which would imply that  $R \rightarrow \infty$ . This is the inviscid flow case, governed by Eulers equations, and should be

approached for successively increased  $R$  from the Navier-Stokes equations. A non-dimensional form of the equations would therefore be convenient since the limiting form then becomes clear.

At this state the non-dimensionalizing quantities do not need to be specified, and when equations (2.1) and (2.2) are scaled according to

$$x_i = \frac{x_i^*}{l^*}; \quad u_i = \frac{u_i^*}{U^*}; \quad p = \frac{p^*}{\rho U^{*2}}; \quad t = \frac{t^* U^*}{l^*};$$

where (\*) denotes dimensional quantities and  $l^*$  and  $U^*$  are characteristic length and velocity scales, respectively, the following non-dimensional form of the Navier-Stokes equations are obtained

$$\frac{\partial u_i}{\partial x_i} = 0, \quad (2.14)$$

$$\frac{\partial u_i}{\partial t} + u_j \frac{\partial u_i}{\partial x_j} = -\frac{\partial p}{\partial x_i} + \frac{1}{R} \frac{\partial^2 u_i}{\partial x_j^2}, \quad (2.15)$$

and the Reynolds number ( $R$ ) is

$$R = \frac{U^* l^*}{\nu}.$$

The linearized disturbance equations are derived by superposing small perturbations onto the base flow, i.e. letting  $u_i = U_i + u'_i$ . Here  $u'_i$  and  $U_i (= \bar{u}_i)$  denotes the perturbation term and the base flow, respectively. After subtracting the solution of the base flow and neglecting non-linear terms we end up with the linearized stability equations

$$\frac{\partial u'_i}{\partial x_i} = 0, \quad (2.16)$$

$$\frac{\partial u'_i}{\partial t} + u'_j \frac{\partial U_i}{\partial x_j} + U_j \frac{\partial u'_i}{\partial x_j} = -\frac{\partial p}{\partial x_i} + \frac{1}{R} \frac{\partial^2 u'_i}{\partial x_j^2}. \quad (2.17)$$

Making the assumption of a parallel base flow along the surface in the stream-wise direction which only depends on the wall-normal distance, i.e.  $U = U(y)$  and taking the divergence of the three component momentum equations the pressure can be derived as

$$\nabla^2 p = -2 \frac{dU}{dy} \frac{\partial v}{\partial x}, \quad (2.18)$$

where we in the following have omitted the primes on the fluctuating quantities. When this expression for the pressure is replaced in the momentum equation for  $v$  we obtain

$$\left[ \left( \frac{\partial}{\partial t} + U \frac{\partial}{\partial x} \right) \nabla^2 - U'' \frac{\partial}{\partial x} - \frac{1}{R} \nabla^4 \right] v = 0, \quad (2.19)$$

where  $(\prime)$  from now on denotes differentiation with respect to  $y$ . Now, having the disturbance equation for  $v$  it would be interesting to see if for any initial velocity distribution there exists an indefinitely growing perturbation. But instead of considering all possible perturbations we restrict ourselves to one single disturbance wave at a time, which simplifies the problem. We assume the following ansatz for the wave disturbances (normal mode hypothesis)

$$q_i = \hat{q}_i(y) e^{i(\alpha x + \beta z - \omega t)}, \quad (2.20)$$

where  $\bar{q} = (u, v, w, p)$ . Here,  $\omega$  is the angular frequency and  $\alpha$  and  $\beta$  denote the streamwise and spanwise wavenumber, respectively, which together defines the overall wavenumber ( $k$ ) as  $k^2 = \alpha^2 + \beta^2$ . Implemented in equation (2.19) we obtain the well known Orr-Sommerfeld equation

$$\left[ (-i\omega + i\alpha U)(\mathcal{D}^2 - k^2) - i\alpha U'' - \frac{1}{R}(\mathcal{D}^2 - k^2)^2 \right] \hat{v} = 0, \quad (2.21)$$

where  $\mathcal{D}$  is differentiation with respect to  $y$ . The remaining two components ( $u$  and  $w$ ) of the linearized stability equation (2.17) are used to obtain a second equation through the definition of the normal vorticity  $\eta = \frac{\partial u}{\partial z} - \frac{\partial w}{\partial x}$ , which in Fourier components are written

$$\hat{\eta} = i\beta \hat{u} - i\alpha \hat{w}, \quad (2.22)$$

resulting in the Squire equation

$$\left[ (-i\omega + i\alpha U) - \frac{1}{R}(\mathcal{D}^2 - k^2) \right] \hat{\eta} = i\beta U' \hat{v}. \quad (2.23)$$

The no-slip condition, mentioned earlier in this section, delivers conditions both about the vorticity and the first derivative of the wall-normal perturbation at the wall. Further conditions widely used is that all perturbations vanishes at a surface and in the free stream far from the surface. The continuity equation

(2.16) expressed in Fourier components read

$$i\alpha\hat{u} + D\hat{v} + i\beta\hat{w} = 0, \quad (2.24)$$

and together with equation (2.22) and the physical boundary conditions discussed above the following boundary conditions can be stated

$$\hat{v} = D\hat{v} = \hat{\eta} = 0 \quad (2.25)$$

and should be fulfilled both at the surface and far from the boundary layer edge.

The streamwise and spanwise perturbations are obtained through equations (2.22) and (2.24), resulting in functions of the vorticity ( $\hat{\eta}$ ) and the first derivative of the wall-normal perturbation ( $D\hat{v}$ ) as

$$\hat{u} = \frac{i}{k^2} (\alpha D\hat{v} - \beta\hat{\eta}), \quad (2.26)$$

$$\hat{w} = \frac{i}{k^2} (\beta D\hat{v} - \alpha\hat{\eta}). \quad (2.27)$$

Note that so far no choice of the non-dimensionalizing scales is made nor any choice of the character of the problem, i.e. if the evolution will be regarded as temporal or spatial. In the former case the eigenvalue problem consisting of equations (2.21), (2.23) and (2.25) are solved for  $\omega \in \mathbb{C}$  or alternately for  $c = \omega/\alpha$ , being the phase velocity, and  $\alpha, \beta \in \mathbb{R}$ . In the latter case one solves for  $\alpha \in \mathbb{C}$  for given values of  $\omega, \beta \in \mathbb{R}$ , which is somewhat more challenging since the eigenvalue appears as a fourth power in equation (2.21) instead of a first as for the temporal case. The spatial evolution is nevertheless the preferred one since comparisons with experiments are straightforward. The non-dimensional frequency ( $F$ ) is often used by experimentalists and is defined as

$$F = \frac{2\pi f\nu}{U_\infty^2} \times 10^6. \quad (2.28)$$

#### 2.4.1. Modified Orr-Sommerfeld and Squire equations

When deriving the Orr-Sommerfeld and Squire equations, (2.21) and (2.23) respectively, the assumption of parallel flow is made. This assumption may be argued to hold for a continuous suction case where the mean wall-normal velocity component ( $\bar{V}$ ) is constant. In order to neglect the  $V$ -component the suction rate has to be small. However, if the length scale is chosen to be the displacement thickness (eq. 2.6) the Reynolds number ( $Re$ ) turns out to be

the ratio of the free stream velocity to the suction velocity for the asymptotic suction profile (which is shown in section 2.6.1). The advantage of choosing  $\delta_1$  as length scale is that when the suction velocity ( $V_0$ ) or the wall-normal velocity component ( $V$ ) is scaled with the free stream velocity (to be made non-dimensional) it turns out to be the inverse of the Reynolds number and the parallel flow assumption is not needed since the cross-flow term easily can be considered.

When the following base flow,  $U_i = U(x_2)\delta_{1i} + V(x_2)\delta_{2i}$ , is introduced into equation (2.17) one extra term is added to each degree of freedom, namely  $V\frac{\partial u_i}{\partial x_2}$ . The expression for the pressure (eq. 2.18) does however not change since the adding terms fulfill the continuity equation and therefore cancel out. After that the expression for the pressure is made use of in the  $v$ -equation of momentum we get

$$\left[ \left( \frac{\partial}{\partial t} + U \frac{\partial}{\partial x} - \frac{1}{Re} \frac{\partial}{\partial y} \right) \nabla^2 - U'' \frac{\partial}{\partial x} - \frac{1}{Re} \nabla^4 \right] v = 0, \quad (2.29)$$

which with the normal mode hypothesis applied give rise to the modified Orr-Sommerfeld equation according to

$$\left[ (-i\omega + i\alpha U - \frac{1}{Re} \mathcal{D})(\mathcal{D}^2 - k^2) - i\alpha U'' - \frac{1}{Re} (\mathcal{D}^2 - k^2)^2 \right] \hat{v} = 0. \quad (2.30)$$

This modified version of the Orr-Sommerfeld equation can be found in Drazin & Reid (1981). Continuing from here a modified Squire equation can equally be derived resulting in

$$\left[ (-i\omega + i\alpha U - \frac{1}{Re} \mathcal{D}) - \frac{1}{Re} (\mathcal{D}^2 - k^2) \right] \hat{\eta} = i\beta U' \hat{v}. \quad (2.31)$$

So far no change of the boundary conditions of the disturbance quantities have been made and should indeed not be necessary as long as the permeability of the porous material has a reasonably low value.

Taylor (1971) discussed the boundary conditions for a porous material and concluded that due to the open structure of a porous solid with large pores the external surface stress may produce a tangential flow below the surface resulting in that the no-slip condition is not valid. This surface velocity is assumed to depend on the mean tangential stress in the fluid outside the porous material, the permeability and another material (porous) connected parameter. This model showed that experimental results agreed well with calculation but has only influence for high permeabilities.

Another analysis of the boundary conditions of a porous plate was done by Gustavsson (2000), where a pressure perturbation above the plate is added

to Darcy's law. The result is an extra term for the boundary condition at the wall that is proportional to the permeability to the power of two, which for small permeability would be negligible. This condition has so far not been verified experimentally. In following the boundary conditions in (2.25) are used.

## 2.5. Numerical methods

The stability calculations carried out on the Blasius and the asymptotic suction boundary layer in the present chapter are for the spatial spectrum, i.e. the set of equations are solved for  $\alpha$  given a real frequency  $\omega$ , which was discussed in section 2.4. Furthermore, only the least stable modes are studied, i.e. two-dimensional wavelike perturbations according to Squire's theorem, resulting in that  $\beta = 0$  in all calculations.

The numerical method used for these calculations was a spectral method with Chebyshev expansion of the dependent variable. The solution is then represented by a truncated sum of Chebyshev polynomials according to

$$\hat{v} = \sum_{n=0}^N a_n \mathbb{T}_n^{(j)}(\hat{y}) \quad \text{for } \hat{y} \in [-1, 1],$$

where  $N$  is the truncated value,  $a_n$  is the coefficient of the  $n$ :th Chebyshev polynomial and the superscript  $(j)$  denotes the  $j$ :th derivative of the Chebyshev polynomials. A domain mapping from the finite Chebyshev domain  $([-1, 1])$  into the semi-infinite physical domain of the boundary layer was made through  $y = \frac{y_\infty}{2}(1 - \hat{y})$ . The written numerical code counts for three-dimensional perturbations even though only two-dimensional calculations are presented here.

A spatial approach gives rise to a nonlinear eigenvalue problem where the eigenvalue appears as a fourth power in the normal velocity. This can be reduced to an eigenvalue equation of second power by a transformation of the independent variable according to Haj-Hariri (1988)

$$\begin{pmatrix} \hat{v} \\ \hat{\eta} \end{pmatrix} = \begin{pmatrix} \hat{V} \\ \hat{E} \end{pmatrix} e^{-\alpha y}. \quad (2.32)$$

In order to get rid of the non-linearity, i.e. now the remaining second order  $\alpha$ -terms of the  $\hat{V}$ -component, in the eigenvalue problem one can introduce a vector quantity according to

$$\mathbf{d} = \begin{pmatrix} \alpha \hat{V} \\ \hat{V} \\ \hat{E} \end{pmatrix} \quad (2.33)$$

suggested by Schmid & Henningson (2001) which takes care of the second order  $\alpha$ -terms. After applying the transformation of equation (2.32) on the perturbation equations we get a linear eigenvalue problem which in matrix

form can be written

$$\mathcal{L}\mathbf{d} = \alpha\mathcal{M}\mathbf{d}, \quad (2.34)$$

where

$$\mathcal{L} = \begin{pmatrix} -R_1 & -R_0 & 0 \\ I & 0 & 0 \\ 0 & -S & -T_0 \end{pmatrix} \quad \text{and} \quad \mathcal{M} = \begin{pmatrix} R_2 & 0 & 0 \\ 0 & I & 0 \\ 0 & 0 & T_1 \end{pmatrix}. \quad (2.35)$$

The  $R_i$ ,  $T_i$  and  $S$  elements represent a number of terms and the only difference between the Orr-Sommerfeld & Squire equations and the modified Orr-Sommerfeld & Squire equations is the appearance of some extra terms that are marked below

$$R_2 = 4\mathbb{T}^2 + 2iURe\mathbb{T}^1 + \underbrace{2\mathbb{T}^1}_{extra} \quad (2.36)$$

$$\begin{aligned} R_1 &= -4\mathbb{T}^3 - iURe\mathbb{T}^2 - \underbrace{3\mathbb{T}^2}_{extra} - 2i\omega Re\mathbb{T}^1 + 4\beta^2\mathbb{T}^1 + \\ &+ iURe\beta^2\mathbb{T}^0 + iU''Re\mathbb{T}^0 + \underbrace{\beta^2\mathbb{T}^0}_{extra} \end{aligned} \quad (2.37)$$

$$\begin{aligned} R_0 &= \mathbb{T}^4 + \underbrace{\mathbb{T}^3}_{extra} + i\omega Re\mathbb{T}^2 - 2\beta^2\mathbb{T}^2 - \underbrace{\beta^2\mathbb{T}^1}_{extra} - i\omega\beta^2 Re\mathbb{T}^0 + \\ &+ \beta^4\mathbb{T}^0 \end{aligned} \quad (2.38)$$

$$T_1 = \mathbb{T}^1 + iURe\mathbb{T}^0 + \underbrace{\mathbb{T}^0}_{extra} \quad (2.39)$$

$$T_0 = -\mathbb{T}^2 - \underbrace{\mathbb{T}^1}_{extra} - i\omega Re\mathbb{T}^0 + \beta^2\mathbb{T}^0 \quad (2.40)$$

$$S = i\beta U' Re\mathbb{T}^0. \quad (2.41)$$

The notation of the elements in the matrixes (2.35) are chosen to be the same as used by Schmid & Henningson (2001).

The system of equations (2.34) was solved using a built-in eigenvalue problem solver in the mathematical software Matlab.

The evolution equation was also solved with a spectral approach, where Chebyshev expansion was made in the wall-normal direction and a backward finite difference method in the marching direction with a step size of  $d\xi = 0.001$ . Also here the commercially available software Matlab was used and a built in non-linear equation solver was used.

## 2.6. Theoretical results

### 2.6.1. The analytical asymptotic suction profile

A well known phenomenon in Laminar Flow Control (LFC) is the asymptotic suction profile, i.e. the profile obtained by applying continuous suction over a large area. According to Schlichting (1979) this profile was first derived by Griffith and Meredith (1936) and turns out to be of exponential nature. The restriction that has to be made is that no changes in  $x$  are allowed, i.e.  $\frac{\partial}{\partial x} \equiv 0$ . Now, the boundary layer equations (2.3) and (2.4) are reduced to  $V_0 \frac{\partial u^*}{\partial y^*} = \nu \frac{\partial^2 u^*}{\partial y^{*2}}$  for the following boundary conditions

$$\begin{aligned} y^* = 0 & : & u^* = 0 & \text{ and } & v^* = -V_0 = \text{constant}, \\ y^* \rightarrow \infty & : & u^* \rightarrow U_\infty. \end{aligned}$$

and when fully solved we end up with the asymptotic suction profile

$$u^*(y) = U_\infty \left( 1 - e^{-\frac{V_0 y}{\nu}} \right). \quad (2.42)$$

Analytical velocity profiles are not common but when achieved highly appreciated. The displacement- and momentum thickness are easily calculated through equations (2.6) and (2.7) giving us the following result

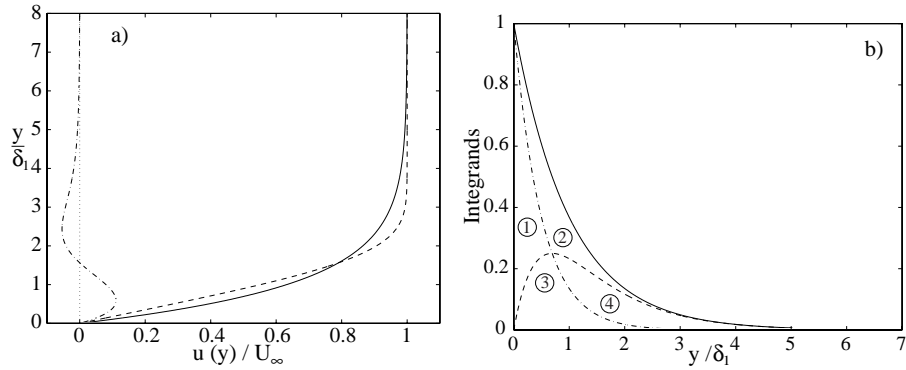


Figure 2.1: Characteristics of the asymptotic suction profile. a) Asymptotic suction profile (solid), Blasius profile (dashed) and mean deviation profile (dash-dotted). b) Integrands of  $\delta_1$  (solid),  $\delta_2$  (dashed) and  $\delta_1 - \delta_2$  (dash-dotted) of the asymptotic suction profile.

$$\delta_1 = \frac{\nu}{V_0}, \quad \delta_2 = \frac{1}{2} \frac{\nu}{V_0}, \quad \text{and} \quad H_{12} = 2. \quad (2.43)$$

Note that the exponent in equation (2.42) is equivalent to  $-y/\delta_1$ . In figure 2.1a) the asymptotic suction profile (solid line), Blasius profile (dashed line) and the mean deviation profile (dash-dotted line) are plotted in the same figure, which reveals the fuller shape of the asymptotic profile compared to the Blasius. Expression (2.43) showing that  $\delta_1 = 2\delta_2$  is geometrically verified by plotting their integrands (equations (2.6) and (2.7)) in figure 2.1b). The solid-, dashed- and the dash-dotted line corresponds to the integrands for  $\delta_1$ ,  $\delta_2$  and  $\delta_1 - \delta_2$ , respectively, making the regions 1 and 4 identical in size just as regions 2 and 3.

The viscous velocity and length scales from equation (2.9) become

$$u_\tau = \sqrt{V_0 U_\infty} \quad \text{and} \quad \ell = \frac{\delta_1}{\sqrt{Re}}, \quad (2.44)$$

where  $Re$  is the Reynolds number based on  $\delta_1$  and can be written as

$$Re = \frac{U_\infty}{V_0} \quad (2.45)$$

by making use of expression (2.43) of  $\delta_1$ . The last length scale of importance is the boundary layer thickness, which turns out to depend on  $V_0$  alone according to the following expression

$$\delta = \frac{\nu}{V_0} \log(100) = \delta_1 \log(100), \quad (2.46)$$

when defined as the distance above the plate where  $u^*(y)$  reaches  $0.99U_\infty$ .

### 2.6.2. $\varepsilon$ -parameter representing the influence of suction

The evolution equation (2.12) derived in section 2.3 describes the transformation from the Blasius profile to the asymptotic suction profile and gives the spatial evolution of the mean streamwise- and wall-normal velocity profiles when solved. In figure 2.2 the mean streamwise velocity profiles are plotted in the evolution region with a varying spatial step of  $d\xi = 0.005$  (up to 1.03), 0.01 (up to 1.1) and 0.1 (up to 1.5). At the last position, i.e.  $\xi = 1.5$ , the profile belonging to  $\xi = 5$  is also plotted (dash-dotted line) showing that no further significant evolution of the profile happens further downstream.

As a representation of the evolution region one can make a simplification in generating the velocity profiles. By introducing an  $\varepsilon$ -parameter ( $\varepsilon \in [0, 1]$ )

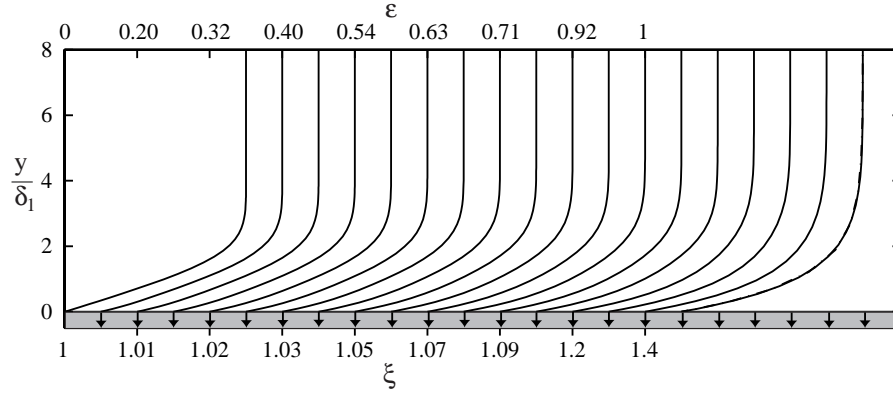


Figure 2.2: Calculated mean velocity evolution profiles from the evolution equation (2.12) with uniform suction. See text for  $\xi$  and  $\varepsilon$ .

according to following expression

$$u(y, \varepsilon) = (1 - \varepsilon)u_{bl}(y) + \varepsilon u_{as}(y), \quad (2.47)$$

where  $u_{bl}$  is the velocity of the Blasius profile and  $u_{as}$  of the asymptotic suction profile. For  $\varepsilon$  being zero the Blasius profile is achieved and for  $\varepsilon$  taken the value of unity the asymptotic suction profile is achieved and consequently values in between can be used to generate profiles of an intermediate shape. The  $\varepsilon$  value given in figure 2.2 and 2.3 is determined by minimizing the (\*)-norm of the residual vector ( $\mathbf{r}$ ) of  $u(y, \varepsilon)$  to the profile achieved from the evolution equation. The (\*)-norm is defined as

$$\|\mathbf{r}\|_* = \sqrt{\frac{1}{\delta} \int_0^\delta (u(y, \varepsilon) - u_{evo}(y))^2 dy},$$

where  $u_{evo}$  is the exact velocity profile from the evolution equation and  $u$  is from equation 2.47. These  $\varepsilon$  values are plotted versus the downstream distance in figure 2.3 a) which are based on 4000 velocity profiles. The (\*)-norm is less than 0.0111 for all profiles which can be seen in figure 2.3 b) and c). The worst profile fit with equation 2.47, i.e. for  $\|\mathbf{r}\|_* = 0.0111$  at  $\xi = 1.07$  and  $\varepsilon = 0.63$ , is plotted together with two other profiles (at locations seen in figure 2.3c)) in figure 2.4 in order to show how representative the  $\varepsilon$ -parameter is of the mean evolution velocity profiles. In this figure the solid lines are the solution from the evolution equation (2.12) at the chosen  $\xi$ -positions and the markers are from equation (2.47) for the corresponding  $\varepsilon$  value. However, even though the mean profile representation agrees well at a first sight the stability effect can be

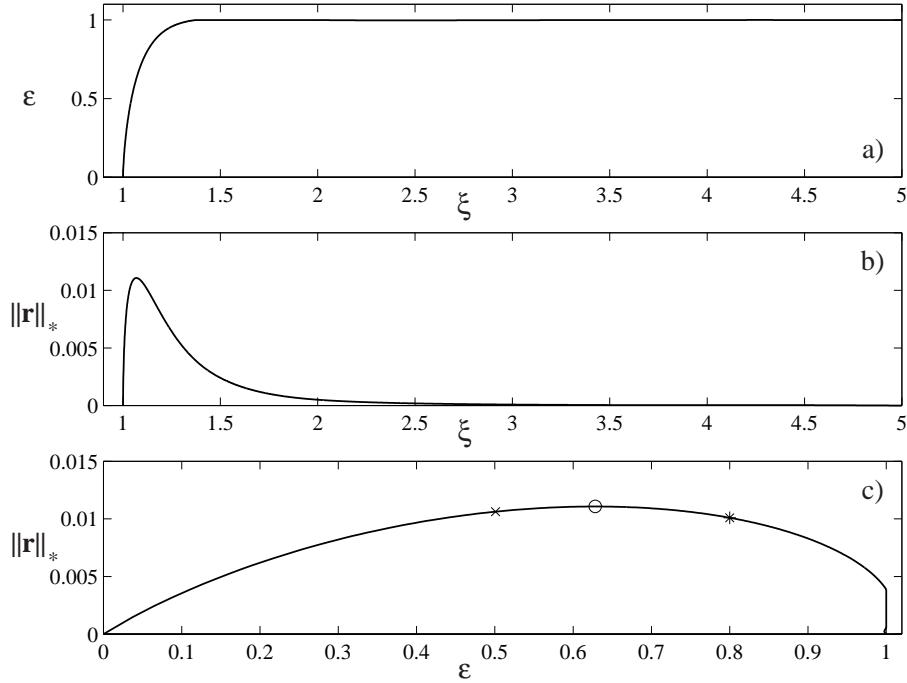


Figure 2.3: a)  $\varepsilon$ -parameter value vs the down stream distance. b) and c) shows the (\*)-norm of the residual vector (see text) vs the down stream distance and the  $\varepsilon$ -parameter, respectively. The entire profiles are plotted in figure 2.4 for the locations at ( $\times$ ), ( $\circ$ ) and ( $*$ ) in c).

large if one intend to substitute the evolution region with the  $\varepsilon$ -representation as an accurate replacement. This will be further discussed in section 2.6.3.

In figure 2.5 the displacement thickness ( $\delta_1$ ) of the profiles in the evolution region are plotted. The different curves can be seen as different impermeable entry lengths shown with the dotted lines, i.e. they belong to different values of the initial length ( $\xi_L$ ) of the simulation. These are the positions where suction starts and what all the curves have in common is that after some evolution region they all merge together to a value of unity which corresponds to the asymptotic suction region. Recall equation (2.43) and note the scaling.

### 2.6.3. Stability analysis

The simplest way to analyse the stability of the asymptotic suction profile is to use an Orr-Sommerfeld (OS) (eq. 2.21) solver with the asymptotic profile. This will be shown in the following to give accurate description of the eigenfunctions.

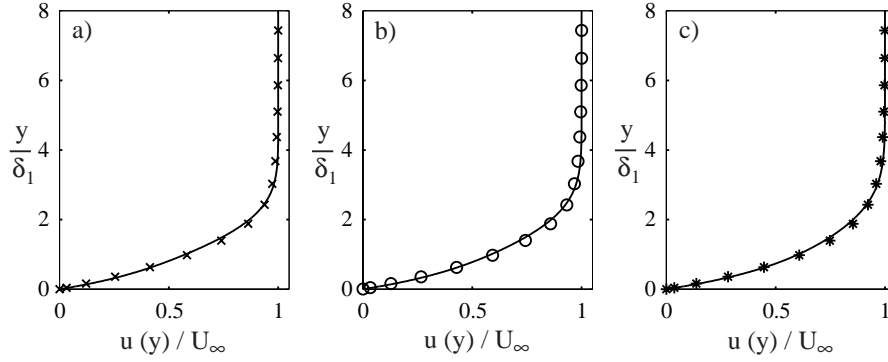


Figure 2.4: Correspondence between the evolution equation (2.12) (solid line) and the  $\varepsilon$ -parameter representation (2.47) (markers) in the worst region. a)  $\xi = 1.04$  and  $\varepsilon = 0.5$  giving  $\|\mathbf{r}\|_*^{max} = 0.0106$ , b)  $\xi = 1.07$  and  $\varepsilon = 0.63$  giving  $\|\mathbf{r}\|_*^{max} = 0.0111$ , c)  $\xi = 1.12$  and  $\varepsilon = 0.8$  giving  $\|\mathbf{r}\|_*^{max} = 0.0101$ .

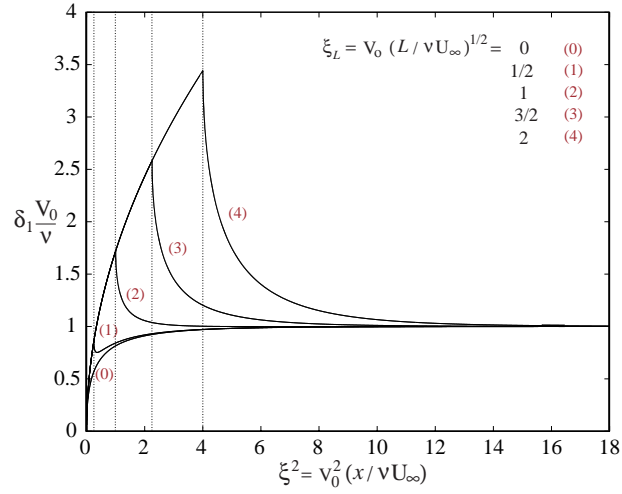


Figure 2.5: The displacement thickness evolution from the evolution equation (2.12) vs the downstream distance to the power of two. See text for comments.

However, in order to get accurate values of the growth/decay rate one has to solve the modified Orr-Sommerfeld (mod-OS) equation (2.30) in order to catch the influence of the  $V$ -component. Now, when solving for the Blasius profile one uses the Orr-Sommerfeld equation (2.21) and for the asymptotic suction

profile the modified Orr-Sommerfeld equation (2.30), which in the limit of  $\varepsilon$  going from zero to unity is somewhat difficult since a discontinuity will always appear when change of equation is done. This can be by-passed if applying the  $\varepsilon$  concept (introduced in the previous section) on the modified stability equation, i.e. by multiplying all extra terms in equations (2.36)-(2.40) with the  $\varepsilon$ -parameter, resulting in a successively increasing influence of the  $V$ -component when changing the profile towards exponential. This method will be denoted the *variable* modified Orr-Sommerfeld (varmod-OS) equation.

The stability of the worst profile representation with the  $\varepsilon$ -parameter was compared in order to see if the stability feature agreed as well. However, small changes in the velocity profile that hardly are thought to make any distinction can have large influence on the derivatives and since the second derivative of the velocity profile is directly present in the Orr-Sommerfeld equation 2.21 (and the

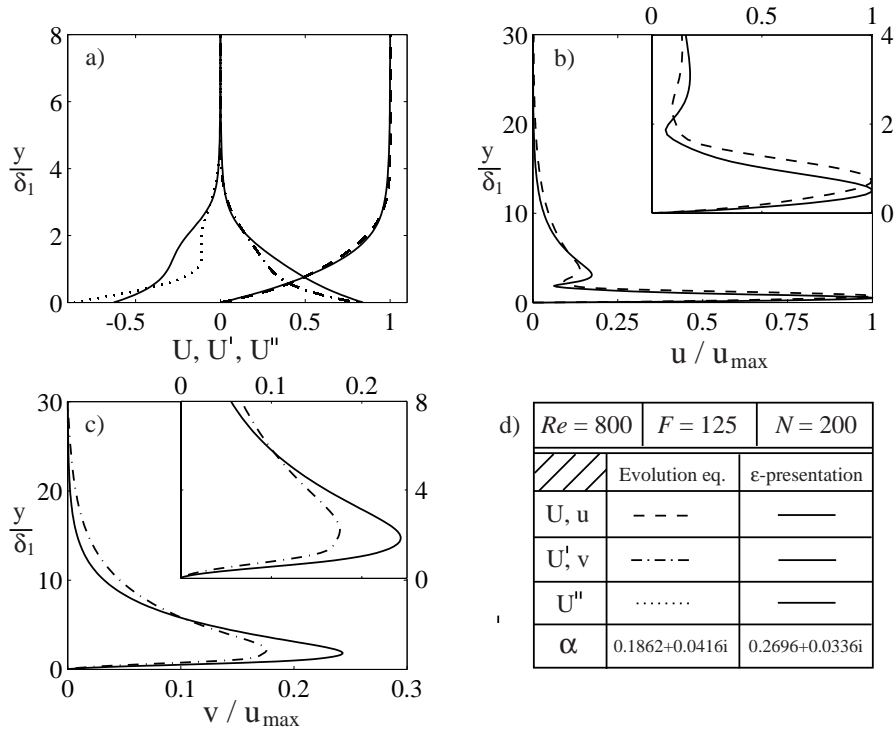


Figure 2.6: Comparison of the evolution equation and  $\varepsilon$ -representation for the worst deviation case. a) Mean velocity properties. b) Streamwise eigenfunction (least stable mode). c) Wall-normal eigenfunction (least stable mode). d) Parameter table.

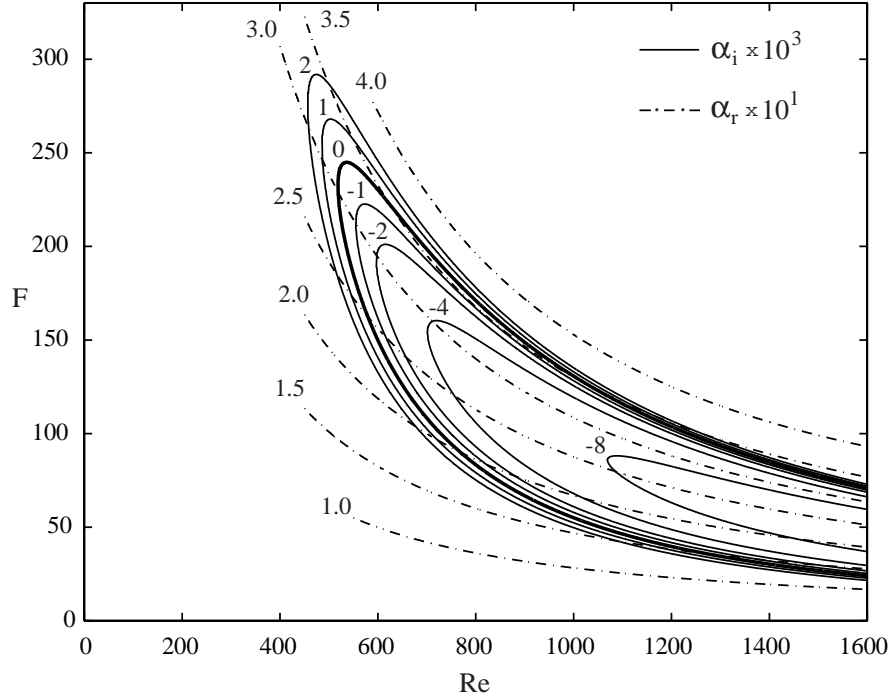


Figure 2.7: Spatial stability curves for the Blasius profile. Solid lines are for constant imaginary parts of the stream wise wavenumber ( $\alpha_i$ ) and dash-dotted for constant real parts ( $\alpha_r$ ). The bold solid line is the neutral stability curve.

first derivative in the Squire equation 2.23) it may effect the stability characteristics strongly. In figure 2.6 the comparison between the worst  $\varepsilon$ -representation and the exact profile from the evolution equation is illustrated, i.e. comparison between the two profiles in figure 2.4b). As can be seen in figure 2.6a) the first and second derivatives of the two profiles do not agree resulting in a large difference of the calculated eigenvalue ( $\alpha$ ) in d) and correspondingly of the eigenfunctions in b) and c). The long and the short of the  $\varepsilon$ -representation is that one can not make use of it if an accurate representation of the evolution region by means of stability is sought. However, it can still be used as a representation of what happens with the stability in between the Blasius and the asymptotic suction profile. The stability calculations in figure 2.6 is with the varmod-OS method.

The stability diagram is given in figure 2.7 for the Blasius profile. The solid lines are contours of the growth factor ( $\alpha_i$ ) where the bold solid line shows the

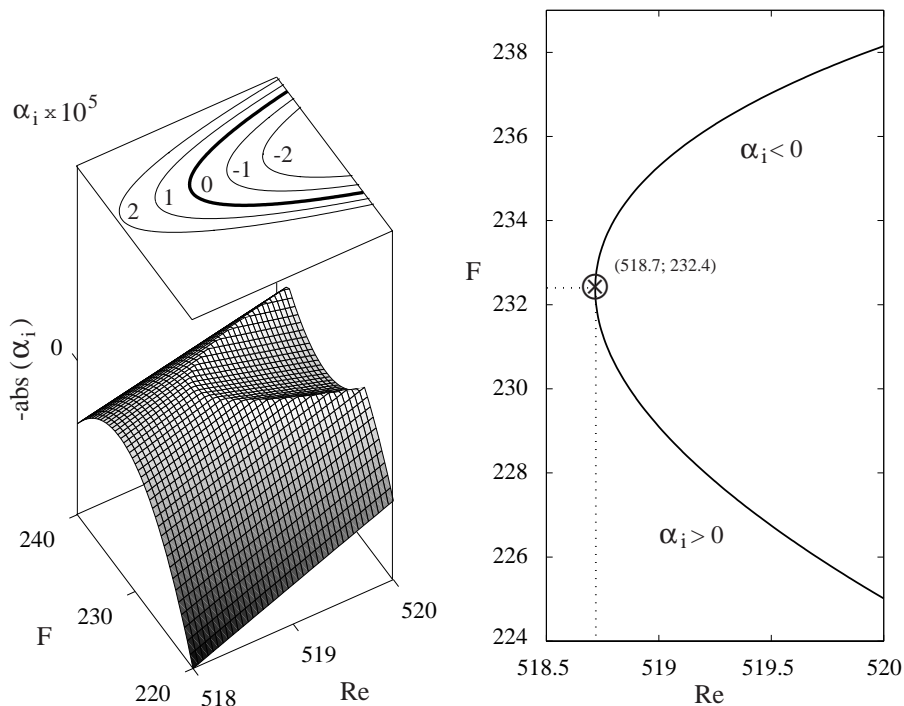


Figure 2.8: Spatial determination of the critical Reynolds number ( $Re_c$ ) for the Blasius profile. a) contains  $201(F) \times 41(Re)$  eigenvalue calculations with  $N = 100$  and  $y_\infty = 20$ . b) shows  $Re_c$  and  $F_c$ .

neutral stability curve, i.e. the contour line of  $\alpha_i = 0$ . The dash-dotted lines correspond to contour lines of constant wave number ( $\alpha_r$ ). What always is of interest is to know where the first unstable mode appears, this being the critical point in the  $Re - F$  plane here denoted as  $[Re, F] = [Re_c, F_c]$ . One way to determine these critical values is to scan the  $Re - F$  plane with a small step size around the critical point. This was done for the Blasius profile and is shown in figure 2.8a). A total area of  $20 \times 2 FRe$ -units was scanned with a total amount of  $201 \times 41$  points. Then the critical values can be determined graphically in figure 2.8b) to  $[Re_c, F_c] = [518.7, 232.4]$  for the Blasius profile. These critical values are in good agreement with other published values, see e.g. Drazin & Reid (1981) and Schmid & Henningson (2001), and the slightly varying values may be due to solution method. One can however determine the critical values without carrying out unnecessary calculations, i.e. by means of creating search routines. Such a program was developed, with a temporal approach since it

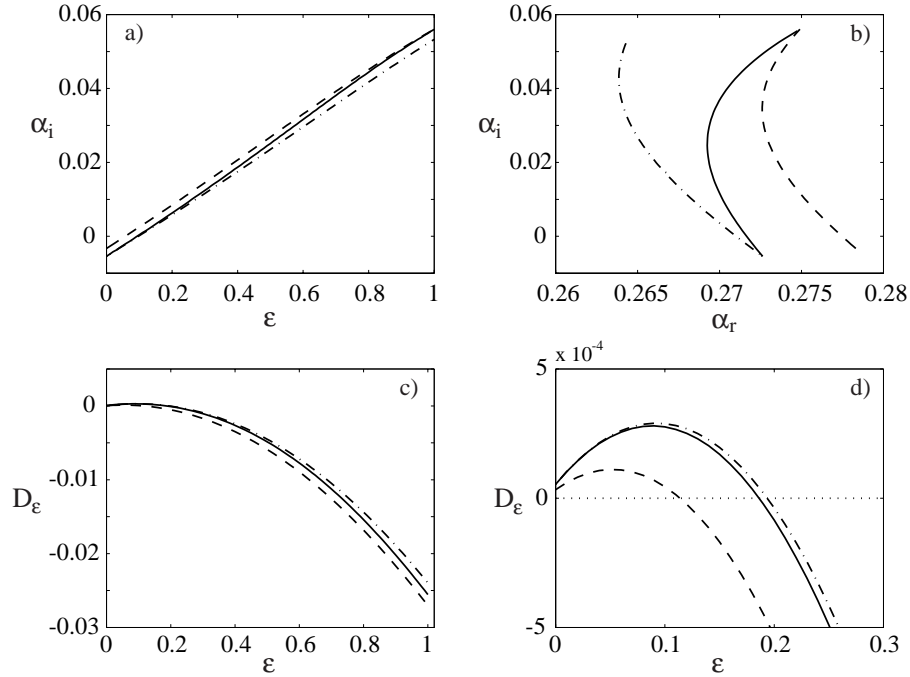


Figure 2.9: Comparison between the OS-eq. (dash-dotted line), modified OS-eq. (dashed line) and the variable modified OS-eq. (solid line).  $Re = 800$ ,  $F = 125$  and  $\epsilon$  varying from 0 to 1 with a step size of  $d\epsilon = 0.01$ .

is faster, in order to provide high accuracy of the critical values. For a given wave number ( $\alpha$ ) this program searches for the Reynolds number where the imaginary part of the phase velocity ( $c_i$ ) is zero with an accuracy specified by the user and stops only for positive values of  $c_i$ . From there it chooses a new  $\alpha$  by means of minimizing  $Re$ . The accuracy of  $\alpha$  is also set by the user. The same critical Reynolds number was obtained with the search program as with the graphical technique. In table 1 the critical values are shown for both the Blasius and the asymptotic suction case.

In figures 2.9-2.11 the three different methods are compared, i.e. the OS-, mod-OS- and the varmod-OS-method. In figure 2.9a) it is clear that what contributes to the major part of the stabilizing effect is the shape of the velocity profile and not the additional  $V$ -component in the modified versions. Here the

$\varepsilon$	0 (Blasius)	1 (Asymptotic)
$Re_c$	518.7	54382
$\alpha_c$	0.3036	0.1555
$c_r^c$	0.3966	0.1499

Table 1: Critical values for the Blasius and the asymptotic suction boundary layer.

dash-dotted line corresponds to the OS-eq., the dashed line to the mod-OS eq. and the solid line to the varmod-OS equation. It is seen that the dashed line lies above the dash-dotted line for all  $\varepsilon$ , whereas the solid line starts at the OS eq. for  $\varepsilon = 0$  and then approaches the mod-OS eq. as  $\varepsilon$  approaches unity. The  $\alpha$ -plane is plotted in figure 2.9b) for all  $\varepsilon$  values and here the  $\varepsilon$  concept becomes obvious since the varmodOS eq. can describe the evolution states of the velocity profile and the  $V$ -component contribution without any discontinuity in curves. In figures 2.9c) and d) a decay factor ( $D_\varepsilon$ ) is used and is defined as

$$D_\varepsilon(\varepsilon) = - \int_{\varepsilon_0}^{\varepsilon} \alpha_i(\varepsilon') d\varepsilon'. \quad (2.48)$$

It is an accumulative factor of the  $\varepsilon$  value, i.e. the velocity profile. The position in the  $Re - F$  plane is  $[Re, F] = [800, 125]$ , which is in a highly unstable region for  $\varepsilon = 0$  (see figure 2.7), resulting in that a small growth is first achieved before the change of  $\varepsilon$  gets large enough to push the stability curve out of range from the initial position. This can be observed in figure 2.9d), which is a blow-up of the growth region in c). For the decay factor the solid line does never reach the mod-OS eq. (dashed line) state since the decay factor has a history effect on the profile change. In figures 2.10 and 2.11 the eigenfunctions  $\hat{u}$  and  $\hat{v}$ , respectively, are examined for varying  $\varepsilon$ . In these two figures the eigenfunctions from all three methods are plotted. It is hardly possible to distinguish them from each other for the same  $\varepsilon$ , but in the last square of each figure both the eigenfunction corresponding to  $\varepsilon$  zero and unity are plotted and it clearly illustrates the difference in shape between the Blasius- and asymptotic suction profile input. In figure 2.12 the phase distribution of the  $\hat{u}$ -component is plotted for the variable modified OS-method. The difference between the Blasius ( $\varepsilon=0$ ) and the asymptotic suction ( $\varepsilon=1$ ) boundary layer eigenfunctions

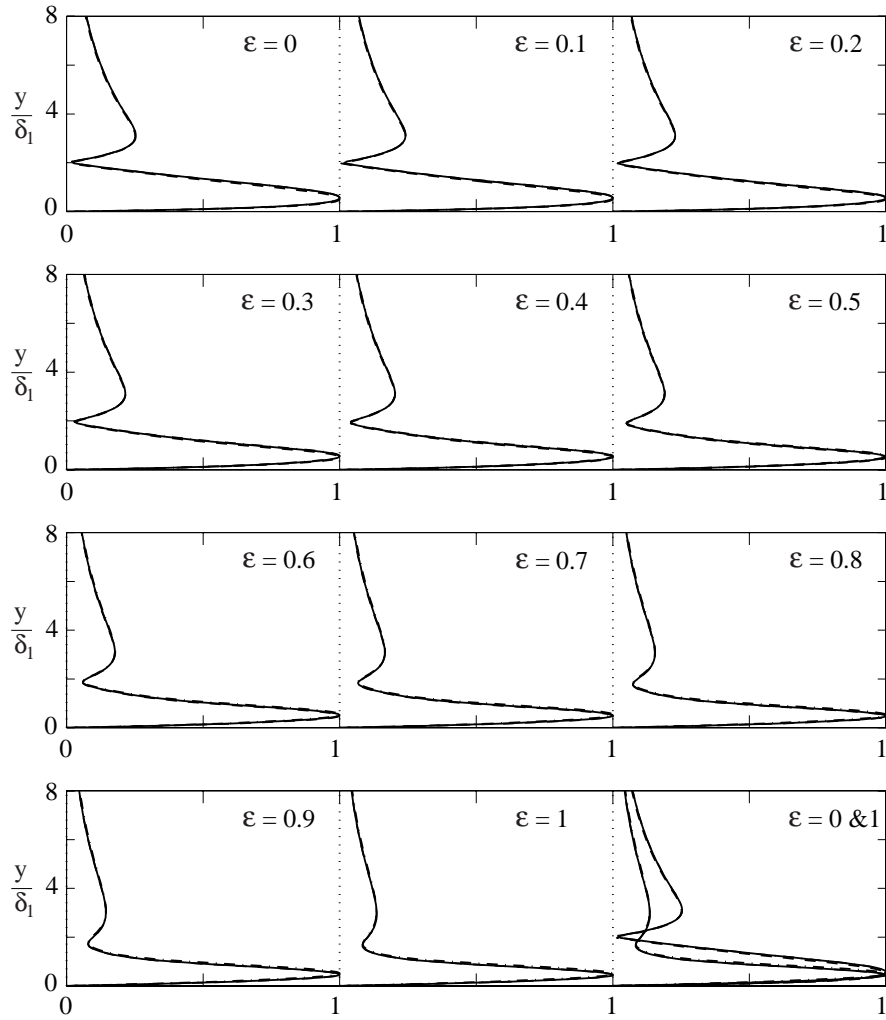


Figure 2.10: Eigenfunctions of the  $\hat{u}$ -component normalized with its maximum value for different  $\varepsilon$  values and  $(Re, F) = (800, 125)$ . OS-eq. (dash-dotted line), modified OS-eq. (dashed line) and the variable modified OS-eq. (solid line).

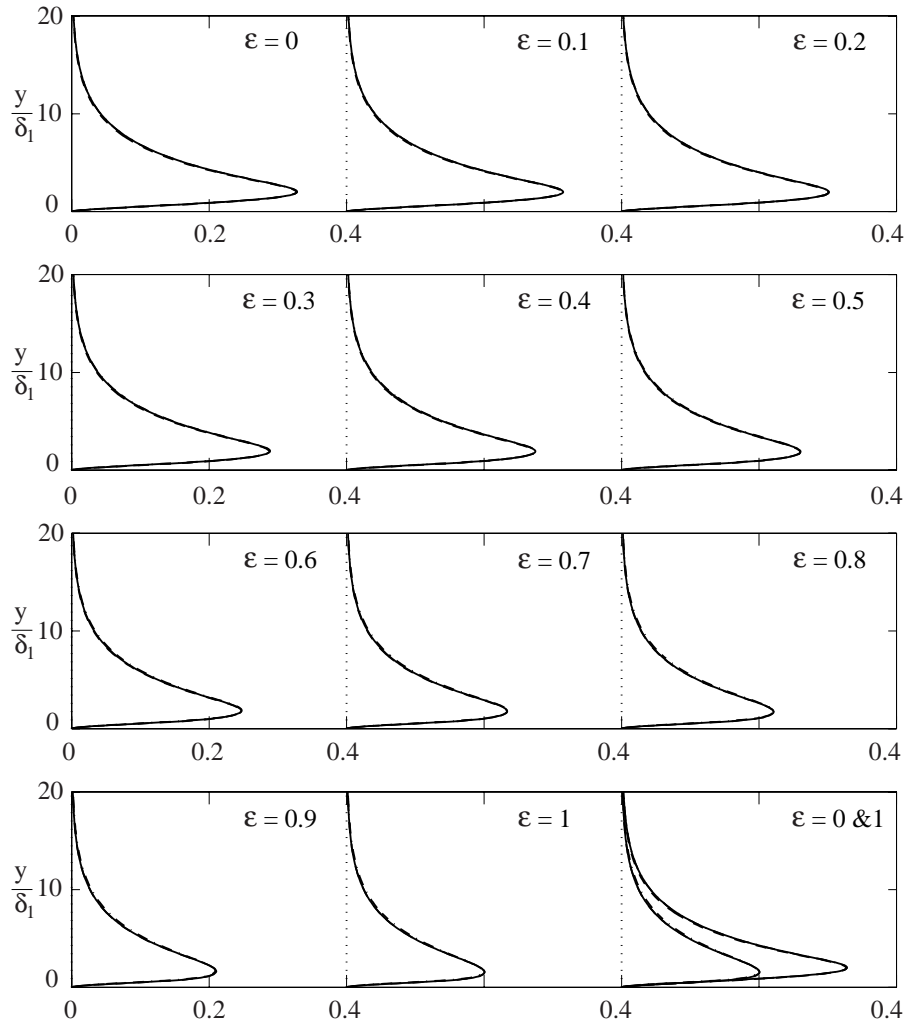


Figure 2.11: Eigenfunctions of the  $\hat{v}$ -component normalized with the corresponding maximum value of  $\hat{u}$ -component for different  $\varepsilon$  values and  $(Re, F) = (800, 125)$ . OS-eq. (dash-dotted line), modified OS-eq. (dashed line) and the variable modified OS-eq. (solid line).

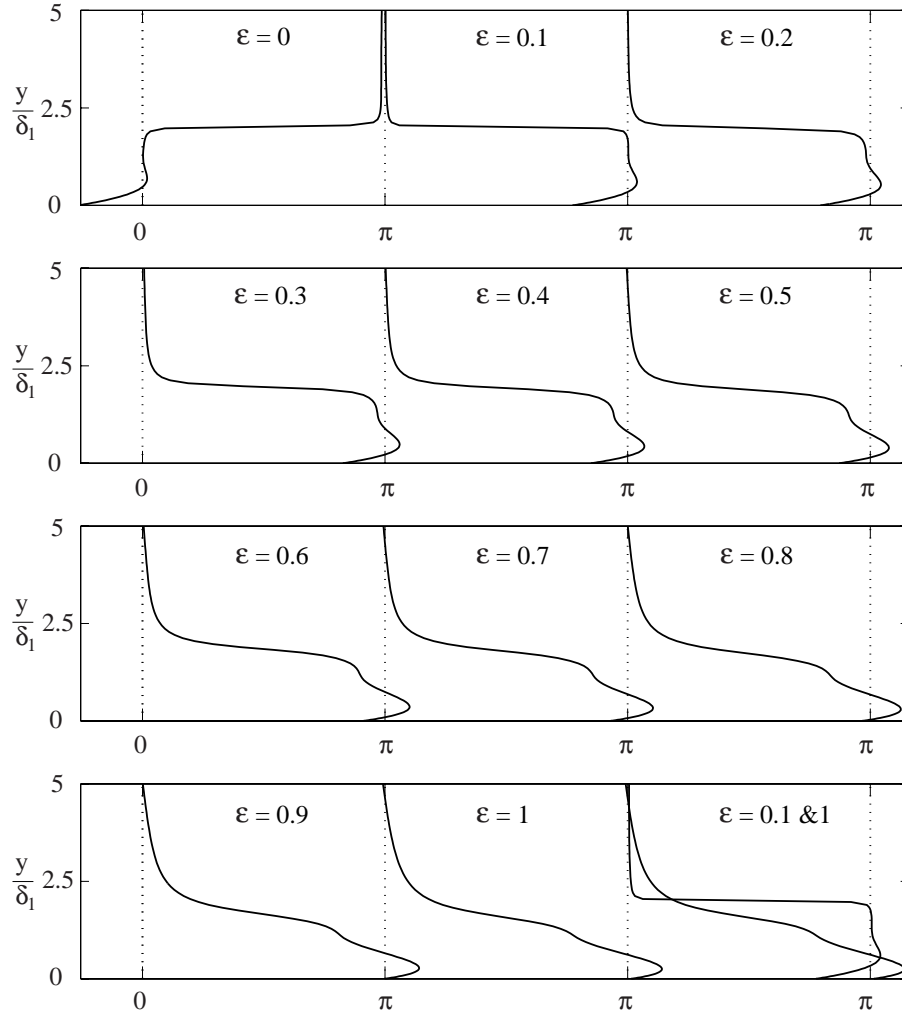


Figure 2.12: Phase distribution of the  $\hat{u}$ -component for different  $\varepsilon$  values and  $(Re, F) = (800, 125)$ . The solid line corresponds to the variable modified OS-eq.

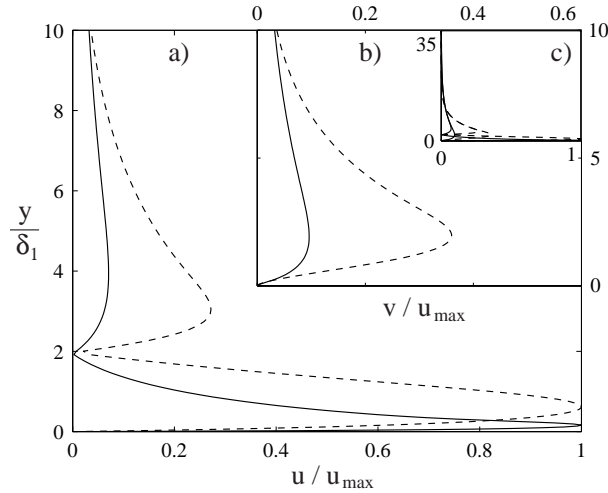


Figure 2.13: Eigenfunctions of both the Blasius and the asymptotic suction case at their critical values respectively. a) Streamwise eigenfunction, b) wall-normal eigenfunction, and c) blow-up of a) and b) showing the convergence in the free stream. (Solid lines) Blasius and (dashed lines) asymptotic case.

(streamwise and wall-normal) at their critical values respectively (see table 1) are shown in figure 2.13.

## 2.7. Model problem

### 2.7.1. Mean flow distribution

The asymptotic suction profile is one of few exact solutions to the Navier-Stokes equations, however it is also possible to obtain an exact solution for the streamwise velocity profile in a plane channel with uniform cross flow. The shape of the profile depends on a Reynolds number,  $R_v = V_0 h / 2\nu$ , based on the crossflow velocity ( $V_0 = \text{const}$ ) and half the channel height  $h/2$ . In this section the stability of this flow case will be analyzed as a model problem.

The velocity profile can be written as

$$\frac{u(y)}{U_0} = R_v \frac{y + \sinh^{-1}(R_v) e^{-R_v y} - \coth(R_v)}{1 - \log\left(\frac{\sinh(R_v)}{R_v}\right) - R_v \coth(R_v)}, \quad (2.49)$$

where  $y$  ( $\in [-1, 1]$ ) is the non-dimensional variable normal to the walls and  $U_0$  is the maximum streamwise velocity. In the limit of  $R_v \rightarrow 0$  expression (2.49) simply becomes the parabolic velocity profile, i.e.  $u(y)/U_\infty = 1 - y^2$ . The velocity profiles are plotted in figure 2.14a). In the presence of the crossflow

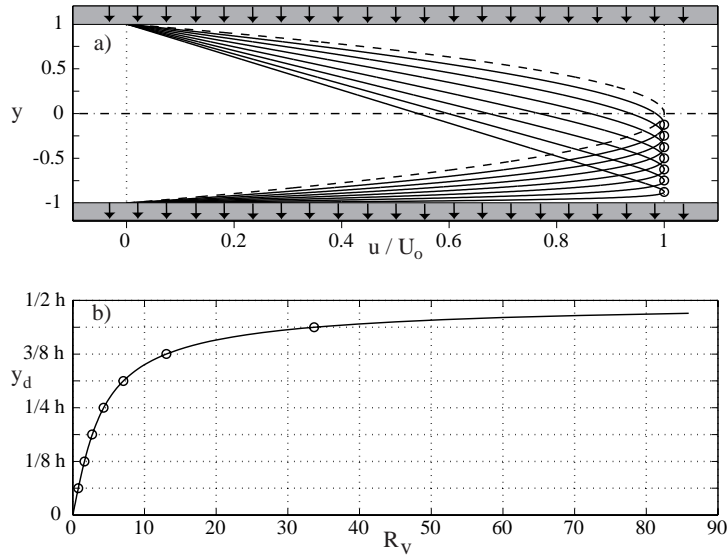


Figure 2.14: a) Plane Poiseuille flow with continuous crossflow and keeping the maximum streamwise velocity constant. Dashed line is the parabolic profile achieved when the crossflow is absent and the dash-dotted indicates the centreline. b) The influence of  $R_v$  on  $y_d$ . See text for comments.

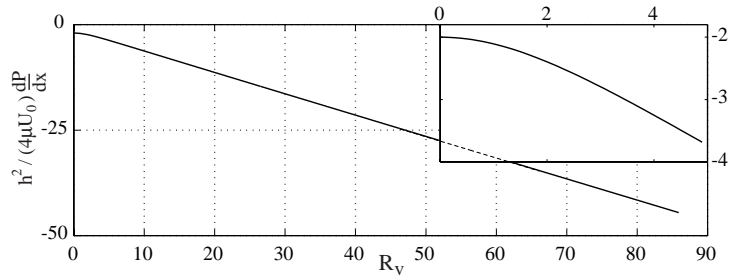


Figure 2.15: Influence of the crossflow on the streamwise pressure gradient when keeping  $U_0$  constant.

the position of maximum streamwise velocity (this position is denoted by  $y_d$  in the following) shifts towards the lower (suction) wall. In figure 2.14b)  $y_d$  is plotted versus  $R_v$ , where the  $y_d$ -values of the profiles in a) are marked with circles. Note that for high enough values of  $R_v$  the velocity profile will approach

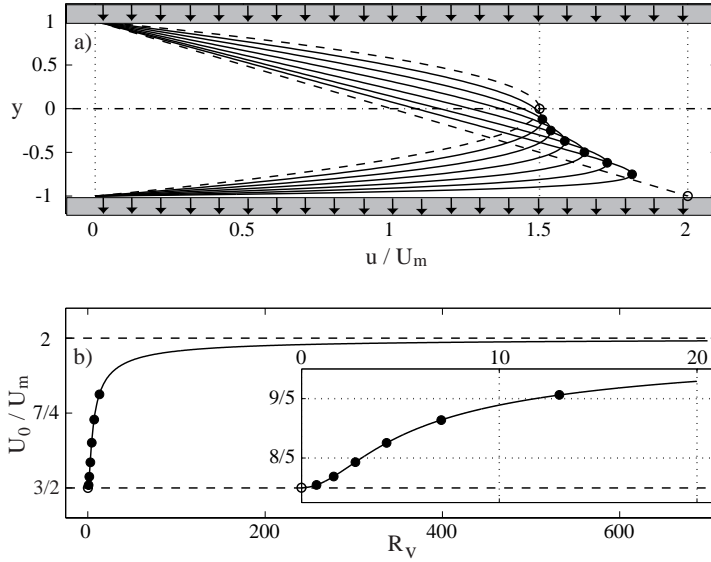


Figure 2.16: a) Plane Poiseuille flow with continuous crossflow and constant massflow. Dashed lines are the parabolic and linear Couette profiles whilst the dash-dotted indicates the centreline. b) Influence of  $R_v$  on  $U_0$  for constant massflow ( $U_m$ ). The markers corresponds to the same  $y_d$  as in figure 2.14.

the linear Couette flow profile, except for a thin boundary layer at the suction wall. In the above expression the streamwise pressure gradient is substituted by expressing it with the maximum velocity ( $U_0$ ) in the channel. The pressure gradient is plotted in terms of ( $U_0$ ) in figure 2.15 versus  $R_v$  which shows that the pressure difference has to increase to keep  $U_0 = \text{const}$ .

In previous works on the stability analysis of this particular flow, e.g. Hains (1971) and Sheppard (1972), the pressure gradient has instead been held constant. For such a condition the crossflow decreases the maximum velocity and thereby the flow Reynolds number. This has been proven to have a stabilizing effect of the flow for all  $R_v$  and Hains (1967) showed that the unstable mode in plane Poiseuille flow (without crossflow) becomes completely stable as the velocity profile approaches the linear profile of Couette flow, which in turn has been proven to be stable for all infinitesimal disturbances (see e.g. Potter (1966)).

In this study the stability is considered through two other Reynolds numbers than what was used by the above references (based on constant  $dP/dx$ ). One of the Reynolds numbers is based on a constant  $U_0$ , whereas the other is based on a constant average velocity ( $U_m = \text{const}$ ) defined as

$$U_m = \frac{1}{2} \int_{-1}^1 u(y) dy.$$

This latter condition gives an increasing maximum velocity, see figure 2.16a), with increasing cross flow velocity. In figure 2.16b) the influence of  $R_v$  on  $U_0/U_m$  is plotted. For the parabolic profile the value is  $3/2$ , whereas in the asymptotic limit when  $R_v \rightarrow \infty$ , the Couette flow limit is approached and the maximum velocity is twice the average velocity. To keep the Reynolds number constant the applied pressure gradient has to increase with increasing cross flow for both cases.

### 2.7.2. Stability characteristics

In chapter 2 a detailed description of the derivation of the stability equation in form of a modified Orr-Sommerfeld equation was given. The crossflow term can easily be considered in the linearized stability equation, i.e. the parallel flow assumption is not needed which gives rise to some extra convective terms in the stability equation. This stability analysis is done with a temporal approach implying that the eigenvalue problem is solved for  $\omega \in \mathbb{C}$  or alternately for  $c = \omega/\alpha$ , being the phase velocity, and with the streamwise and spanwise wave numbers  $\alpha, \beta \in \mathbb{R}$ .

For a specific  $Re$  and wavenumber ( $\alpha$ ) the influence of  $R_v$  on the stability is analyzed. For the chosen values, which are  $(Re, \alpha, \beta) = (6000, 1.0, 0)$ , the parabolic profile is unstable, i.e.  $c_i > 0$ . For a gradually increasing crossflow

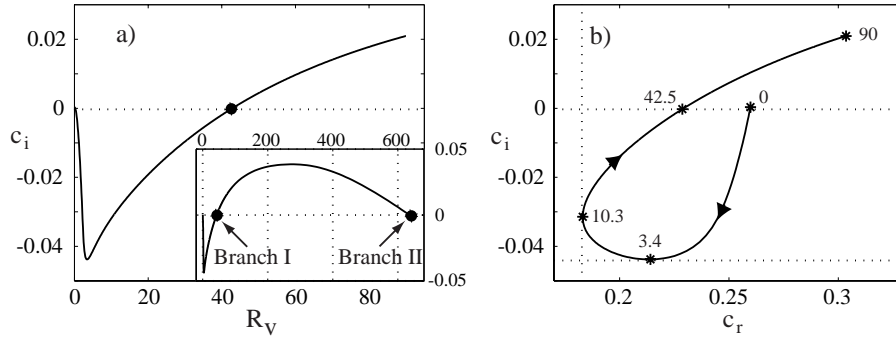


Figure 2.17: Stability calculation where the flow Reynolds number is based on the maximum velocity. Flow parameters  $(Re, \alpha, \beta) = (6000, 1.0, 0)$ . a) Shows the turning point of where  $R_v$  stops being stabilizing. b) The complex phase velocity plane with corresponding  $R_v$ -values at (\*)-markers.

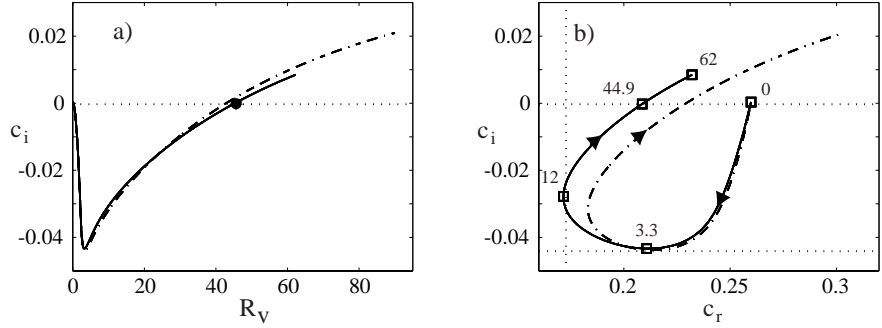


Figure 2.18: Stability calculation where the flow Reynolds number is based on the average velocity. Flow parameters  $(Re_m, \alpha, \beta) = (4000, 1.0, 0)$  corresponding to  $Re = 6000$  for  $R_v = 0$ . a) Shows the turning point of where  $R_v$  stops being stabilizing. b) The complex phase velocity plane with corresponding  $R_v$ -values at ( $\square$ )-markers. For solid line  $c$  is normalized with  $U_0$  and the dash-dotted line is the curve seen in figure 2.17b).

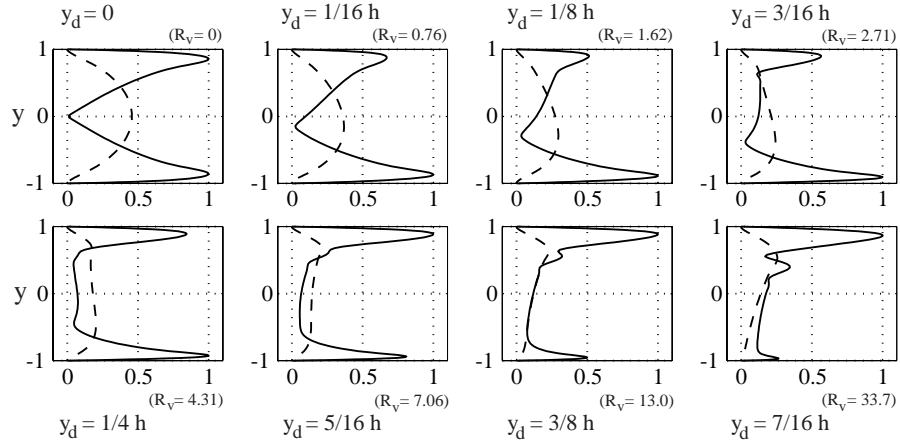
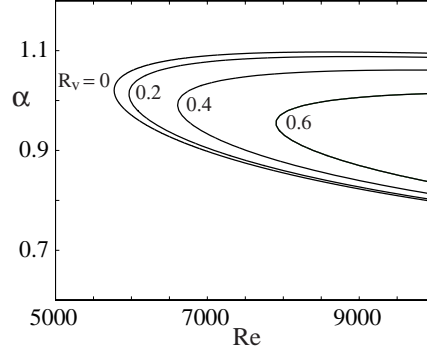


Figure 2.19: Amplitude distributions of streamwise and wall-normal disturbance function,  $|\hat{u}|$  (solid lines) and  $|\hat{v}|$  (dashed lines) respectively, for different strength of the cross flow. Both functions are normalized with the maximum value of  $|\hat{u}|$ . Flow parameters  $(Re, \alpha, \beta) = (6000, 1.0, 0)$ .

Figure 2.20: Neutral stability curves for varying  $R_v$ .

the flow is first stabilized until some critical value is reached. Increasing the crossflow further destabilizes the flow and it becomes unstable again after a certain threshold of  $R_v/Re$  is reached, typically 0.5 – 1%. This threshold value will be denoted branch I, since for a further increasing  $R_v$  the flow will enter the stable region again after crossing branch II. This is seen in figure 2.17a) and b), where the least stable mode is followed. In 2.17a)  $c_i$  is plotted versus  $R_v$  where the branches are marked in the reduction figure and in b) the complex plane of the phase velocity ( $c = c_r + ic_i$ ) is plotted where the  $R_v$ -value is given at the markers.

When keeping  $Re = \text{const.}$  based on  $U_0$ ,  $Re_m$  based on the average velocity decreases. In order to show that this influence is small, figure 2.18a) and b) show similar plots (as in figure 2.17) but now with  $Re_m = \text{const.}$  based on the average velocity. As can be seen the effect of the choice of Reynolds number is only marginal.

For both Reynolds numbers used here we see a stabilizing effect for small crossflow velocities which is in agreement with the previous works. However, for a critical value the influence of the cross flow changes character and becomes destabilizing, even reaching an unstable region before it changes character again and finally becomes stable. This behaviour has not been observed before.

The streamwise and wall-normal disturbance amplitude distributions belonging to the least stable eigenvalue are shown in figure 2.19 for different strengths of the cross flow (here given both in terms of  $R_v$  and  $y_d$ ). The distributions between the two different Reynolds number based calculations can hardly be distinguished, thus only the maximum velocity based is plotted. For small values of  $R_v$  (up to 3.4 for these parameters) the flow stabilizes and the

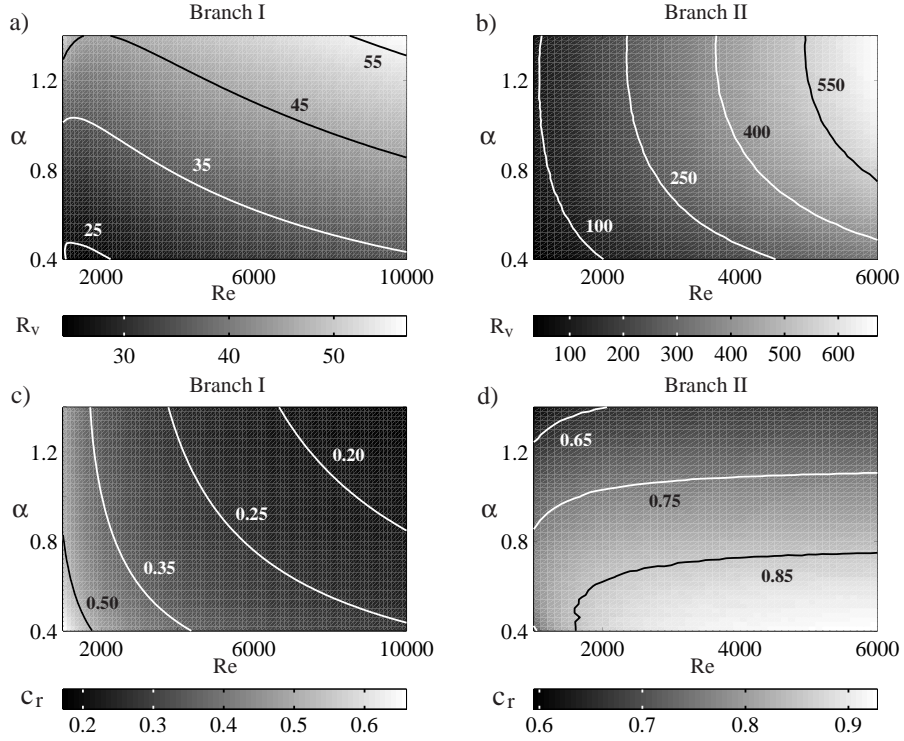
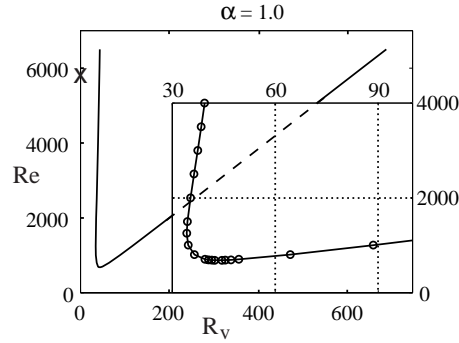


Figure 2.21: Contour plots of  $R_v^c$  and  $c_r$  in the  $\alpha$ - $Re$  plane for branch I. a) and c) and branch II b) and d).

effect on  $\hat{u}$  is a decreasing amplitude of the upper peak (blowing side) as compared to the suction side. The suction side peak also moves towards the wall. The distribution of the wall-normal disturbance shows a similar trend, i.e. its maximum is shifted towards the suction side. When increasing  $R_v$  further the streamwise disturbance peak at the blowing side becomes the largest and also the wall normal disturbance has its largest amplitude in the upper part of the channel.

Neutral stability curves for  $R_v = 0, 0.2, 0.4$  and  $0.6$  are plotted in figure 2.20 to show the movement of the curves for increasing  $R_v$ . The shift of the curves towards higher  $Re_c$  and lower  $\alpha_c$  may be observed for increasing  $R_v$ . Recall that for relatively large  $R_v$  the stability changes character and therefore the neutral stability curve will at some  $R_v$  change direction in its movement towards smaller  $Re_c$ . The critical values for the chosen crossflows in figure 2.20 are presented in table 2. These values are calculated with a critical-value search program,

Figure 2.22: Neutral stability curve for  $\alpha = 1.0$  in the  $Re$ - $R_v$  plane.

discussed in section 2.6.3, developed for accurate determination of these values. The critical value for plane Poiseuille flow determined here are in agreement with e.g. Schmid & Henningson (2001).

As was shown in figure 2.17 there is a region of intermediate  $R_v$  where the cross flow makes the flow unstable. In order to elucidate this region contour plots of critical  $R_v$  with the corresponding  $c_r$  for branch I and II in the  $\alpha$ - $Re$  plane are shown in figure 2.21. The solid lines indicates paths of constant critical  $R_v$ -values (a,b) and  $c_r$ -values (c,d).

In figure 2.22 the neutral stability curve for  $\alpha=1.0$  is plotted in the  $Re$ - $R_v$  plane. For small values of  $R_v$  the critical  $Re$  increases dramatically from  $Re_c = 5814.9$ , marked with (x) in figure 2.20, and the unstable range of wavenumbers becomes smaller. When  $R_v$  increases further the flow becomes more unstable and the neutral curve moves towards lower critical  $R_v$ . The ultimate critical values are determined to be  $(Re_c, \alpha_c, R_v^c) = (667.4, 0.858, 38.24)$  with  $c_r = 0.644$ . The critical  $Re$ -value can substantially be reduced when crossflow is

$y_d$	$R_v$	$Re_c$	$\alpha_c$	$c_r$	$R_v/Re_c$
0	0	5772.22	1.02039	0.263982	0
0.0332 h	0.2	5967.01	1.01189	0.261378	3.35e-5
0.0665 h	0.4	6607.4	0.99025	0.25399	6.05e-5
0.0989 h	0.6	7902.5	0.95361	0.24148	7.59e-5

Table 2: Critical values for various  $y_d$  values. (See text)

present and for the ultimate critical value the crossflow velocity to the maximum streamwise velocity ratio is 5.7%, and the critical  $Re$  is hence lower by an order of magnitude as compared to plane Poiseuille flow.

## CHAPTER 3

### Experimental design and set-up

This chapter deals with the design of the experimental set-up, the construction work, and the experimental techniques. In order to perform experiments in an asymptotic suction boundary layer a plate had to be designed and built with a suitable permeable surface material. Furthermore, a removable leading edge was designed, which also can be used together with other plates.

#### 3.1. Leading edge

An asymmetric leading edge was specially designed for this experimental set-up, which resulted in a relatively short pressure gradient region without any suction peak at the leading edge. The work by Klingmann *et al.* (1993) ended the discussion whether or not linear parallel stability theory of a Blasius boundary layer agrees with experiments. This success was partly because of the MTL wind-tunnel at KTH, which has a very low background disturbance level, but also due to the specially designed leading edge, which has been used as a challenge in the design of the new (58% thicker) leading edge.

The ideal flat plate does not have any leading edge, it is simply an infinitely thin plate with a zero pressure gradient everywhere. When placing any obstacle in a flow the fluid will accelerate around it causing the static pressure to decrease. First when the fluid is allowed to decelerate the pressure can start to recover. In figure 3.1 a symmetric "leading edge" generated by a two-dimensional source in a uniform velocity field with potential flow theory is shown (solid line). The pressure coefficient ( $C_p$ ) possessing an exact solution for this body is also plotted (dashed line). At the stagnation point ( $x/L = 0$ )  $C_p$  is equal to unity according to potential flow theory. Thereafter  $C_p$  is reduced as long as the fluid is accelerating around the nose, but as soon as the curvature starts to decrease the pressure starts to recover. This dip of  $C_p$  is the well known suction peak giving rise to a local negative pressure gradient followed by a positive one. The large pressure gradient prevents the evolution of a Blasius profile in this region and also effects the stability characteristics of the boundary layer flow, as shown by Klingmann *et al.* (1993). They showed that an asymmetric leading edge together with a trailing edge flap can limit this influence of the leading edge.

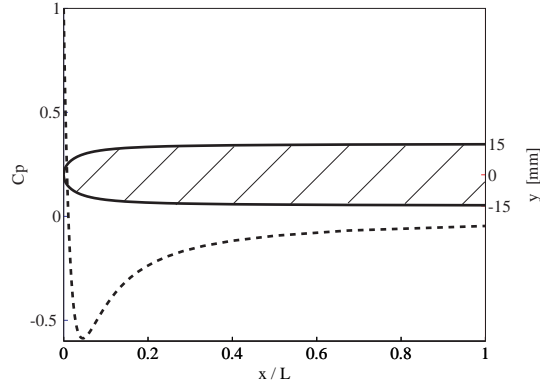


Figure 3.1: Symmetrical leading edge generated by a 2D source in a uniform velocity field with potential flow theory ( $L=0.215$  m).

### 3.1.1. Flow calculations

The commercial flow solver CFX 4.2 was used to design the leading edge for the present set-up. Two-dimensional laminar flow calculations was performed in the test section of the wind tunnel, i.e. the ceiling (upper wall) and the floor (lower wall) of the tunnel were simulated together with the plate. Since the plate is not positioned in the centre of the test-section the ceiling and floor influence the pressure distribution and this effect can not be neglected. Furthermore, the tuning of the stagnation point at the leading edge could be done by simulating the effect of a trailing flap by changing the outflow ratio between the upper (I) and lower (II) outlet. In this way the full length of the plate does not need to be simulated and the computational box can be reduced.

Two cubic Bézier-curves connected at the nose tip were used to describe the upper and the lower sides of the leading edge. A cubic Bézier-curve is a parameter based polynomial consisting of two interpolation points ( $\bar{p}_1, \bar{p}_2$ ) and ( $\bar{p}_2, \bar{p}_3$ ) for the lower and upper parts, respectively) and two steering points ( $(\bar{b}_l, \bar{c}_l)$  and  $(\bar{b}_u, \bar{c}_u)$  the for lower and upper parts, respectively). The interpolation points are shown in figure 3.2. In the connection point between the upper and lower curves the two curves were forced to have the same first derivate (expressed by the  $\bar{K}_{2l}$  and  $\bar{K}_{1u}$  vectors) making the transition smooth.

A systematic parameter study was performed by applying different total areas (or weights) of the leading edge. The varying parameters are nose position ( $\bar{p}_2$ ), starting points of curvature on lower and upper side ( $\bar{p}_1$  and  $\bar{p}_3$  respectively), and the steering points ( $2 \times \bar{b}$  and  $2 \times \bar{c}$ ), i.e. totally 7 parameters. First an area (or weight) of the leading edge was chosen and then the steering

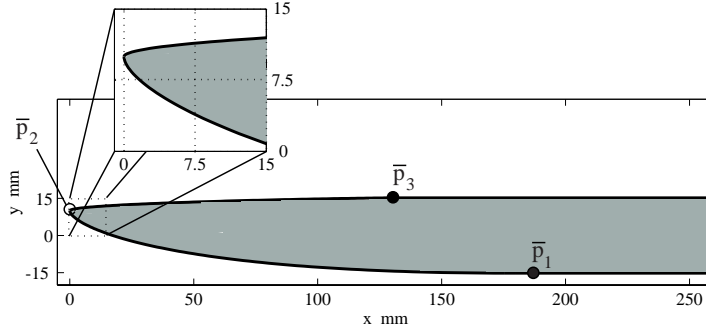


Figure 3.2: Final shape of the leading edge. The profile is described by the Bézier curves  $\bar{r}_l$  and  $\bar{r}_u$  given above.

points were varied for different  $\bar{p}$ -vectors, thereafter the total area was changed again.

After the parameter study, in order to minimize the pressure gradient region, the final shape of the leading edge (lower ( $l$ ) and upper ( $u$ ) part) became

$$\begin{aligned}\bar{r}_l &= (1-t)^3\bar{p}_1 + 3t(1-t)^2\bar{b}_l + 3t^2(1-t)\bar{c}_l + t^3\bar{p}_2, & 0 \leq t \leq 1 \\ \bar{r}_u &= (1-t)^3\bar{p}_2 + 3t(1-t)^2\bar{b}_u + 3t^2(1-t)\bar{c}_u + t^3\bar{p}_3, & 0 \leq t \leq 1\end{aligned}$$

$$\begin{aligned}\bar{b}_l &= \bar{p}_1 + \alpha_l\bar{K}_{1l}; & \bar{b}_u &= \bar{p}_2 + \alpha_u\bar{K}_{1u}; \\ \bar{c}_l &= \bar{p}_2 - \gamma_l\bar{K}_{2l}; & \bar{c}_u &= \bar{p}_3 - \gamma_u\bar{K}_{2u};\end{aligned}$$

$$\bar{p}_1 = [0.18 \quad -0.015]; \quad \bar{p}_2 = [0 \quad 0.01]; \quad \bar{p}_3 = [0.13 \quad 0.015];$$

$$\begin{aligned}\bar{K}_{1l} &= [-1 \quad 0]; & \bar{K}_{2l} &= [0 \quad 1]; & \alpha_l &= 0.15; & \gamma_l &= 0.0046; \\ \bar{K}_{1u} &= [0 \quad 1]; & \bar{K}_{2u} &= [1 \quad 0]; & \alpha_u &= 0.0033; & \gamma_u &= 0.0110;\end{aligned}$$

and is plotted in figure 3.2. The total dimension of the leading edge is  $260 \times 1200 \times 30$  mm (length  $\times$  width  $\times$  thickness).  $\alpha$  and  $\gamma$  (above) are positive numbers representing the "strength" of the steering points and gives the actual steering points for fixed  $\bar{p}$ -vectors.

In figure 3.3 a view of the flow domain and geometry in the computational box is shown. A homogeneous velocity of 5 m/s was used as inlet condition in all runs, on the walls the 'no slip' condition was used, and the outlet conditions was set by specifying the massflow ratio between outflow I and II.

In figure 3.4 the effect upon the stagnation point is illustrated when increasing the massflow below the plate with 2.5% in each figure from a) to c). The

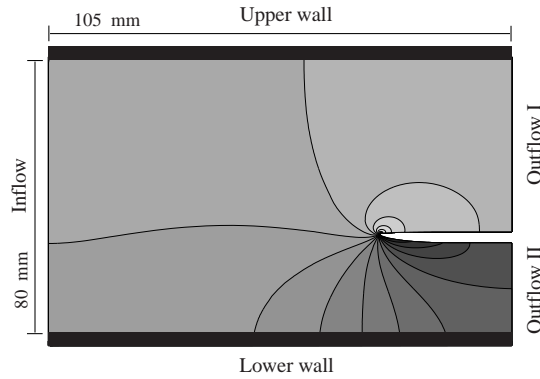


Figure 3.3: View of the computational domain. The filled contour plot shows the pressure distribution in this particular run.

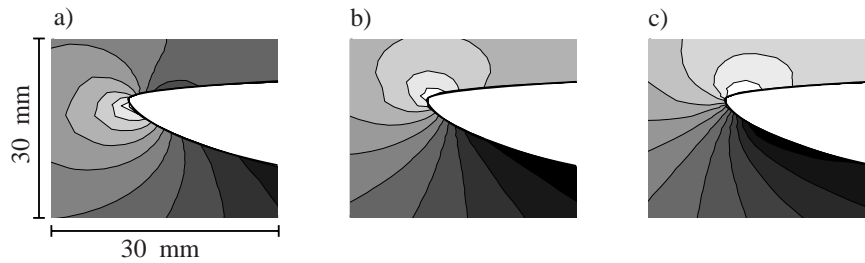


Figure 3.4: Illustration of the effect upon the stagnation point when the mass-flow below the plate is increased 2.5% in each figure from a) to c).

2.5% of massflow change corresponds approximately to a flap angle change of  $1^\circ$  of a one meter long flap. The filled contours shows the pressure distribution with low and high pressures as light and dark colors, respectively.

### 3.1.2. *Experimental verification of the flow around the leading edge*

In figure 3.5 the experimental pressure distribution along the leading edge is shown. The pressure coefficient was calculated from the velocity, i.e. from hot-wire measurements, according to potential flow theory using Bernoulli's equation. The velocity used for this calculation is the velocity just outside the boundary layer and it has been obtained by traversing the probe through the boundary layer and then the position that has a following negligible velocity

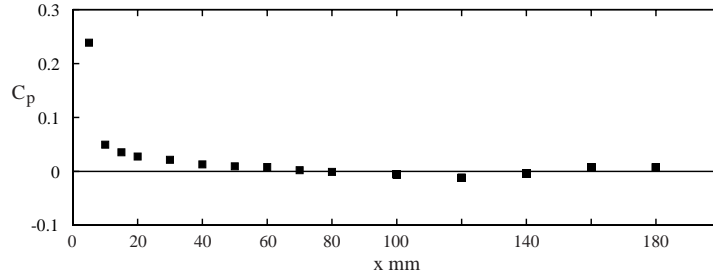


Figure 3.5: Pressure distribution around the leading edge.

change is chosen. The pressure distribution is found to be within  $\pm 0.01$  downstream of  $x = 40$  mm, which is judged to be quite good for a plate of this thickness (= 30 mm).

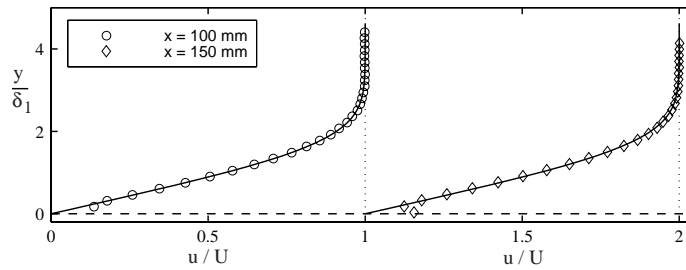


Figure 3.6: Velocity profiles measured relatively close to the leading edge. Solid line is the Blasius profile and the markers denote measured profiles. For  $x=100$  mm  $\delta_1=0.91$  mm and for  $x=150$  mm  $\delta_1=1.14$  mm.

Another check of the flow around the leading edge is how Blasius-like the flow is close to the leading edge. In figure 3.6 two profiles are plotted at  $x=100$  and 150 mm, and these profiles also show that the present design of the leading edge was successful.

### 3.2. Porous material

As a permeable plate a porous plastic material was chosen. Compared to laser drilled plates (discrete holes) it is only one tenth of the price and it has some other advantages. For instance, the plastic material allow quite accurate hot-wire readings close to the wall due to the low heat conductivity, and its pore

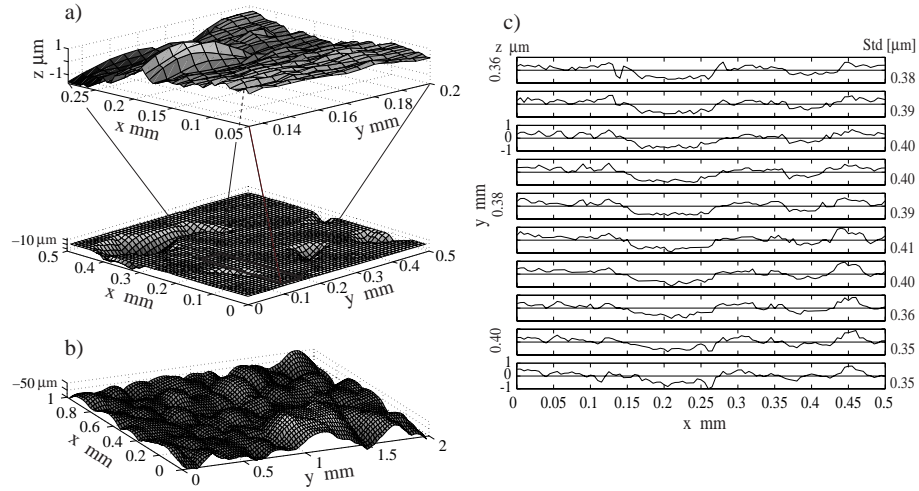


Figure 3.7: Surface roughness measurement of the porous material. a) smooth side with a blow-up area and b) rough side. c) shows the surface traces from a part of the area shown in a).

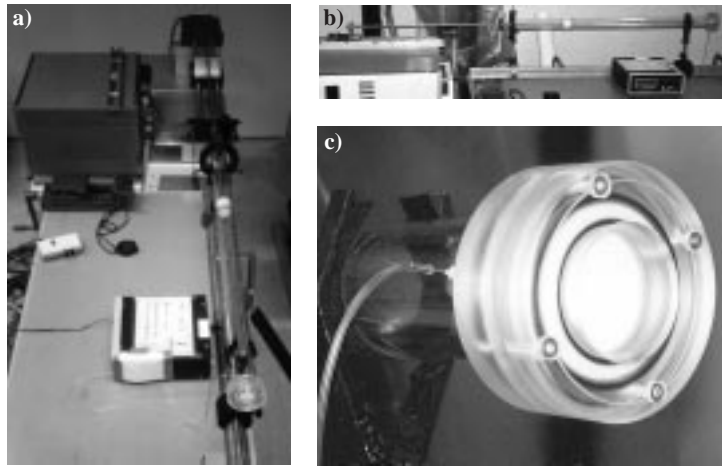


Figure 3.8: Piston-experimental set-up. a) Top view, b) side view and c) end-plug of the Plexiglass pipe.

size and pore spacing is small making the crossflow velocity "uniform" over the surface area which is preferable in this experiment in contrast with what would be obtained in an experiment with a plate with discrete holes.

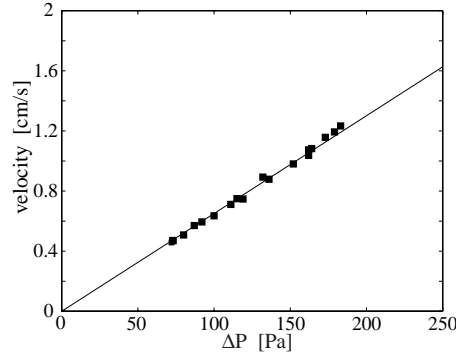


Figure 3.9: Piston-experiment result used to determine the permeability of the porous material.

The porous plates consist of a sintered plastic material with an average pore size of  $16 \mu\text{m}$ . One of the surfaces can be considered smooth and the other rough (the smooth one was used as the upper surface). The standard deviation of the roughness is about  $0.38 \mu\text{m}$  on the smooth side, which was calculated from a surface roughness measurement seen in figure 3.7a) and b) (note the scale). In figure 3.7c) the needle traces from the blow-up area in a) is shown.

The flow properties of the porous material was characterized through a piston-experiment where the permeability of the porous material was determined. This was done by placing a piece of the porous material (thickness  $d$

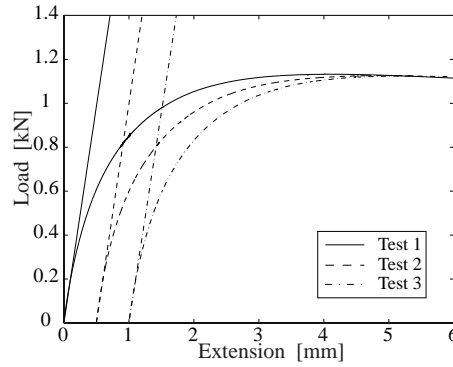


Figure 3.10: Load-test result in where the modulus of elasticity was determined.

= 3.2 mm) at the end of a 0.9 meter, 4 cm diameter Plexiglass pipe and measuring the pressure drop over the porous material when a piston was forced through the pipe with a linear motor (see figure 3.8 for the experimental set-up). This was done at various velocities ( $V$ ) in the range 0.4-1.2 cm/s and it was found that the pressure drop  $\Delta p$  varied in linear proportion to the flow velocity through the material (see figure 3.9 for the measurement result). From this the permeability ( $k$ ) of the material was determined from Darcy's law as  $k = Vd\mu/\Delta p$  where  $\mu$  is the dynamic viscosity. From these measurements it was found to be  $k = 3.7 \times 10^{-12} \text{m}^{-2}$ .

A load-test of the porous material was performed in order to be able to design the inner structure of the plate such that the surface deformation was sufficiently small when suction was applied. Three tests (shown in figure 3.10) were performed and the average modulus of elasticity was determined to be 973.6 MPa. On the suction side longitudinal T-profiles with a certain spanwise interval distance supported the plate. The spanwise distance ( $L_s$ ) between the T-profiles, supporting the porous plates, was then determined by assuming a 1.5 kPa pressure on the plate with a restriction of a bending deviation ( $w_b$ ) of less than 1% of the boundary layer thickness (being 5 mm resulting in  $w_b = 50 \mu\text{m}$ ). This gave  $L_s = 58 \text{ mm}$  and the  $L_s$  finally used was 50 mm. Since the actual pressure difference that was applied in the final experiment was about 200-250 Pa there was some margin in the load assumption.

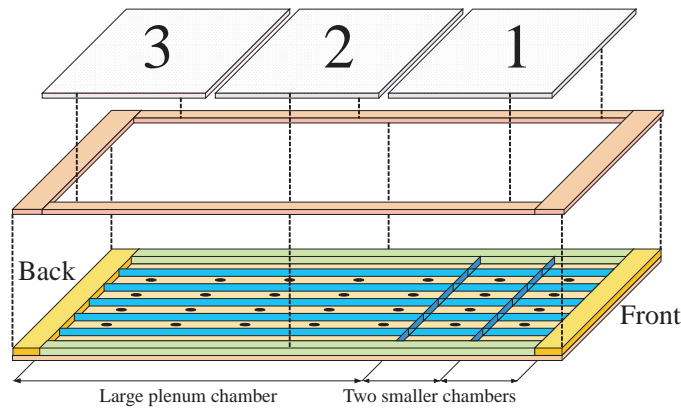


Figure 3.11: Schematic view of the plate construction. See text for comments.

### 3.3. Plate construction

The test plate is built as a sandwich-construction and a schematic is shown in figure 3.11. In the front of the plate the removable leading edge is mounted and

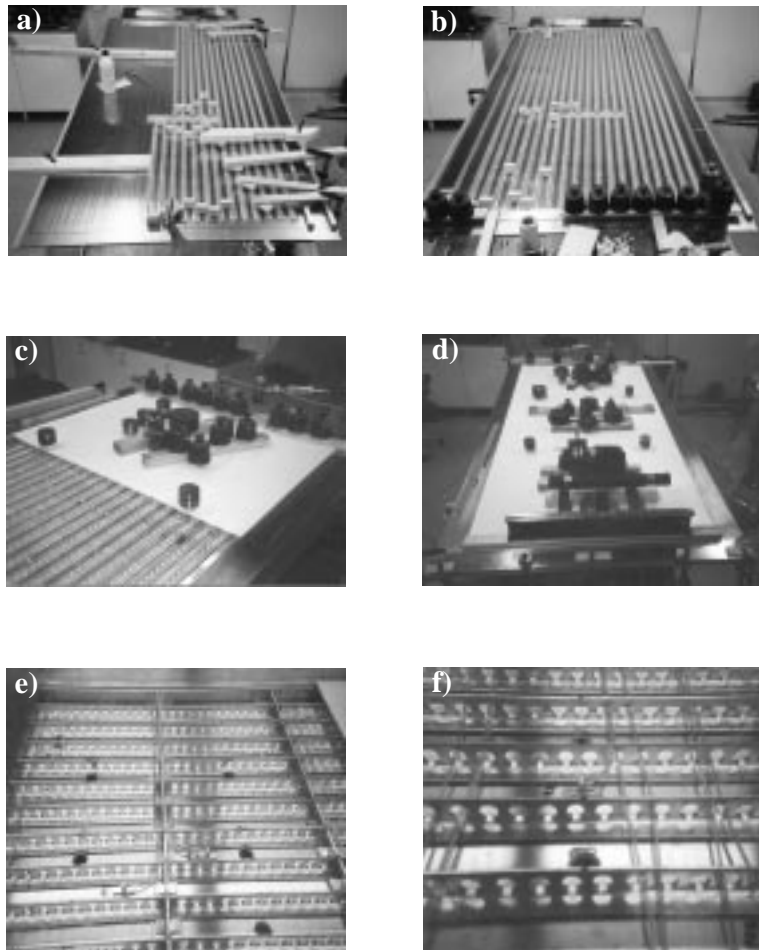


Figure 3.12: Photos of the construction work (a-d). Photo e) shows the two front plenum chambers together with the larger spanwise drilled suction holes. Photo f) is a zoomed piece of e) where the hollowed T-profiles and the pressure tubing for the static pressure holes are shown.

in the back there is a possibility to extend the plate by additional plates of aluminum. The plate is constructed on a base plate of aluminum with a frame, and is designed having two 250 mm long plenum chambers starting 360 mm from the leading edge followed by a 1750 mm long plenum chamber. The subdivision into three chambers is for future work in where the suction rate then is allowed to change with the downstream distance. Inside the plenum chamber distance

elements made of hollowed T-profiles are glued, with a spanwise separation of 50 mm, in order to support the porous plates and avoid bending the plates when suction is applied. On these T-profiles three porous plates with the total dimension  $3.2 \times 2250 \times 1000 \text{ mm}^3$  (thickness, length, width) were mounted into the frame plate. On a spanwise line in the base plate five large holes (30 mm) were drilled at nine positions to where nine suction channels were connected. This was sufficient to achieve uniform pressure in the plenum chamber. In the chamber the static pressure could be measured at 40 well distributed positions giving information of the uniformity of the pressure. In figure 3.12 photos are shown of the construction process work. The two front chambers are seen in 3.12e) as well as the larger spanwise distributed suction holes. Finally, the finished plate mounted in the test-section of the MTL windtunnel is shown in figure 3.13.

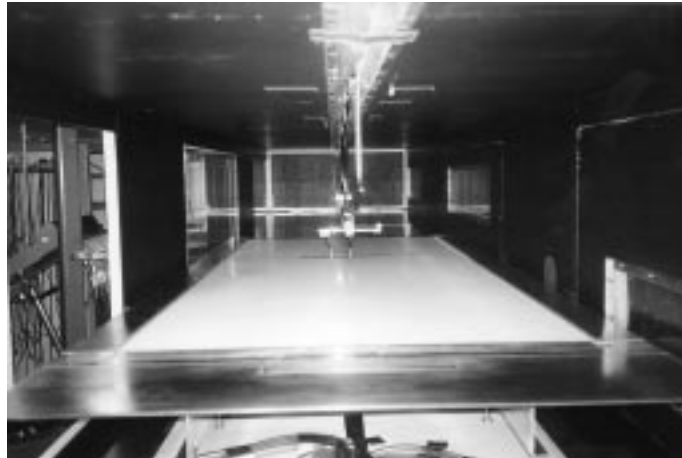


Figure 3.13: Photo of the plate together with the leading edge mounted in the windtunnel.

### 3.4. Experimental set-up

The experiments were carried out in the MTL-wind tunnel at KTH. The test section is 7 m long, 0.8 m high and 1.2 m wide. The wind tunnel has a 5 degree of freedom traversing mechanism, which is convenient for boundary layer traverses as well as X-probe calibration.

A schematic of the experimental set-up is shown in figure 3.14, and is divided into two figures showing the Free Stream Turbulence (FST) experimental set-up and the Tollmien-Schlichting (TS) wave experimental set-up in a) and b), respectively. Everything present in a) is also present in b) except for the

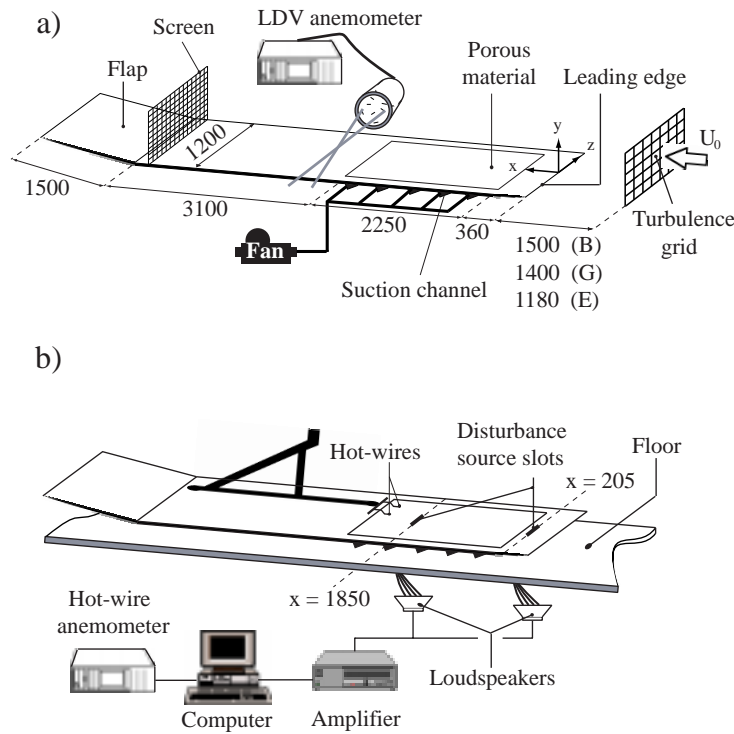


Figure 3.14: Schematic of the experimental set-up. a) The three turbulence generating grids give different turbulence intensities at the leading edge.  $Tu_B = 1.4\%$ ,  $Tu_E = 4.0\%$  and grid G being an active grid was used at  $Tu_G = 2.2\%$ . b) 2D-waves were generated through two different slots in the plate.

turbulence generating grids. Laser Doppler Velocimetry (LDV) measurements were only carried out in the FST experiments, whereas hot-wire measurements were carried out in both experiments. A fine-meshed screen was installed at the end of the test section just upstream the trailing edge flap (going into the diffuser). The screen was needed to compensate for the extra blockage below the plate due to suction channels and tubing. In the present experiments the wind tunnel ceiling was adjusted so that the pressure gradient along the test section was close to zero for the no suction (Blasius flow) case. When suction was applied less than 1 % of the flow in the test section was removed. This gives rise to a slight adverse pressure gradient, however the effect on the mean boundary layer flow is very small as compared to the suction itself. The suction is achieved by a centrifugal fan positioned outside the test-section and is

connected through a stagnation chamber to the suction channels underneath the plate with vacuum cleaner tubing.

Free stream turbulence was generated by three different grids (two passive, B and E, and one active, G) mounted at different distances from the leading edge. The grids gave turbulence intensities ( $Tu = u_{rms}/U_\infty$ ) at the leading edge of the plate of 1.4%, 4.0% and 2.2%, respectively. In appendix B the active turbulence generating grid, injecting secondary fluid upstream and in that way allowing different  $Tu$ -levels, is described separately showing its characteristics.

TS-waves were generated by alternating suction and blowing at the wall through a slot in a plug mounted in the plate. The slot is 330 mm long in the spanwise direction and 0.8 mm thick. Two plugs (slots) are present, one in the removable leading edge at  $x=205$  mm from the leading edge and one at  $x=1850$  mm for disturbance investigation in the fully developed asymptotic suction boundary layer. At this second plug the porous plate was made impermeable by putting a tape underneath the plate over the 50 mm in the the flow direction over the whole spanwise width (in order to keep the two-dimensionality of the flow) where the plug was located. The disturbance signal was generated by the computer through a D/A-board to an audio amplifier driving the loudspeakers. The loudspeakers are connected to the disturbance source through ten flexible tubes. A more thorough description of the disturbance generating system can be found in Elofsson (1998).

### 3.5. Measurement techniques

#### 3.5.1. Hot-Wire Anemometer (HWA)

Single hot-wire probes operating in CTA mode were used to measure the streamwise velocity components. One probe could be traversed in all three spatial directions whereas a second probe was located at a specific spanwise position (in the centre of the tunnel). Both probes were traversed in the  $x$  and  $y$ -directions by the same traversing system and their  $x$  and  $y$  positions were the same. This made it possible to make two-point spanwise space correlation measurements.

The single probes were made of  $2.5 \mu\text{m}$  platinum wires with a distance between the prongs of approximately 0.5 mm. The calibration function according to Johansson & Alfredsson (1982) was used, where an extra term is added to King's law for compensation of natural convection which makes it suitable for low speed experiments and is shown below,

$$U = k_1(E^2 - E_0^2)^{1/n} + k_2(E - E_0)^{1/2}.$$

In the HWA-technique an X-probe was also used to measure the streamwise and wall-normal velocity components operating in CTA mode. The probe was made of  $2.5 \mu\text{m}$  platinum wires and had a measurement volume less than  $1 \text{ mm}^3$  (side length  $\leq 1 \text{ mm}$ ). The calibration was done at different angles and flow

velocities, and then two 2D fifth-order polynomials were fitted to the calibration data, giving  $U$  and  $V$  as functions of the obtained voltage pair  $(E_1, E_2)$ . This calibration procedure is described in detail by Österlund (1999).

### 3.5.2. *Laser Doppler Velocimetry (LDV)*

In the LDV-measurements an integrated one dimensional laser-optics unit was used, including a 10 mW He-Ne laser of wavelength 632.8 nm. A beam expander was mounted to the lens to reduce the measurement volume, which can be approximated as an ellipsoid with axes lengths 0.14 mm and 2.4 mm. To be able to measure the wall-normal component close to the wall the probe has to be inclined. This causes an error which in the present case was estimated to be less than 0.2%. To provide a uniform seeding smoke from a smoke generator was injected downstream of the test section in the closed-loop wind tunnel.

The LDV-data presented are residence time weighted, i.e. each particle is weighted with its transit time. The LDV-unit only allows fixed bandwidths to be changed by the user, and the choice influences the background noise level in the measured data. In the present flow case with a dominant mean flow direction along  $x$  it was possible to choose a more narrow (and better suited) bandwidth for the wall-normal component than for the streamwise one. In the present study two different bandwidths were used for the measurements of the streamwise component.

## CHAPTER 4

### Experimental results

In the following chapter the experimental results will be shown and discussed. The results are divided into three main parts. First of all the Blasius boundary layer will be presented showing the base flow properties and Tollmien-Schlichting (TS) wave experiments. Then the evolution region (from the Blasius to the asymptotic suction state) followed by TS-wave experiments in the asymptotic suction region will be shown, and finally free stream turbulence (FST) experiments will be presented where the Blasius and the asymptotic suction results are chosen to be presented together for direct comparisons.

The experiments reported here were made at a free stream speed of 5.0 m/s and a suction speed of 1.44 cm/s by applying a pressure difference over the porous plate of  $\Delta p=221$  Pa. This gives an asymptotic boundary layer

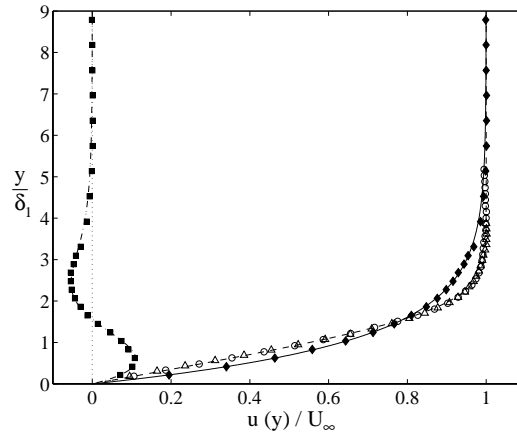


Figure 4.1: Velocity profiles for the Blasius and the asymptotic suction boundary layers. No suction (unfilled-), suction (filled markers) and theory (lines). Asymptotic suction profile (solid line) ( $\diamond$ ) at  $x = 1800$ , Blasius profiles (dashed line) ( $\circ$ ) at  $x = 300$  mm and ( $\triangle$ ) at  $x = 1800$  mm. ( $\blacksquare$ ) is the mean deviation (dash-dotted line).

thickness of 5 mm and a Reynolds number based on the displacement thickness of 347. In figure 4.1 both experimental data and the theoretical distribution are plotted for the Blasius profile measured at  $x=300$  and  $x=1800$  mm and the asymptotic suction profile measured at  $x=1800$  mm. The agreement between the three experimental profiles and the corresponding theoretical profiles are excellent. Even at  $x=1800$  mm the measured Blasius profile agrees well with theory indicating a steady Blasius boundary layer throughout the measurement area when no suction is applied. It is notable that the hot-wire reading very close to the wall is quite accurate, making it possible to measure velocities down to 0.5 m/s without any discrepancy from the theoretical curve. This is due to the calibration function as well as the low heat conductivity of the porous material. Also plotted is the deviation between the suction profile and the Blasius one which clearly reveals the fuller shape of the suction profile.

#### 4.1. TS-waves in a Blasius boundary layer

In order to verify the flow set-up, measurement technique and disturbance generation, the stability characteristics of the Blasius boundary layer for 2D-wave disturbances were determined and compared with previously reported results from the MTL-wind tunnel.

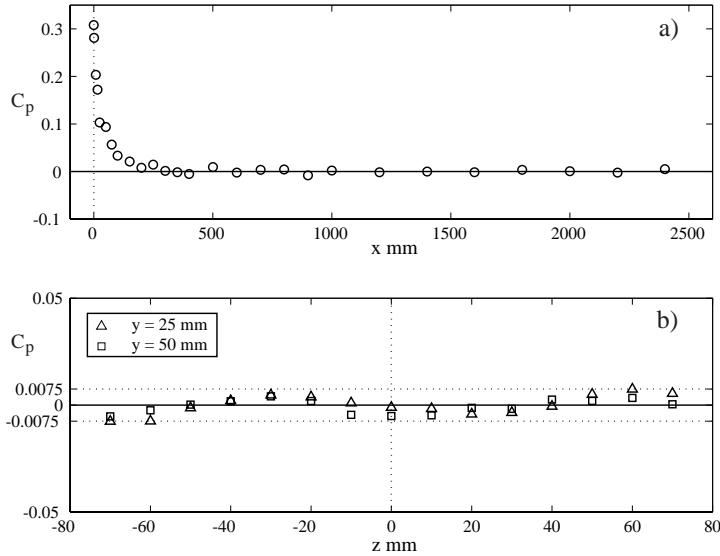


Figure 4.2: Pressure distribution in the test-section. a) Streamwise direction, and b) spanwise direction at  $x = 300$  mm.

## 4.1.1. Base flow properties

In figure 4.2a) the streamwise pressure distribution is plotted for the whole investigated downstream distance on the flat plate, and in b) the spanwise pressure distribution is plotted over a spanwise distance of 140 mm at  $x=300$  mm for two different  $y$ -positions in the free stream.

The relatively long pressure gradient region observed in figure 4.2a), compared to what was shown in figure 3.5, is due to the thickening of the plate due to suction channels and tubing underneath the plate that are present in this experiment. The suction channels alone contributes to an extra vertical blockage of 35 mm.

For a zero pressure gradient boundary layer on flat plate the Blasius profile is accomplished and in figure 4.3 measured profiles (markers) for different streamwise and spanwise positions are compared with the Blasius solution (solid

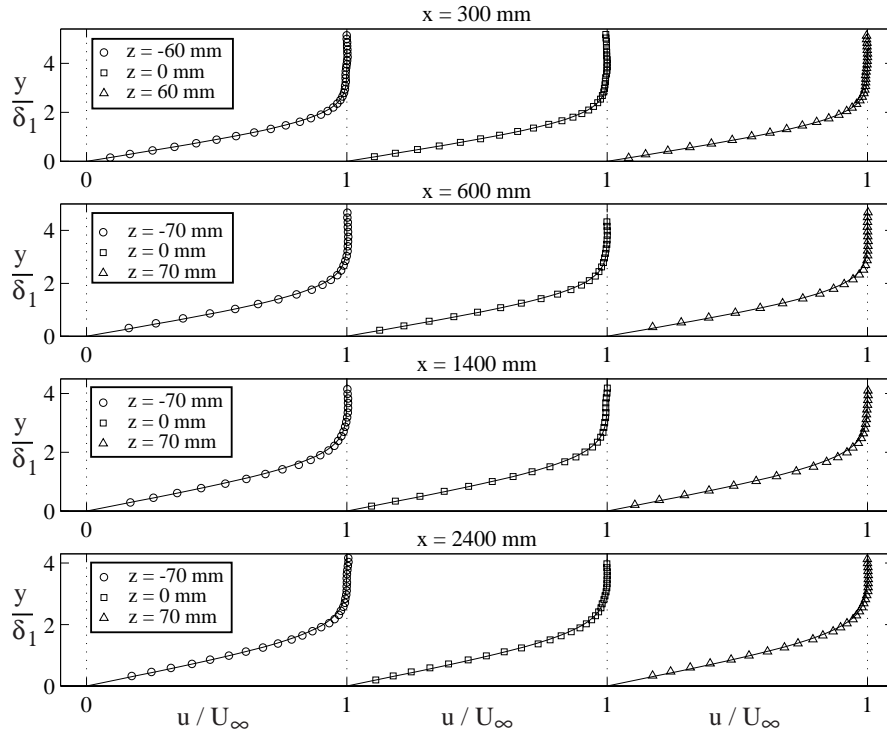


Figure 4.3: Base flow profiles for different streamwise and spanwise positions. Markers are measured profiles and solid lines are the Blasius solution.

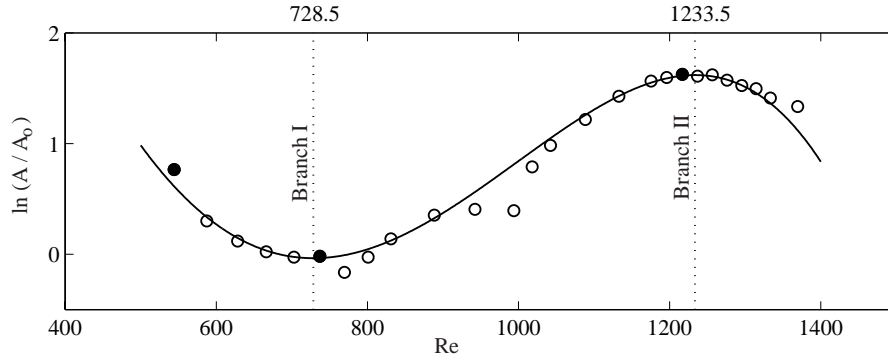


Figure 4.4: Amplitude evolution of the TS-wave at  $F = 100$ . ( $\circ$ ) experimental results, and solid line linear parallel theory of the Blasius profile.

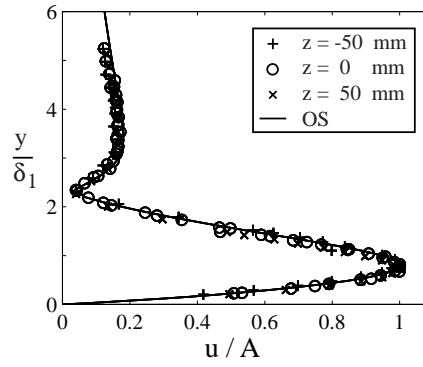


Figure 4.5: Amplitude distribution profile at  $x = 300$  mm and at three different spanwise positions for  $F = 100$ . Markers belong to experiment and the solid line to the OS-solution.

line). This figure illustrates the two-dimensionality of the flow in question for the whole streamwise distance that are to be examined.

#### 4.1.2. Controlled stability experiments

Controlled stability experiments were performed, where the studied disturbance is generated with a known frequency. The first slot in the leading edge is used to verify the experimental set-up, and the second slot far downstream was used to perform experiments that later will be compared

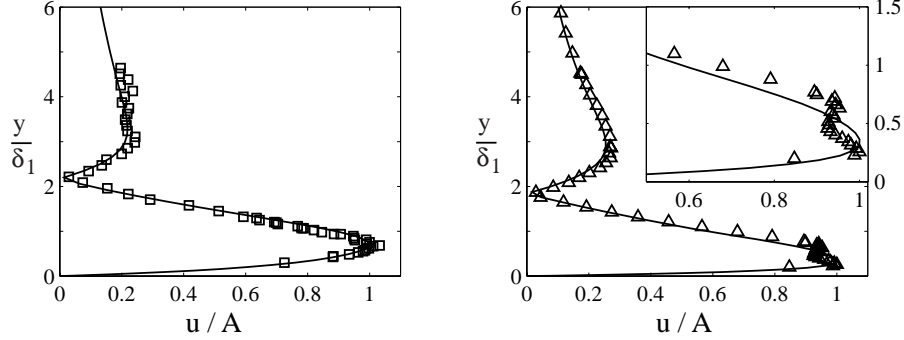
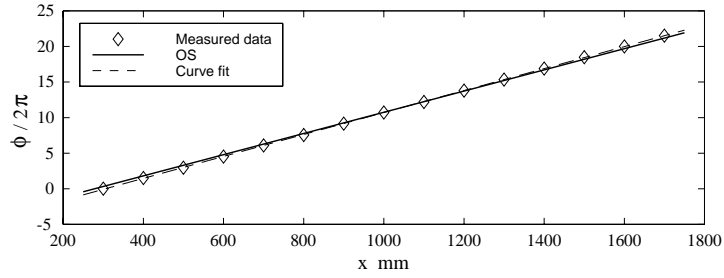
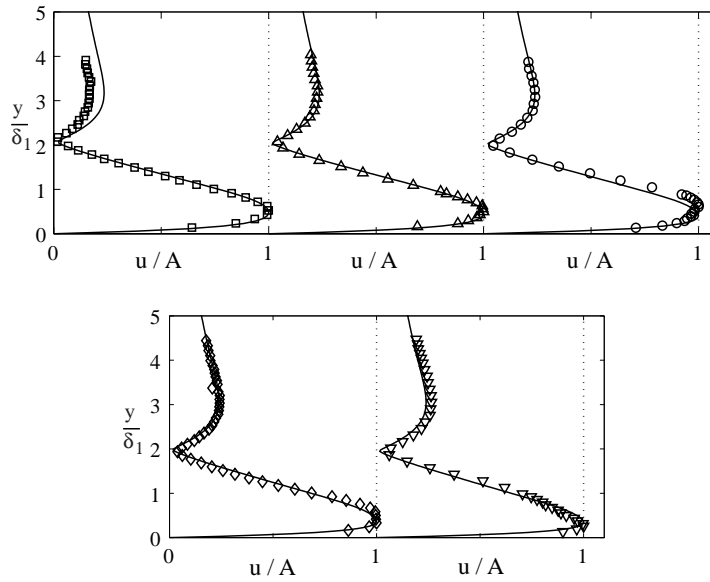


Figure 4.6: Amplitude distribution profiles for  $F = 100$ . a)  $x = 550$  mm ( $A = 0.0036$  m/s), and b)  $x = 1500$  mm ( $A = 0.0210$  m/s).

with the TS-wave study in an asymptotic suction boundary layer. In figure 4.4 the amplitude distribution of the TS-wave at  $F = 100$  is shown (in this and following figures  $A$  corresponds to the maximum measured amplitude in the profile). The experiment (o-markers) shows good agreement with linear parallel theory (solid line), where both the first and the second branch are well captured by the experiment. The TS-wave is generated at  $x = 205$  mm and decays until reaching the first branch at approximately  $Re = 728.5$ . From there on it grows in amplitude until reaching the second branch at approximately  $Re = 1233.5$  where it starts to decay again. In figures 4.5 and 4.6 the disturbance amplitude distribution profiles are shown for the three filled markers ( $\bullet$ ) in figure 4.4. In the former figure the two-dimensionality of the TS-wave is illustrated by plotting the profiles of three different spanwise positions together with the Orr-Sommerfeld (OS) solution, i.e. results from linear parallel theory. The latter figure shows the smallest (least amplified) and the largest (most amplified) profiles, and in a) (at  $x = 550$  mm) the smallness can be revealed in the boundary layer edge where the measured data appear more scattered than in b) (at  $x = 1500$  mm). Furthermore, in b) a deformation of the amplitude distribution at the inner maximum can be seen. This deformation has been observed in previous works, see e.g. Klingmann *et al.* (1993) and Ross *et al.* (1970), at downstream distances far from the disturbance source.

The phase velocity ( $c = \omega/\alpha_r$ ) of the wave can be determined simply by determining the real wave number ( $\alpha_r$ ) since the angular frequency ( $\omega$ ) is known. In figure 4.7 the phase distribution in the streamwise direction is plotted. The phase is taken at the wall-normal distance above the plate where the inner maximum amplitude appears.  $\alpha_r$  is then determined by calculating the phase gradient ( $\partial\Phi/\partial x$ ), and it is seen to be constant throughout the

Figure 4.7: Phase distribution in the streamwise direction at  $F = 100$ .Figure 4.8: Amplitude distribution profiles for  $F = 59$ . ( $\square$ )  $x = 1900$  mm, ( $\triangle$ )  $x = 2000$  mm, ( $\circ$ )  $x = 2200$  mm, ( $\diamond$ )  $x = 2400$  mm, and ( $\nabla$ )  $x = 2600$  mm.

whole investigated downstream distance. The marker is experimental data, the solid curve is the OS-solution, and the dashed line is the curve fit for the determination of the gradient. This curve fit gives us a phase velocity of  $0.34U_\infty$  compared with the theoretical based on the Blasius profile of  $0.36U_\infty$ .

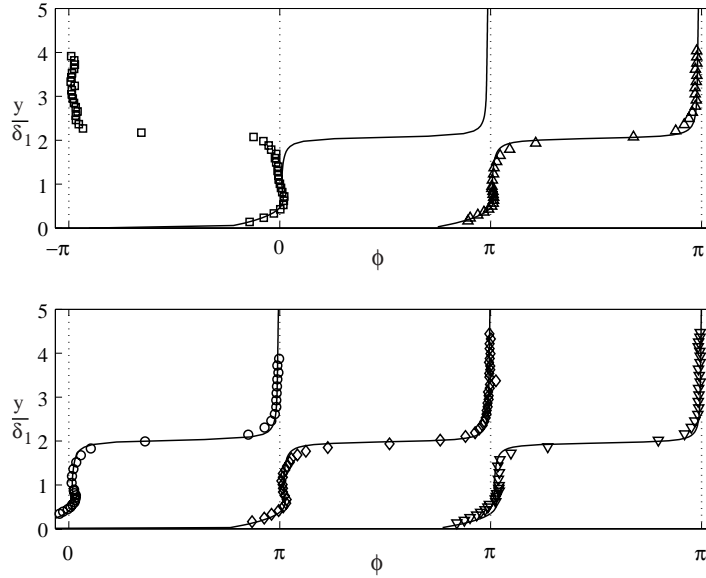


Figure 4.9: Phase distribution profiles for the corresponding  $x$ -positions in figure 4.8. Markers are experimental data and solid line OS-solution.

From now on all stability results are from the second disturbance slot in the plate located at  $x=1850$  mm corresponding to  $Re=1350$ . In figure 4.8 the amplitude distribution profiles are plotted for  $F=59$  at five different downstream positions. The first  $x$ -position closest to the disturbance source, in fact only 50 mm from the source, is not fully developed in the upper part of the profile when compared to the OS-solution. However, from the second  $x$ -position the agreement is excellent in this part.

In figure 4.9 the corresponding phase distribution profiles are plotted, and they clearly show the phase shift of  $\pi$  radians which can be shown to appear where  $\partial v' / \partial y$  changes sign, i.e. at the wall-normal amplitude ( $v'$ ) maxima. The experimental data are in good agreement with the OS-solution (solid line).

For this particular frequency, i.e.  $F=59$ , the TS-wave is unstable. Recall that we are measuring downstream of the second slot which for this low frequency appears to be in between branches I and II. The amplitude growth of the TS-wave is seen in figure 4.10 together with the predicted amplitude evolution by the OS-equation.

The phase velocity for this particular frequency is  $c = 0.29U_\infty$  determined from figure 4.11 and the corresponding phase velocity given by the OS-solution is  $c = 0.33U_\infty$ . However, the agreement has to be judged as good since there

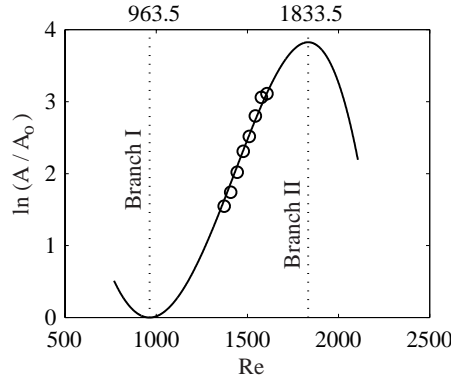


Figure 4.10: Amplitude evolution of the TS-wave at  $F = 59$ . (o) experimental results, and solid line linear parallel theory of the Blasius profile.

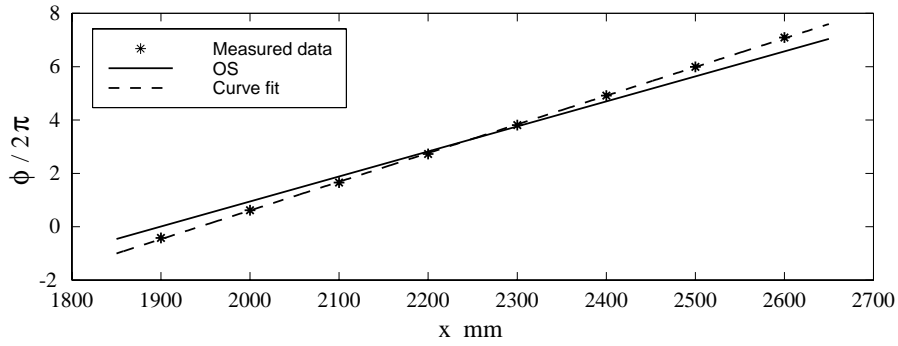


Figure 4.11: Phase distribution in the streamwise direction at  $F=59$ .

are many external conditions that may influence the result this far downstream from the leading edge. When compared with figure 4.7 one can observe that the phase velocity is larger just as for that frequency, but in this case the trend is somewhat stronger and the effect is more apparent.

In figure 4.12 a contour plot of the TS-wave perturbation ( $u = U - \bar{U}$ ) is shown. The time between the different figures is  $\Delta t=8$  ms. In order not to lose contrast in the contourplots there is a colourbar for each figure (note the new interval scale in all figures). The generation of the TS-wave, described in section 3.4, was done through a slot in the plate by alternating blowing and suction. The blowing injects fluid to the flow at the surface whilst the suction

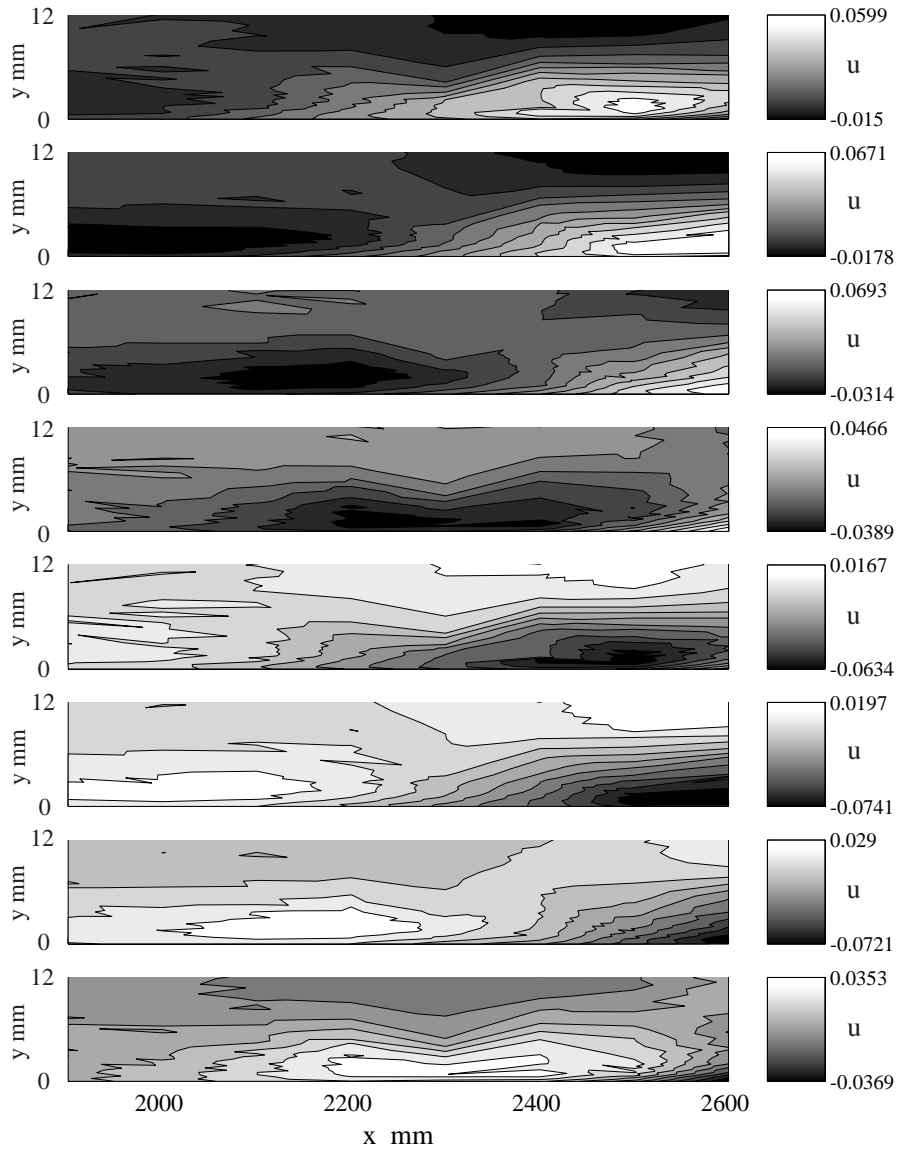


Figure 4.12: Contourplot of the streamwise disturbance velocity of the TS-wave perturbation at  $F=59$  ( $f=15.6$  Hz) in a Blasius boundary layer. The time between the figures is  $\Delta t=8$  ms.

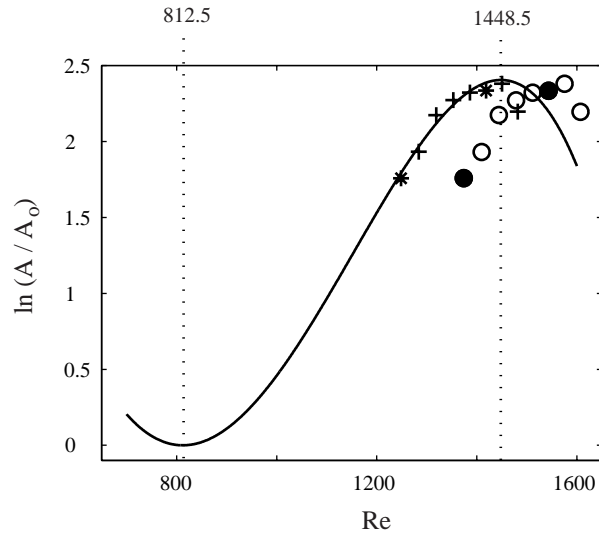


Figure 4.13: Amplitude evolution of the TS-wave at  $F = 81$ . (o) experimental results, and solid line linear parallel theory of the Blasius profile. (+) is the present data but shifted  $\Delta Re = -125$ .

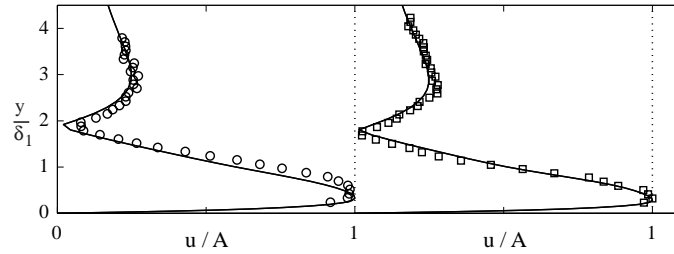


Figure 4.14: Amplitude distribution profiles for  $F = 81$  at the (•)-markers in figure 4.13. (o) at  $x = 1900$  mm and (□) at  $x = 2400$  mm.

removes some fluid, this making the light parts of the contourplot correspond to the blowing and the dark to the suction. As observed in figure 4.10 the TS-wave amplitude grows with the downstream distance making the contrast of the perturbation largest on the right side of the figures. This also makes the phase shift of  $\pi$  radians most visible as far downstream as possible.

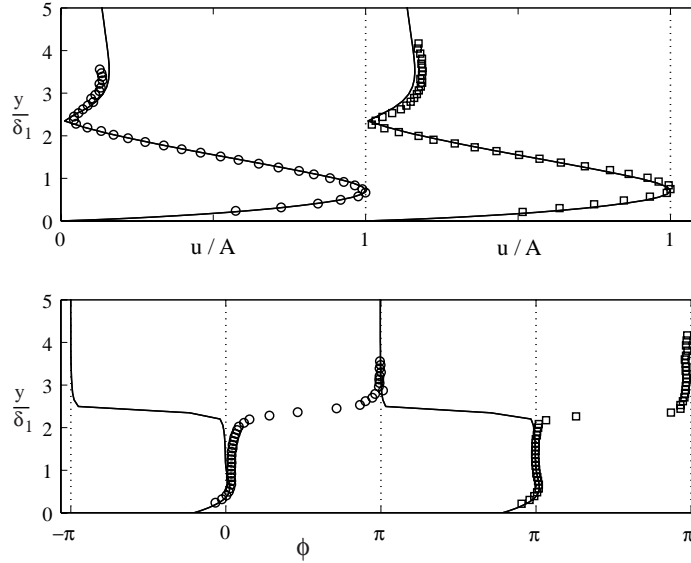


Figure 4.15: Amplitude and phase distribution profiles for  $F = 29$ . ( $\circ$ )  $x = 1900$  mm, and ( $\square$ )  $x = 2400$  mm.

Results from two other frequencies,  $F = 81$  and  $F = 29$ , are also shown here. In figure 4.13 the amplitude evolution of the TS-wave is shown for the higher frequency. ( $\circ$ ) belongs to measured data and ( $+$ ) are the same data but shifted  $\Delta Re = -125$  which is needed for collapse with the OS-solution (solid line). This can just as well be the case for  $F = 59$  in figure 4.10, i.e. that a shift is needed, but can not be detected in that case since there is no amplitude reference point. In the present figure (4.13) we are close to the second branch and a clear decay of the amplitude growth is visible making it impossible to fit the experimental data to the OS-solution without a shift in the Reynolds number. The shift corresponds to a virtual ( $v$ ) origin at  $x_v = -15.8$  mm, which can be considered small. In figure 4.13 two of the markers are filled ( $\bullet$ ) and in figure 4.14 the whole amplitude distribution profiles are plotted for these  $x$ -positions, i.e. at  $x = 1900$  mm and  $x = 2400$  mm.

At the lower frequency ( $F = 29$ ) the amplitude distribution profiles does not look as scattered as for the higher frequency. In figures 4.15 these profiles are plotted together with their corresponding phase distribution profiles.

4.1.3. *Conclusions*

All the results so far indicate that the porous plate itself does not seem to effect the stability characteristics of the boundary layer flow. The amplitude growth of the TS-wave corresponds well with linear parallel theory just as well as the amplitude and phase distribution profiles do.

Investigation of high Reynolds numbers, when the second slot in the plate is used for disturbance generation, reveals that there is a need for a correction of the origin, i.e. an introduction of a virtual origin at  $x = -15.8$  mm, for agreement with linear parallel theory. The larger disagreement of the phase velocity, compared to experiments using the first slot, can however not be explained by the virtual origin since the real dimensional wave number used for determining  $c$  is Reynolds number independent. On the whole one may say that the agreement with linear parallel theory is good even for the second slot experiments, since there are many potential factors that can influence the stability characteristics this far downstream from the leading edge and one should remember that the OS-solution is based on the perfect Blasius profile.

4.2. **TS-waves in an asymptotic suction boundary layer**

In the following section the base flow when continuous suction is applied will be presented together with TS-wave experiments in the fully developed asymptotic suction region. The agreement with linear parallel theory together with potential sources that contributes to the deviations will be discussed.

4.2.1. *Base flow properties and the evolution region*

For the present experiments the flat plate and wind tunnel test section were adjusted for zero-pressure gradient with no suction through the plate. Much effort was spent in order to achieve the zero pressure gradient by changing the floor and ceiling positions of the test-section. Recall that the thick plate

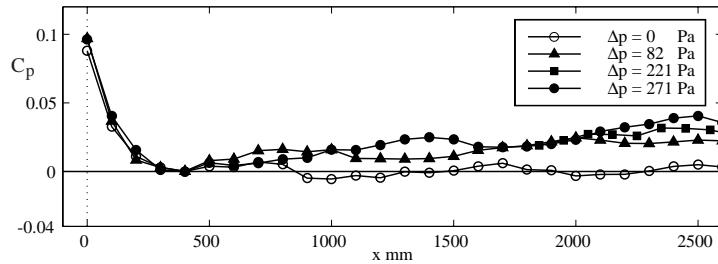


Figure 4.16: Pressure distribution along the streamwise direction for different suction rates.

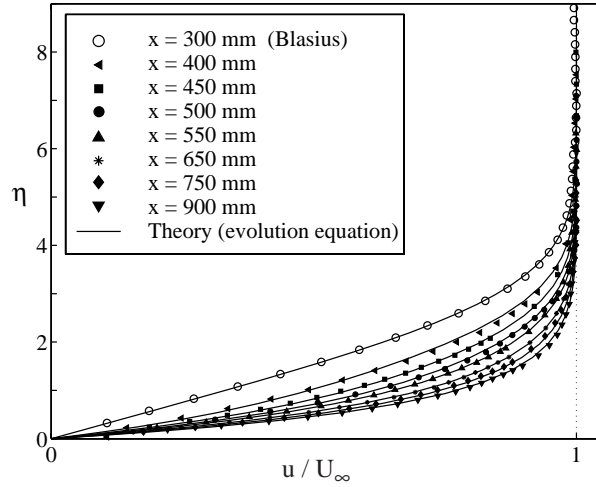


Figure 4.17: Experimental data versus the evolution equation (discussed in section 2.3) in the evolution region.  $\eta = y\sqrt{\frac{U_\infty}{x\nu}}$ .

together with its suction channels and additional blockage due to suction tubing makes the adjustments more difficult. Therefore, no additional geometrical adjustments of the test-section were done for the suction case. The result of different suction rates on the pressure distribution along the streamwise direction is shown in figure 4.16. In the experimental results that are presented in this thesis a pressure difference ( $\Delta p$ ) over the porous plate of 221 Pa was kept, which corresponds to a suction velocity of 1.44 cm/s using the permeability value determined through the piston-experiment described in section 3.2. Note that the total pressure change is less than 3% for this  $\Delta p$ .

In figure 4.17 several velocity profiles are plotted in the evolution region, where the wall-normal distance  $\eta$  ( $= y\sqrt{\frac{U_\infty}{x\nu}}$ ) is chosen in order to clearly follow the profile evolution. The development of the boundary layer from the Blasius towards the asymptotic profile shows good agreement with theory, i.e. the evolution equation, and can be observed in figure 4.18 (note the scaling). The dash-dotted lines are from the Blasius solution and the solid lines originate from the evolution equation.

The uniformness and two-dimensionality of the flow was checked in the asymptotic suction region by comparing the velocity profiles at different spanwise and downstream positions. These profiles are shown in figure 4.19 together with the theoretical exponential profile (solid line).

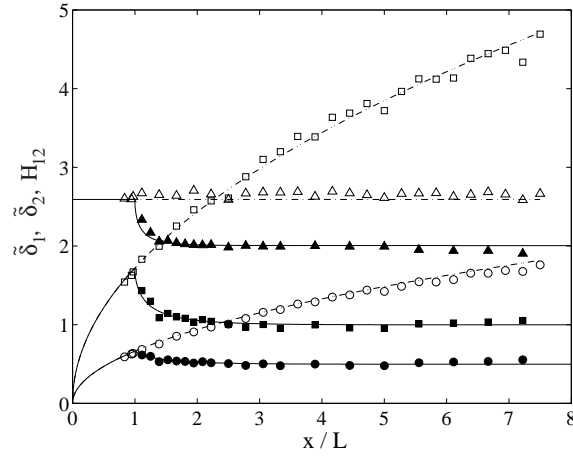


Figure 4.18: Experimental and theoretical results of integral boundary layer parameters. No suction (unfilled-) and suction (filled markers). ( $\square$ )  $\delta_1$  and ( $\circ$ )  $\delta_2$  are the displacement- and momentum thickness, respectively, normalized with  $\frac{1}{L}(\frac{U_\infty L}{\nu})^{1/2}$ . ( $\triangle$ )  $H_{12}$  is the shape factor.

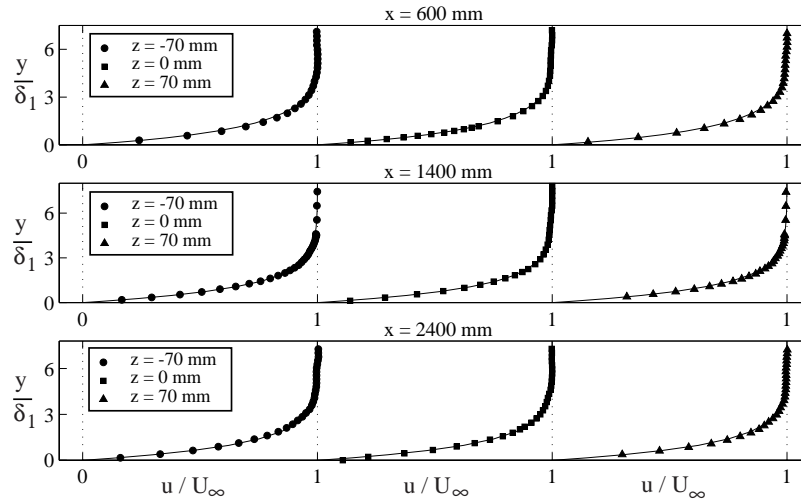


Figure 4.19: Asymptotic suction profiles at different spanwise positions for three different downstream positions.

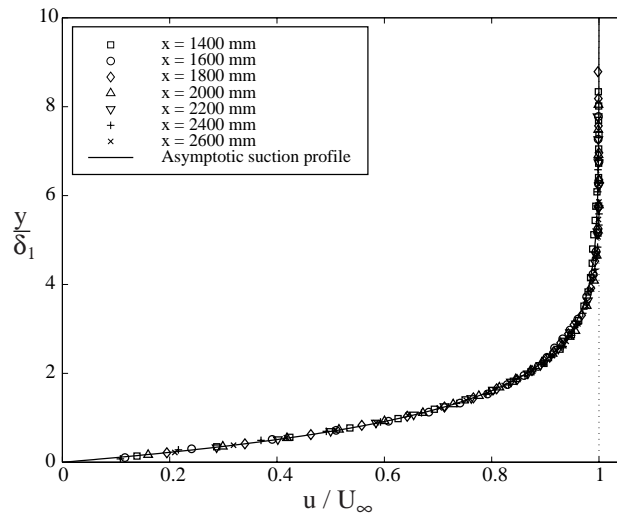


Figure 4.20: Mean velocity profiles for different downstream positions in the asymptotic suction boundary layer.

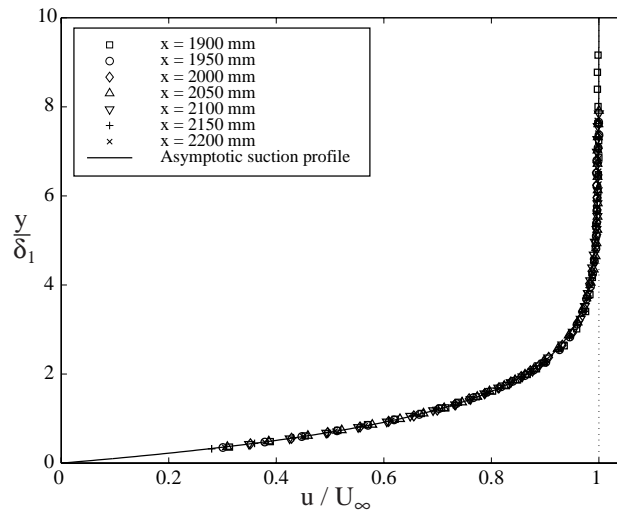


Figure 4.21: Mean velocity profiles for different downstream positions in the visible TS-wave decay region.

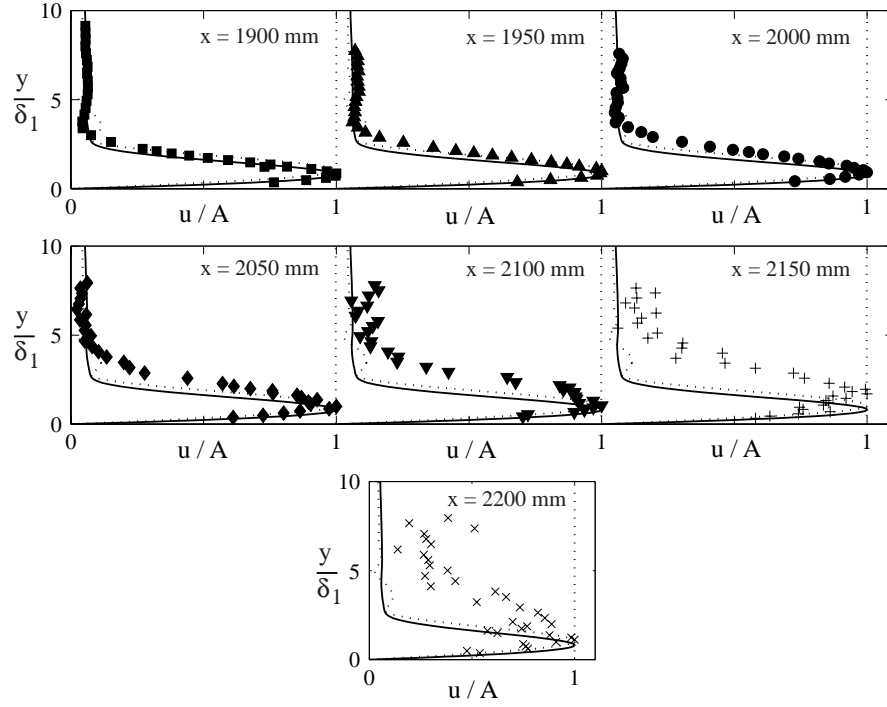


Figure 4.22: Amplitude distribution profiles for different downstream positions in an asymptotic suction boundary layer for  $F=59$ . Markers are measured data, solid line is the modified OS-solution, and dotted line the OS-solution.

In figure 4.20 seven downstream positions are plotted showing total collapse of the profiles on the theoretical curve, i.e. the analytical asymptotic suction profile. The wall position ( $y_0$ ) and the displacement thickness ( $\delta_1$ ) were determined by fitting the experimental data to

$$\frac{u(y)}{U_\infty} = 1 - e^{-(y-y_0)/\delta_1}$$

by means of least square method. This is also a way to verify the actual suction velocity through the porous plate with the suction velocity corresponding to the pressure difference applied. Since the displacement thickness is exact, namely  $\delta_1 = \nu/V_0$ , the suction velocity can easily be calculated once the  $\delta_1$  is determined from the curve fit. Any profile chosen to verify the 1.44 cm/s applied agrees within 9%.

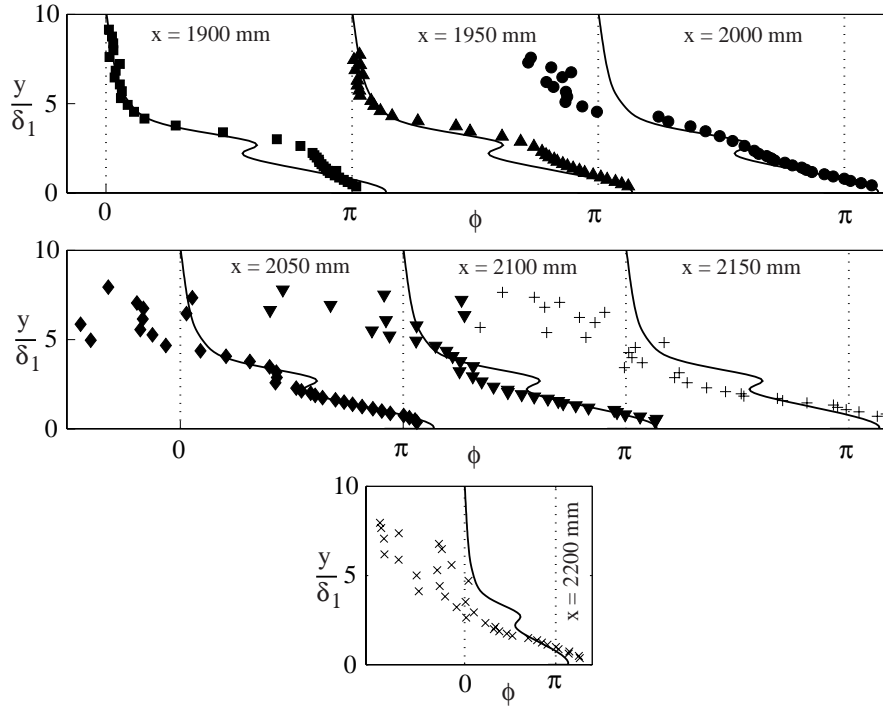


Figure 4.23: Corresponding phase distribution profiles to figure 4.22.

#### 4.2.2. Controlled stability experiments

The Reynolds number based on the displacement thickness is directly determined by the ratio between the free stream velocity and the suction velocity (see section 2.6.1), which implies that the Reynolds number is constant throughout an asymptotic suction boundary layer. This makes the stability analysis rather special, since there is no downstream distance dependence on the main flow, there is no effect from a growing boundary layer as in the Blasius boundary layer. However, the  $V$ -component may not longer be neglected as in the Blasius boundary layer resulting in a modified OS-equation for the stability characteristic comparison.

The displacement thicknesses determined throughout the asymptotic suction region is fairly constant which can be seen in figure 4.20, but in the end part of the region roughly 200 mm after the second slot in the plate the displacement thickness experiences a small increase above the mean value. This making a direct change in the Reynolds number changing the stability characteristics of the overall region. However, there is no need to worry about having lost the

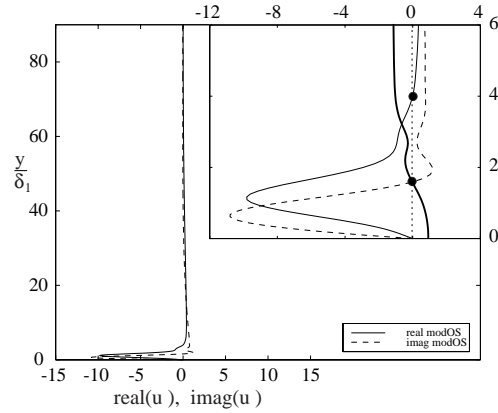


Figure 4.24: Real and imaginary parts of the amplitude distribution profile. The (•)-markers indicate the zero-crossing and the bold line the phase distribution.

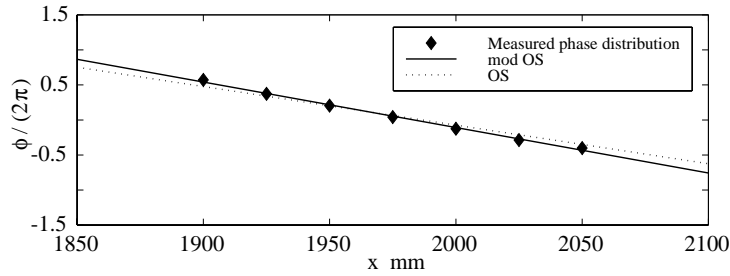


Figure 4.25: Phase distribution in the streamwise direction at  $F=59$  in the asymptotic suction boundary layer.

exponential velocity profile after checking the mean profiles in the area where the TS-waves will be generated, see figure 4.21 for mean velocity profiles from the TS-wave measurements. The slightly larger value of  $\delta_1$  in this region gives a somewhat smaller suction velocity which contributes to a larger Reynolds number than what was proposed in the introduction part of this chapter. The Reynolds number used in the theoretical stability analysis is 382 compared to the previous determined  $Re=347$ , i.e. 10% larger. The effect is though rather small since it is still extremely far away from the unstable region with a critical Reynolds number of two orders of magnitude larger ( $R_{cr} = 54382$ ).

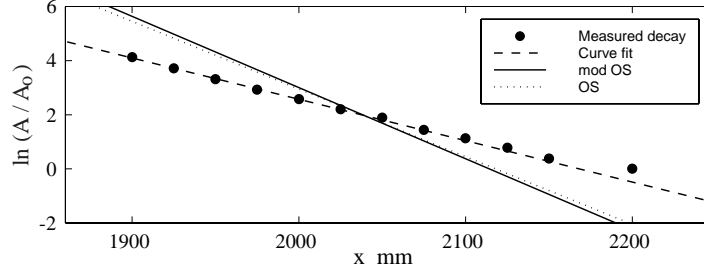


Figure 4.26: Amplitude decay versus the downstream distance for  $F=59$ .

For the present  $Re$  the TS-wave will decay rapidly after its generation. In figure 4.22 the amplitude distribution profiles are shown for different downstream positions. The solid line is the solution from the modified OS-equation and the dotted is the ordinary OS-equation. Note that the last profile shown is only 350 mm from the disturbance source. Close to the disturbance source the experimental results show quit good agreement with the modified OS-solution. But very soon the disturbance is seen to be spread out towards the upper part of the boundary layer and from  $x=2100$  mm the measured data starts to appear somewhat scattered. The corresponding phase distribution profiles are plotted in figure 4.23 with the solid line belonging to the modified OS-solution. The agreement is good in the upper part of the boundary layer and in the free stream, but in the theoretical phase distribution there is z-formation in the middle of the boundary layer that is not seen in the experimental results. This z-formation is understood if a look is taken to the real and imaginary parts of the amplitude distribution profile in figure 4.24. It is the quotient between the imaginary and real part of the eigenfunction that determines the shape of the phase distribution and it is the large decrease with a minimum of this quotient at  $y/\delta_1 = 2.7$  followed by an increase that contributes to the z-formation, i.e. it is the undulation of the imaginary part in this  $y/\delta_1$ -region that gives rise to the z-formation.

The phase velocity of the TS-wave with  $F=59$  is determined in figure 4.25. The solid line is the modified OS-solution and this solution almost corresponds to a curve fit to the measured data. The dotted line is the ordinary OS-solution. The experimental phase velocity is determined to be  $c = 0.48U_\infty$ , which is the phase velocity predicted by the modified OS-solution.

The amplitude decay is shown in figure 4.26 together with theoretical results. The theoretical results overpredicts the stability of the TS-wave. The experimental result gives a damping factor of  $\alpha_i = 0.0153 \text{ mm}^{-1}$ , when the

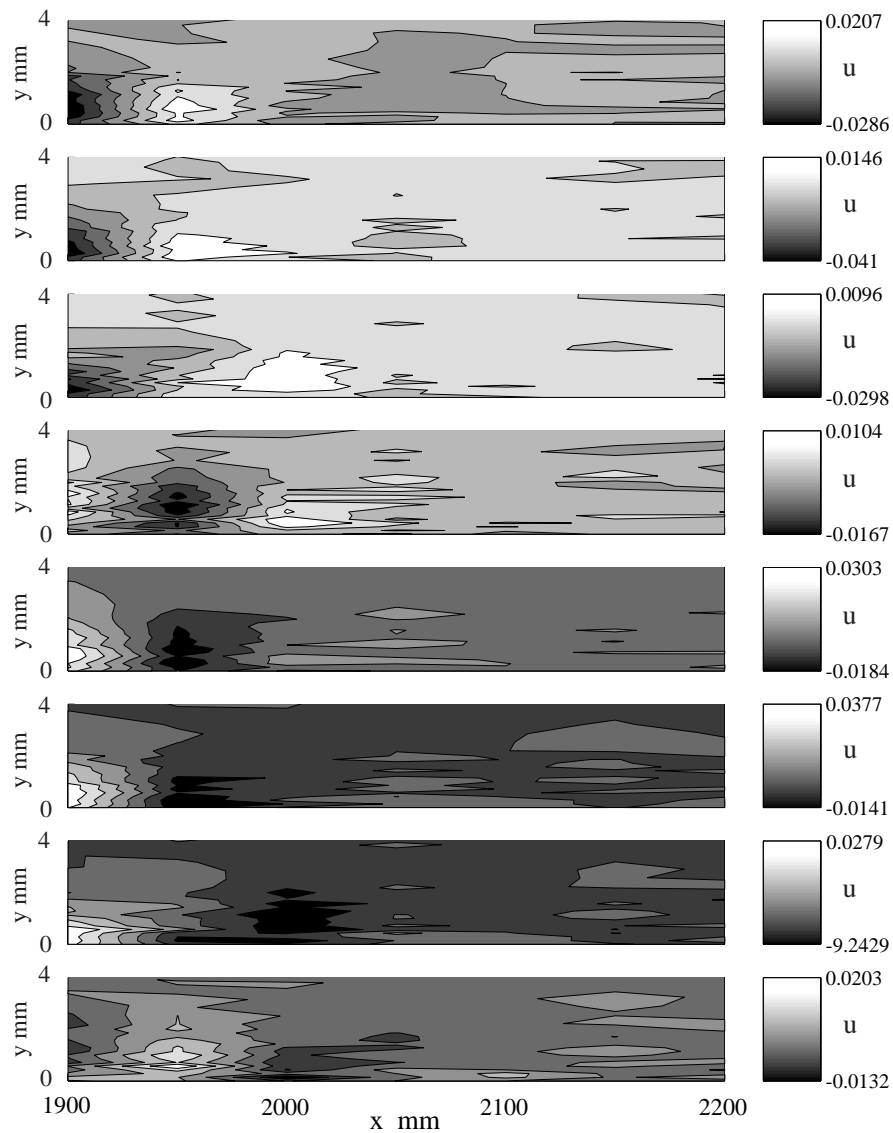


Figure 4.27: Contourplot of a TS-wave perturbation at  $F=59$  in an asymptotic suction boundary layer. The time between the figures is  $\Delta t=8$  ms.

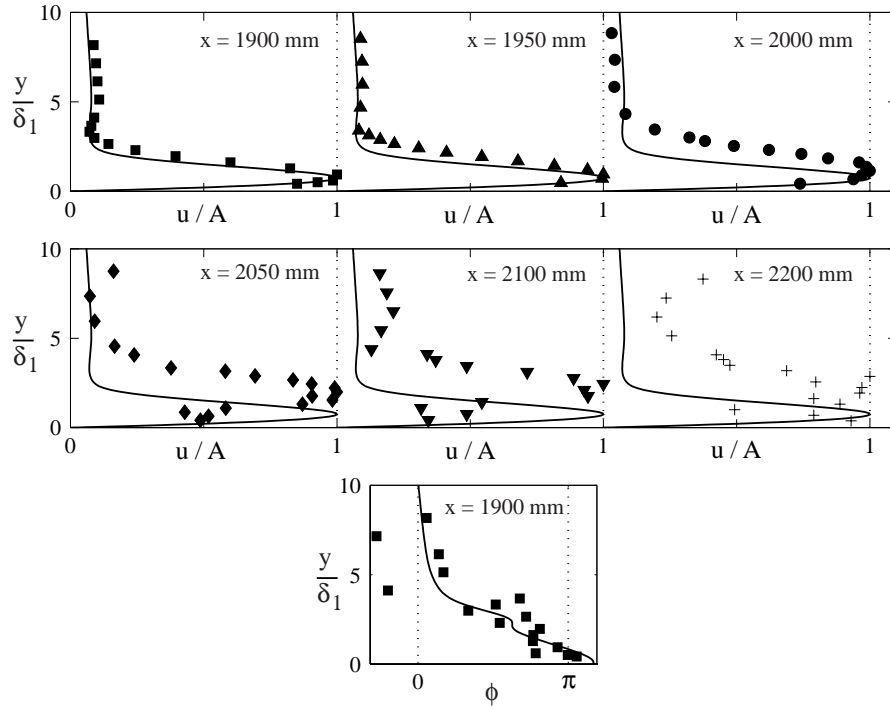


Figure 4.28: Amplitude distribution profiles at different downstream positions for  $F=84.4$  with the last figure showing the phase distribution profile close to the disturbance source.

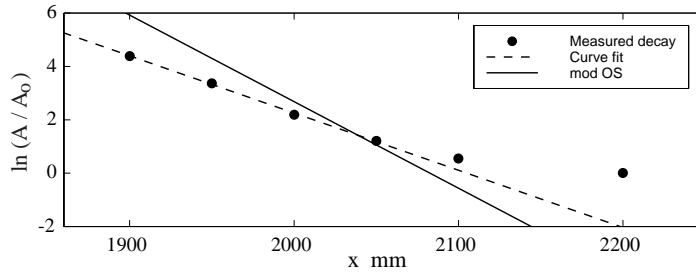


Figure 4.29: Amplitude decay versus the downstream distance for  $F=84.4$ .

first six points are used for the curve fit, and the modified OS-solution predicts  $\alpha_i = 0.0263 \text{ mm}^{-1}$ , i.e. a factor 1.72 higher.

In figure 4.27 contourplots of the TS-wave are shown with a time step of  $\Delta t=8$  ms between the figures. The generated disturbance is seen to have a fast decay before totally vanishing. Again the contrast in the contourplots is brought forth by applying a new colourbar for each figure resulting in a change of colour scale in each figure. This figure can be compared with figure 4.12, which is the corresponding TS-wave (same frequency) evolution in a Blasius boundary layer.

TS-wave results in an asymptotic suction boundary layer is also shown for a higher frequency, i.e.  $F=84.4$ . The same conclusions are drawn as for the lower frequency experiment. Good agreement with theory of the amplitude distribution profile close to the disturbance source and the theoretical decay factor is still overpredicted compared with the experimental results. See figures 4.28 and 4.29 for illustration. In figure 4.29 the four first points are used for the curve fit.

#### 4.2.3. Conclusions

As concluded earlier there are many external conditions that may have a larger impact on the stability characteristics of the flow when measuring far downstream from the leading edge as has been done here. There are some conditions that are known and will be brought up here, but whether these conditions are the underlying factors for linear stability theory not being able to predict the decay factor ( $\alpha_i$ ) correctly or not is hard to say.

First of all the adverse pressure gradient that is present in the asymptotic suction region (due to the suction), and was shown in figure 4.16, influences the stability characteristics of the flow to be more unstable. This would bring the theoretical results closer to the experimental ones. However, the pressure gradient is very small (less than 3% of pressure increase in the whole region) and according to Dr. A. Hanifi (private communication), PSE calculations with the present pressure gradient, show hardly any effect on the stability characteristics.

Secondly, the change of Reynolds number due to the change of displacement thickness in the region of interest may effect the stability characteristics. The reason for the displacement thickness decrease may be due to the impermeable streamwise length of 50 mm in connection with the disturbance slot discussed in section 3.4. A sudden stop of the continuous suction over some streamwise distance would allow the boundary layer to grow and that would imply a displacement thickness growth as noted in the measurements. This in turn makes the experimental profile more unstable, which is in agreement with the actual measured amplitude decay. However, this was taken into account in

the stability calculations by using a higher Reynolds number of  $Re=382$  that was extracted from the profiles in figure 4.21.

### 4.3. Free stream turbulence experiments

#### 4.3.1. Disturbance growth

Free stream turbulence gives rise to regions of high and low velocity (streaky structures) and in a Blasius boundary layer the streamwise disturbance energy grows in linear proportion to the downstream distance. These streaky structures move slowly in the spanwise direction and if the streamwise disturbance amplitude is measured ( $u_{rms}$ ) it is seen to increase with the downstream distance when no suction is applied, whereas in the suction case this amplitude increase was found to be eliminated and the  $u_{rms}$ -profiles more or less collapse on each other independent of the downstream position and the free stream turbulence intensity applied. This can be observed in figure 4.30 where the  $u_{rms}$ -profiles are plotted for both cases, i.e. with and without suction, for the  $Tu_B$ -level. The position above the plate, where the maximum  $u_{rms}$ -value appears, does hardly change in  $y/\delta_1$ -units and is approximately 1.5, this corresponds to 1/2- and 1/3 of the boundary layer thickness without suction and with suction, respectively. The results are similar for the other grids as well.

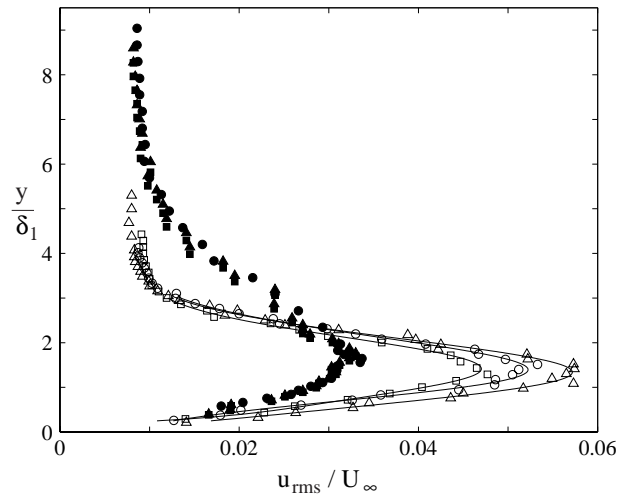


Figure 4.30:  $u_{rms}$ -profiles for different downstream positions from the leading edge with  $Tu_B$ . No suction (unfilled-) and suction (filled markers). ( $\square$ )  $x = 800$  mm; ( $\circ$ )  $x = 1000$  mm and ( $\triangle$ )  $x = 1200$  mm. Solid lines are curve fits to data.

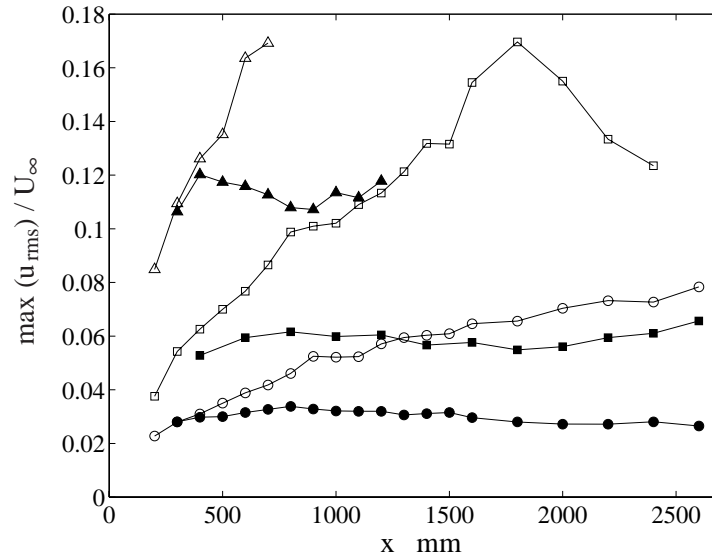


Figure 4.31: Disturbance amplitude vs downstream distance from the leading edge. No suction (unfilled-) and suction (filled markers). ( $\circ$ )  $Tu_B$ ; ( $\square$ )  $Tu_G$  and ( $\triangle$ )  $Tu_E$ .

In figure 4.31 the disturbance amplitude, for different free stream turbulence intensities, is plotted versus the downstream distance from the leading edge. For the no suction cases the disturbance amplitude has been found to grow in proportion to the  $x^{1/2}$  and a similar development is observed here. For grid B transition do not occur over the length of the measured region, despite the fact the the  $u_{rms}$ -level is above 6% at the end. For grid G a maximum of nearly 17% in the turbulence intensity is found at  $x \approx 1800$  mm. Such a maximum is usually observed in the intermittent region where the flow consists both of laminar regions and turbulent spots. Further downstream the intensity decreases which is expected when the flow goes towards a fully developed turbulent stage.

For grid E, measurements were only made until  $x = 700$  mm where a similar high level was observed. For all suction cases, however, it is found that transition do not occur even though the mean velocity as well as the disturbance profile are strongly effected (distorted) for the  $Tu_E$ -level case. Instead the fluctuation level inside the boundary layer reaches an almost constant level which is close to that existing where the suction starts. An interesting observation is that this level is proportional to the level of the free stream turbulence,

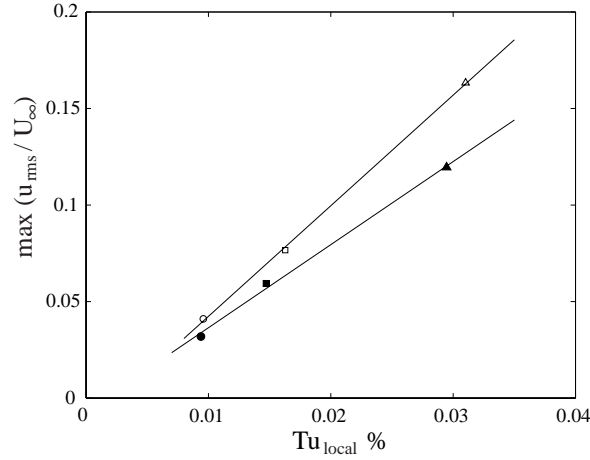


Figure 4.32: The maximum  $u_{rms}$ -value versus the local  $Tu$  at  $x=600$  mm. ( $\circ$ ) Grid B, ( $\square$ ) grid G, and ( $\triangle$ ) grid E. Filled markers with suction and unfilled without.

which is shown in figure 4.32 where the maximum  $u_{rms}$ -values (or saturation level in the suction case) versus the local  $Tu$ -level are plotted for both the suction and no suction case.

In figure 4.34 the velocity traces from different downstream positions and heights above the plate are shown for both the suction and no suction case and for all grids. Simply by looking at the velocity traces one can observe the disturbance growth in the Blasius boundary layer and the disturbance saturation in the asymptotic suction boundary layer, see figures a), c) and e). Figures b), d) and f) show the traces through the boundary layer and the (\*)-markers indicates where the maximum  $u_{rms}$ -value appear in the boundary layer. The displacement thickness that has been used for normalization is the local one calculated from the mean velocity profile. In the case with suction this was done by the curve fit method used in the previous sections. These values are found in the figure caption and in figure 4.33 the displacement thickness evolution is plotted versus the downstream distance. In a Blasius transition region when the profile approaches the turbulent one an increase in the displacement thickness is expected. According to this figure the displacement thickness seems to increase somewhat in both the suction and no suction case when the  $Tu$ -level is increased.

In figures 4.35 to 4.40 both the mean velocity and disturbance profiles are plotted for different downstream positions and for all three grids.

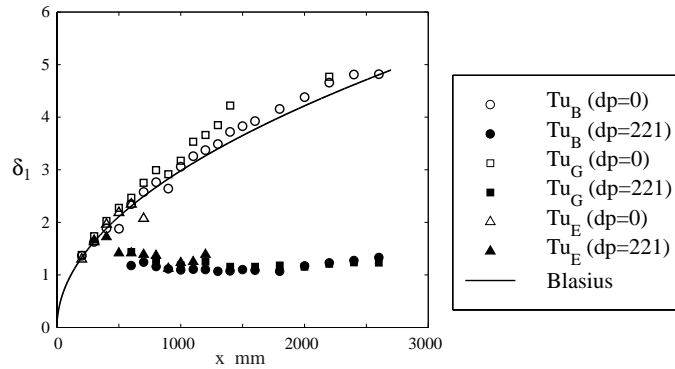


Figure 4.33: The displacement thickness evolution with and without suction when influenced by free stream turbulence.

In figure 4.35 the result from grid B for the no suction case is shown. In a) the mean velocity profile hardly show any distortion from the theoretical Blasius profile despite disturbance levels up to 8% inside the boundary layer far downstream. Each solid curve in b) is a curve fit to data in order to more easily separate the different downstream positions from each other. When suction is applied, see figure 4.36 the asymptotic suction profile is very quickly achieved which is seen in a). The agreement with the theoretical curve is excellent which is somehow expected since for this  $Tu$ -level not even the no suction mean profiles seem to be effected by the free stream turbulence. However, an interesting feature of the asymptotic suction boundary layer, as mentioned earlier, is the appearance of the disturbance saturation level. This can be observed in figure b) where the disturbance amplitude inside the boundary layer is only slightly decreased when going downstream. Note that the decay is not much stronger than the free stream turbulence decay observed in the upper part of this figure.

For high enough  $Tu$ -levels the free stream turbulence will force the flow to transition at a subcritical Reynolds number. When changing the turbulence generating grid to grid G the mean velocity profile becomes turbulent far downstream and is shown in figure 4.37a). In b) the disturbance amplitude is again seen to grow until transition is reached. However, the asymptotic suction mean profiles show no deviation from the theoretical curve for this  $Tu$ -level and the disturbance amplitude has again reached a saturation level, see figure 4.38a) and b).

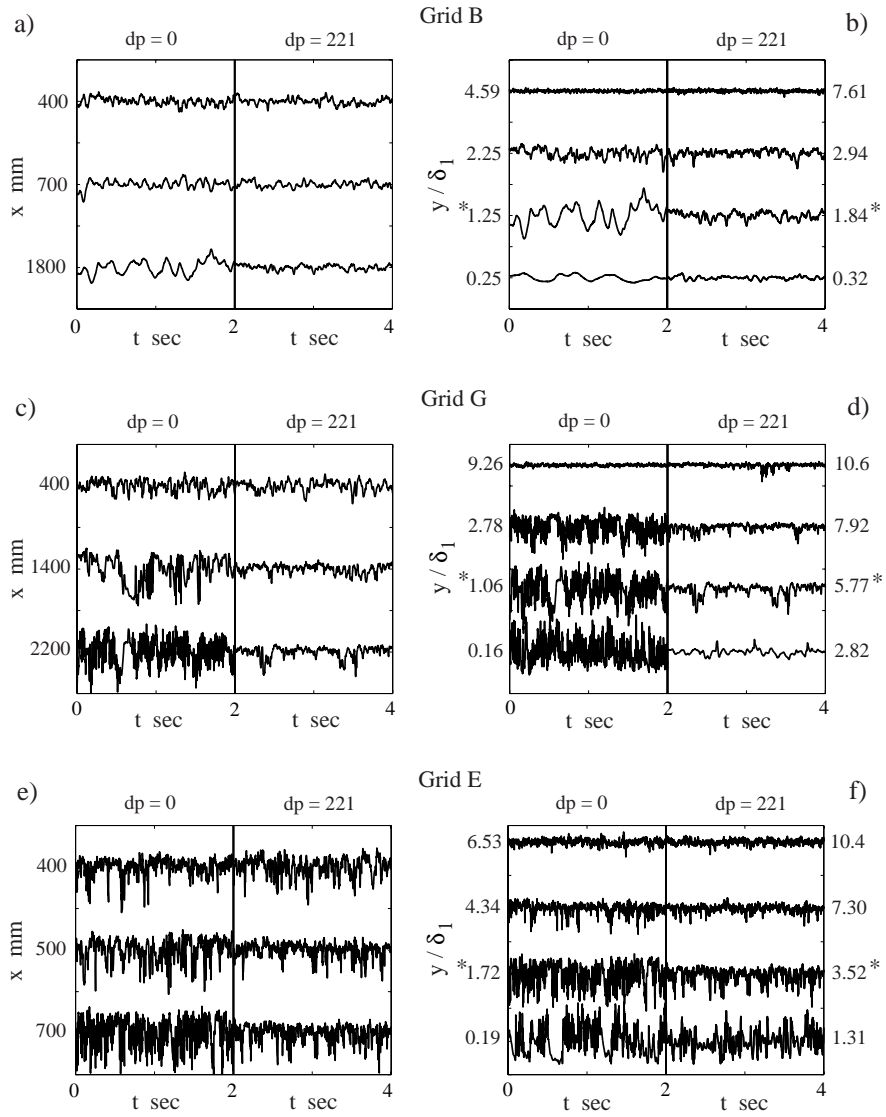


Figure 4.34: Velocity traces (2 sec long) for all grids with and without suction for different  $x$ -positions and heights above the plate. a), c) and e) show traces from where the maximum  $u_{rms}$  appears. b), d) and f) show traces at  $x=1800$  (with  $\delta_1 = 4.16$  mm and  $\delta_1^s = 1.07$  mm), 2200 (with  $\delta_1 = 4.75$  mm and  $\delta_1^s = 1.18$  mm), and 700 mm (with  $\delta_1 = 2.29$  mm and  $\delta_1^s = 1.39$  mm), respectively, for different heights above the plate where the (\*)-markers indicate where the maximum  $u_{rms}$ -value appears across the boundary layer. The superscript (s) stands for suction.

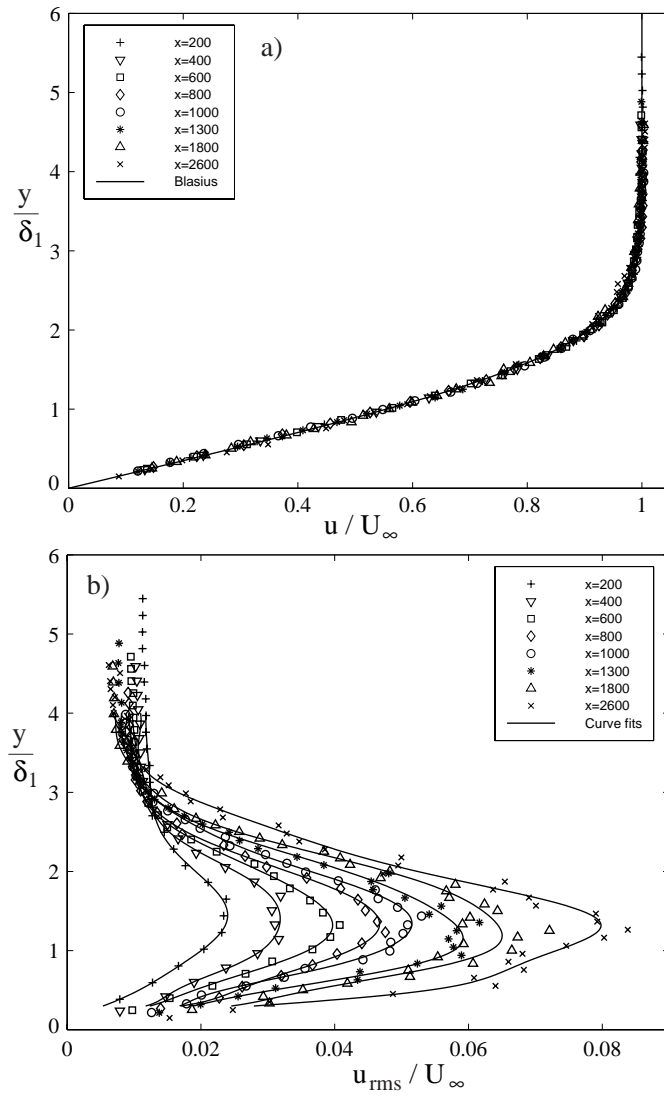


Figure 4.35: Data for different downstream positions from grid B without suction. a) Mean velocity profiles, and b)  $u_{rms}$ -profiles for the same  $x$ -positions as in a).

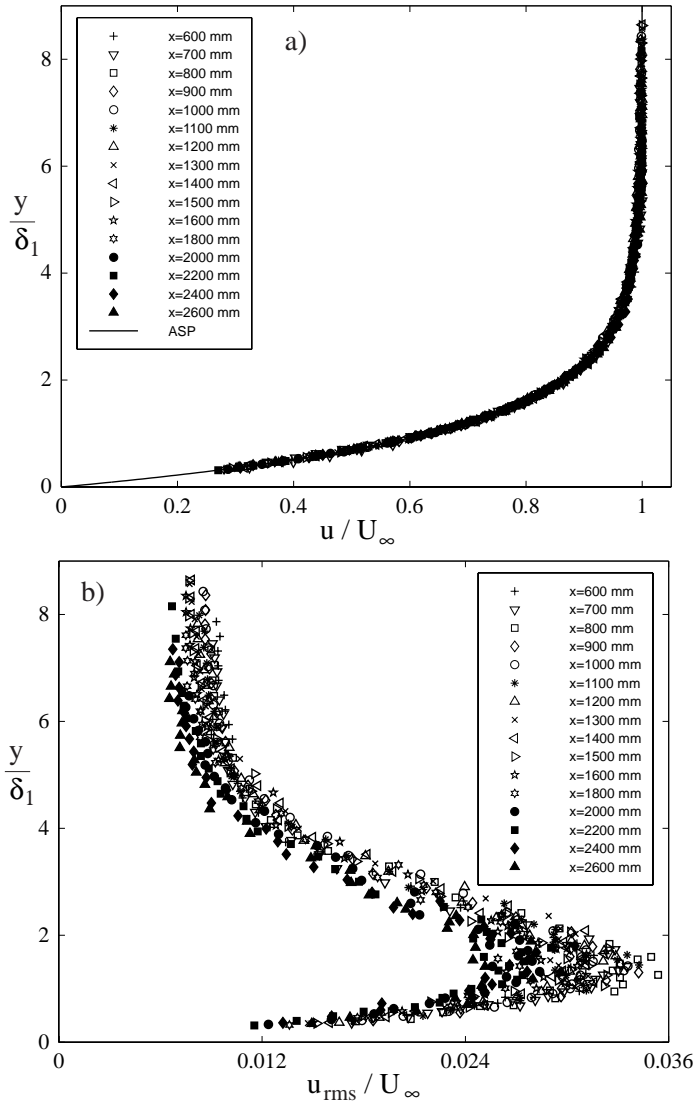


Figure 4.36: Data for different downstream positions from grid B with suction. a) Mean velocity profiles, and b)  $u_{rms}$ -profiles for the same  $x$ -positions as in a).

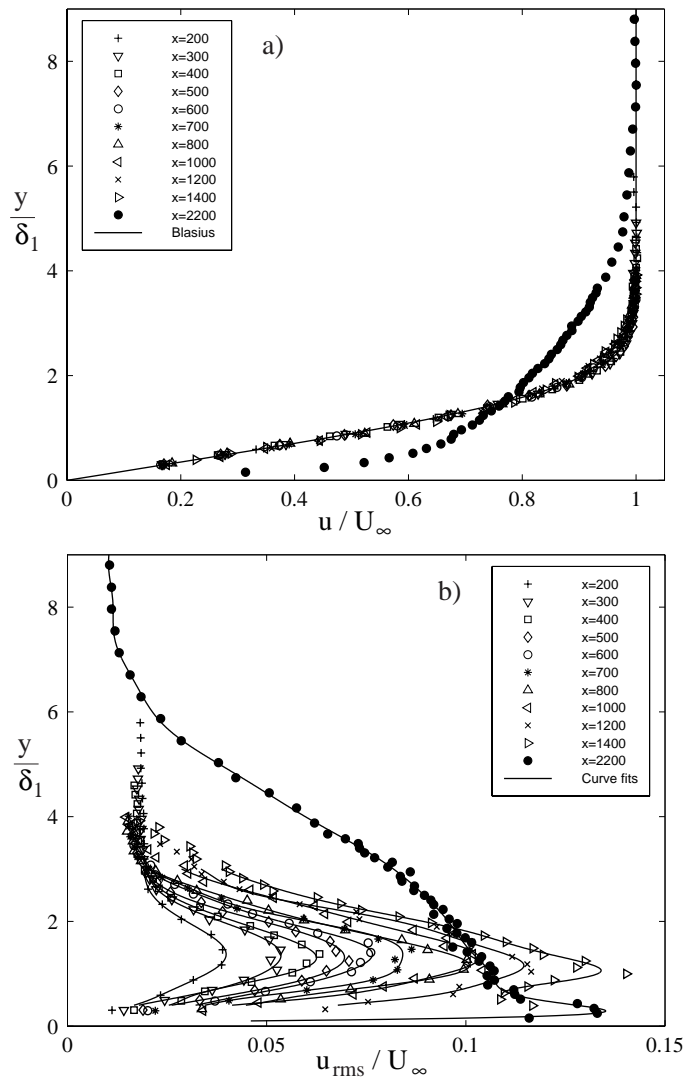


Figure 4.37: Data for different downstream positions from grid G without suction. a) Mean velocity profiles, and b)  $u_{rms}$ -profiles for the same  $x$ -positions as in a).

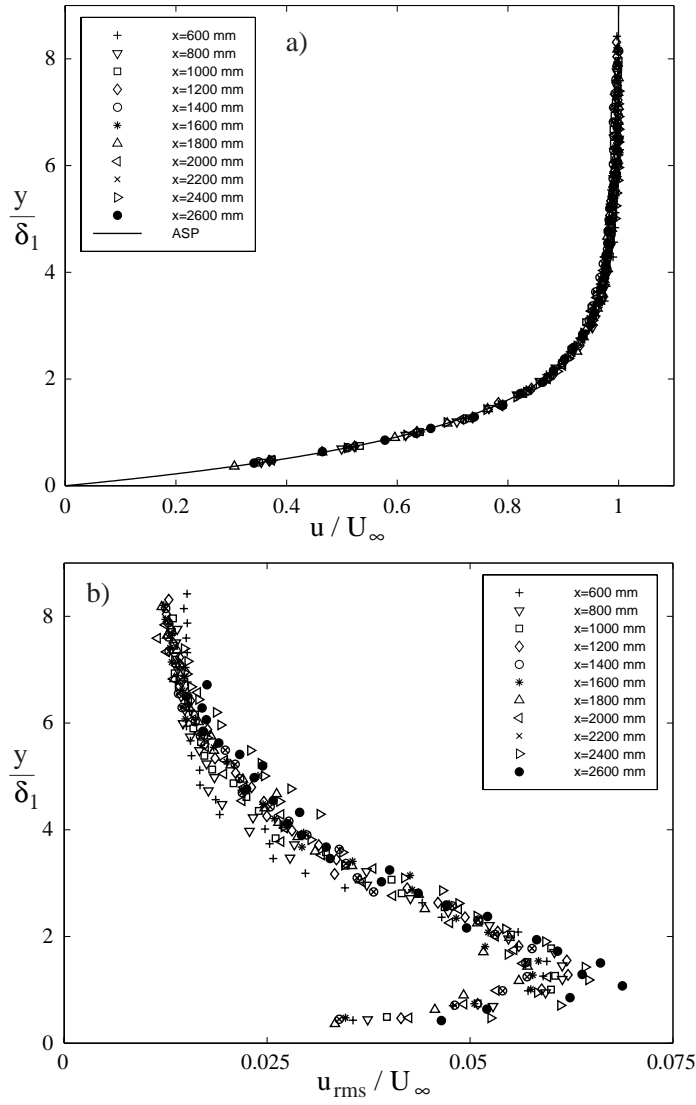


Figure 4.38: Data for different downstream positions from grid G with suction. a) Mean velocity profiles, and b)  $u_{rms}$ -profiles for the same  $x$ -positions as in a).

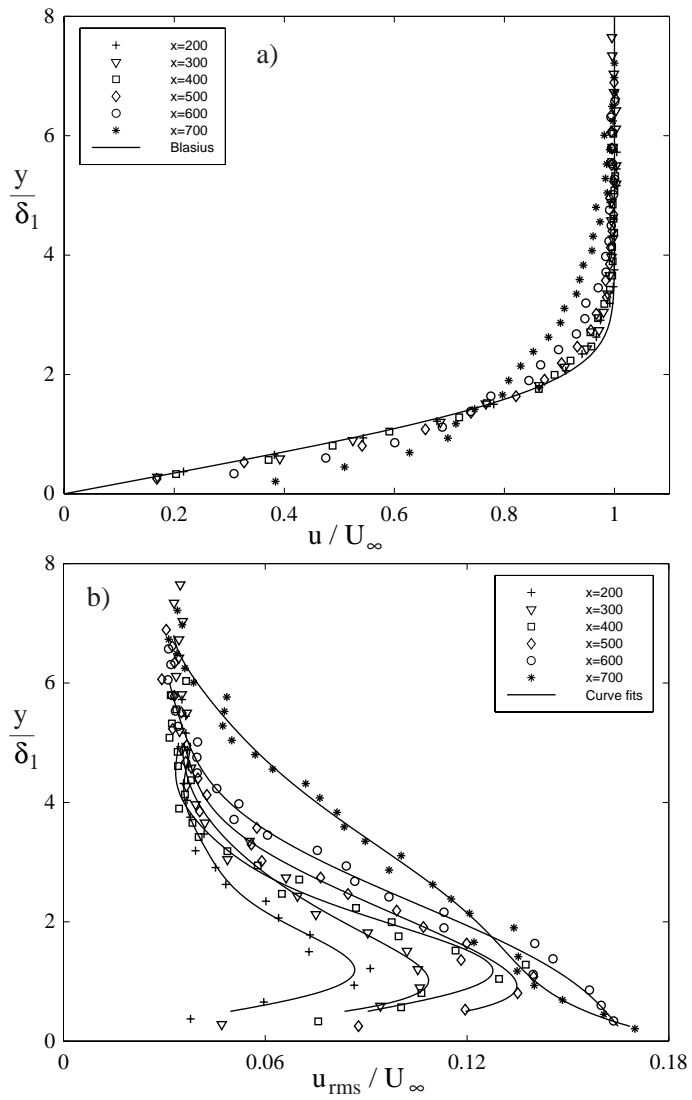


Figure 4.39: Data for different downstream positions from grid E without suction. a) Mean velocity profiles, and b)  $u_{rms}$ -profiles for the same  $x$ -positions as in a).

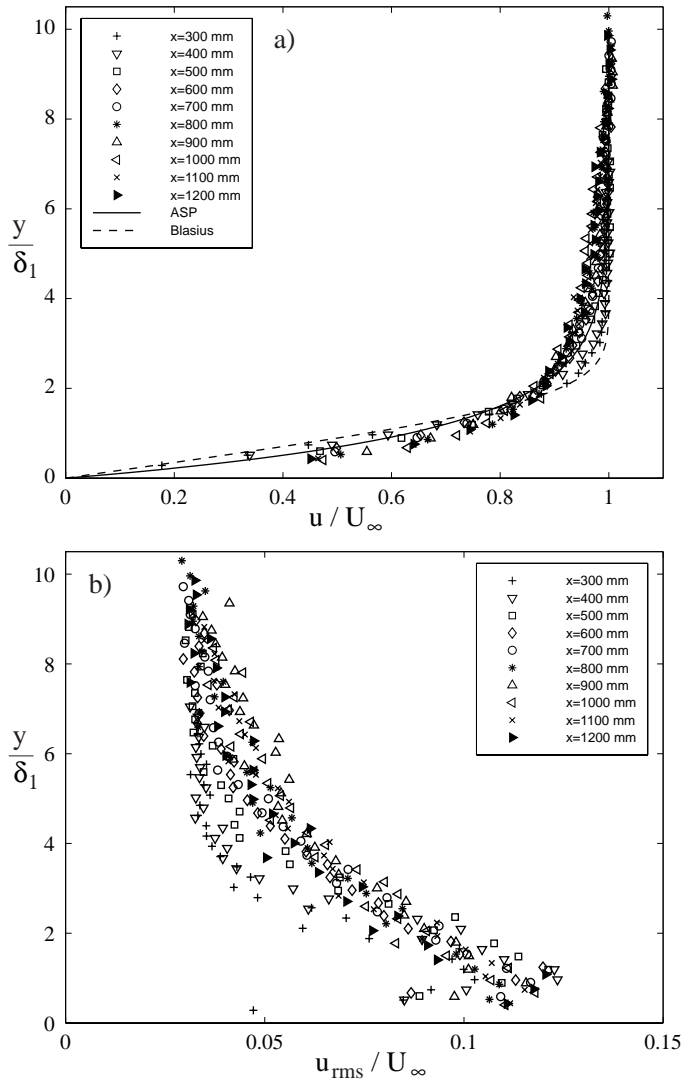


Figure 4.40: Data for different downstream positions from grid E with suction. a) Mean velocity profiles, and b)  $u_{rms}$ -profiles for the same  $x$ -positions as in a).

For grid E the laminar flow can not be sustained for very long. In figure 4.39 this can be observed from the velocity profiles. At an early stage the mean profile is effected of the high  $Tu$ -level and the disturbance amplitude is approximately 10% as early as 300 mm from the leading edge. When suction is applied the asymptotic suction boundary layer is never reached since the suction starts at  $x = 360$  mm and the  $Tu$ -level is very high. Despite the high disturbance amplitude inside the boundary layer at this  $x$ -position the suction is capable of maintaining this disturbance level throughout the measured region, which can be observed in figure 4.40.

In figure 4.41 the total kinetic energy ( $E_{tot}^K$ ) inside the boundary layer is plotted versus the downstream distance from the leading edge. This energy was calculated according to

$$E_{tot}^K = \frac{1}{\delta} \int_0^\delta \int_0^\infty f E d(\log(f)) dy,$$

where  $\delta$  is the boundary layer thickness. For the no suction case this  $\delta$  was consistently taken to be  $5\sqrt{(x\nu/U_\infty)}$ , i.e. the Blasius boundary layer thickness,

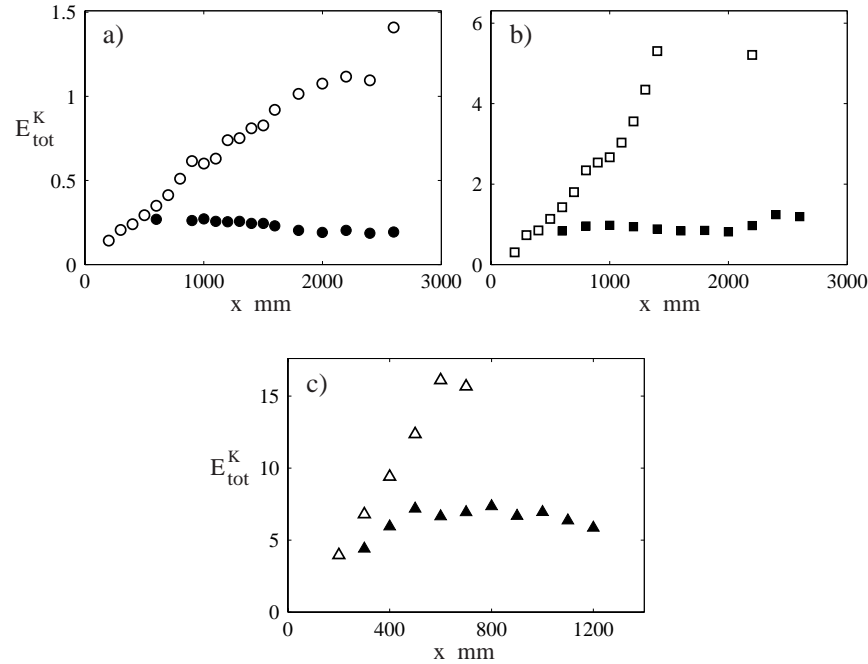


Figure 4.41: The growth of the total kinetic energy inside the boundary layer. a) Grid B, b) grid G, and c) grid E.

and for the suction case expression (2.46) was used with the local  $\delta_1$ . The figures show the well known linear growth of the disturbance energy with the downstream distance for the no suction case and for all  $Tu$ -levels. In the case with suction the energy saturation level is seen.

#### 4.3.2. Spanwise scale of the streaks

The spanwise scale of the streaks can be determined through two-point correlation measurements of the streamwise velocity component. It is well known that the position where the streamwise correlation coefficient ( $R_{uu}$ ) shows a distinct minimum can be interpreted as half the dominating spanwise wavelength of the streaks (see e.g. Matsubara & Alfredsson (2001)). In order to determine this spanwise scale the correlation measurement has preferably to be done inside the boundary layer where the maximum  $u_{rms}$  appears, this is the position where the correlation coefficient will appear strongest. The spanwise correlation coefficient is defined as

$$R_{uu} = \frac{\overline{u(z)u(z + \Delta z)}}{\overline{u(z)^2}}.$$

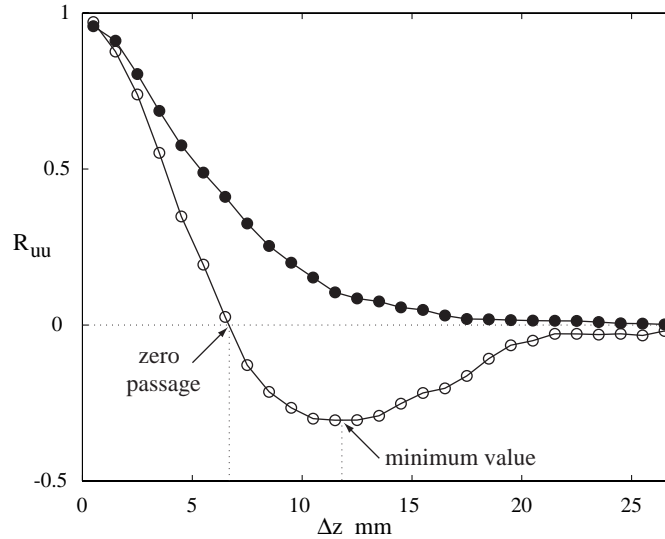


Figure 4.42: The spatial (spanwise) correlation coefficient ( $R_{uu}$ ) versus the separated distance ( $\Delta z$ ). ( $\bullet$ ) Measured at the boundary layer edge, and ( $\circ$ ) measured at the position inside the boundary layer where the maximum  $u_{rms}$  appears. The two curves are obtained from smoothend data from a  $yz$ -plane measurement at  $x = 1800$  mm with  $Tu_B$ .

In figure 4.42 two correlation measurements are shown, one measured at the boundary layer edge ( $\bullet$ ) and the other where the maximum  $u_{rms}$  appears ( $\circ$ ). In the former the correlation is close to one at the first measuring point and it decays gradually to become uncorrelated far away. In the latter measurement the correlation coefficient shows the (previously mentioned) distinct minimum. An interesting observation is the zero passage of the correlation coefficient that will be shown to be an equally good measure of the spanwise scale of the streaks as the minimum value. In figure 4.43 the correlation coefficient is plotted for gradually increasing distance ( $y$ ) above the plate. Close to the surface the data seem to be somewhat scattered, which is due to the low velocity and undeveloped streaks in connection with too short sampling time (30 sec) for these  $y$ -positions. From such figure as 4.43 one can make a contourplot in the  $yz$ -plane for an overview of the structure inside the boundary layer. This was done for different  $Tu$ -levels and  $x$ -positions with and without suction and are shown in figure 4.44 (for  $Tu_B$  and  $Tu_G$ ) and 4.45 (for  $Tu_E$  with suction). Figure 4.44 show that the spanwise scale of the streaky structures is only slightly decreased by suction, despite a twofold reduction in boundary layer thickness, indicating the importance of the scale of the free stream turbulence. Note that the minimum value is clearly distinguishable in all cases, including in figure 4.45 with  $Tu_E$  at  $x = 500$  mm.

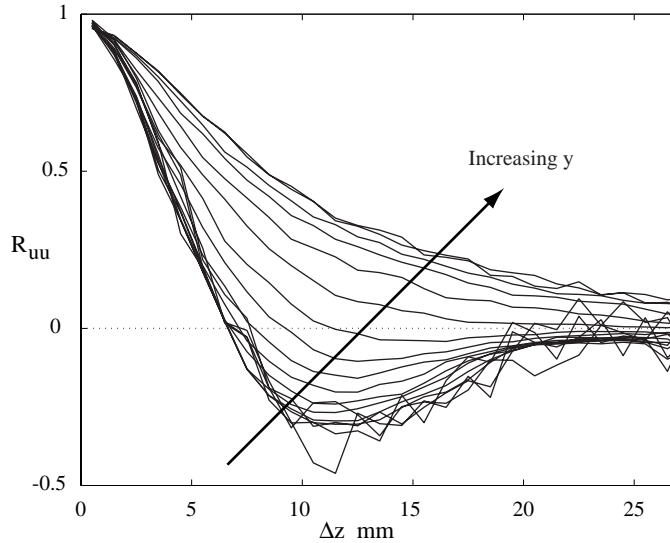


Figure 4.43: The spatial (spanwise) correlation coefficient ( $R_{uu}$ ) versus the separated distance ( $\Delta z$ ) for different distances above the plate at  $x = 1800$  mm with  $Tu_B$ .

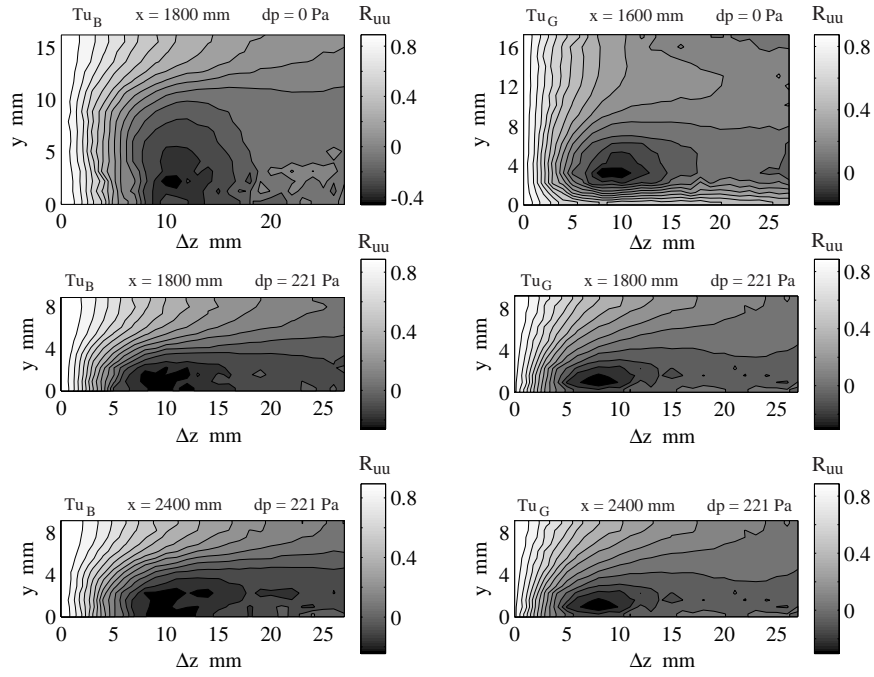


Figure 4.44: Contourplots of  $R_{uu}$  in the  $yz$ -plane for different downstream positions for both  $Tu_B$  and  $Tu_G$ .

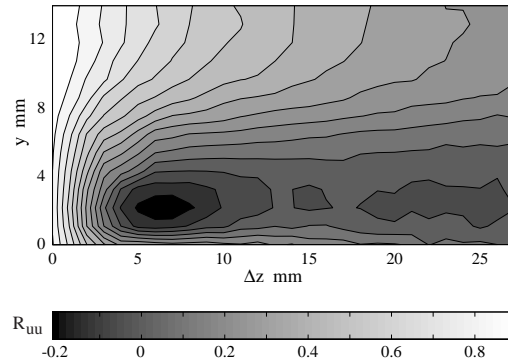


Figure 4.45: Contourplot of  $R_{uu}$  in the  $yz$ -plane at  $x = 500$  mm with  $Tu_E$ .

Matsubara & Alfredsson (2001) showed that the spanwise scale of the streaks observed near the leading edge seems to depend on the free stream turbulence scales introduced into the boundary layer at an early stage of the receptivity process. Further downstream this scale seems to adapt to the boundary layer thickness and grows in proportion to this thickness. In the suction case the scenario is slightly different since the spanwise scale is hardly changed compared to the spanwise scale observed in the Blasius boundary layer, and this despite the fact that the boundary layer thickness is only half of that in a Blasius layer. This result was obtained for all three free stream turbulence intensities tested. The conclusion from figure 4.44 is that the effect of suction on the streaks is compression, i.e. the boundary layer is compressed in the wall-normal direction reducing the boundary layer thickness but preserving the spanwise scale creating an wider structure in terms of boundary layer thickness as compared to the Blasius case. This indicates the importance of the scale of

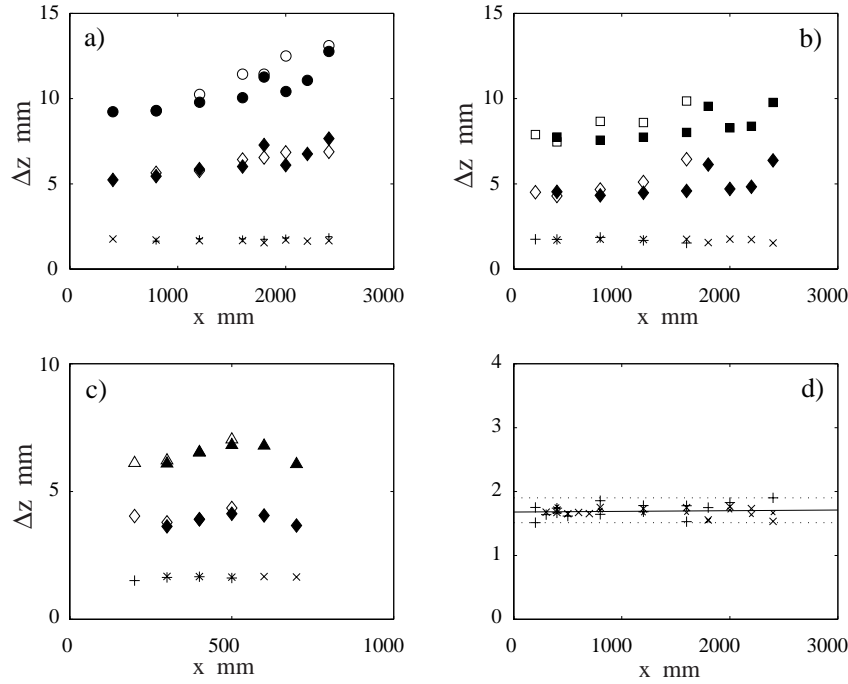


Figure 4.46: Evolution of the spanwise scale of the streaks. No suction (unfilled) and suction (filled markers). a)  $(\circ)$   $\min(R_{uu})$  and  $(\diamond)$   $\text{zero}(R_{uu})$  for  $Tu_B$ . b)  $(\square)$   $\min(R_{uu})$  and  $(\diamond)$   $\text{zero}(R_{uu})$  for  $Tu_G$ . c)  $(\triangle)$   $\min(R_{uu})$  and  $(\diamond)$   $\text{zero}(R_{uu})$  for  $Tu_E$ . d)  $\min(R_{uu})/\text{zero}(R_{uu})$  for all grids. (+) no suction and (x) suction.

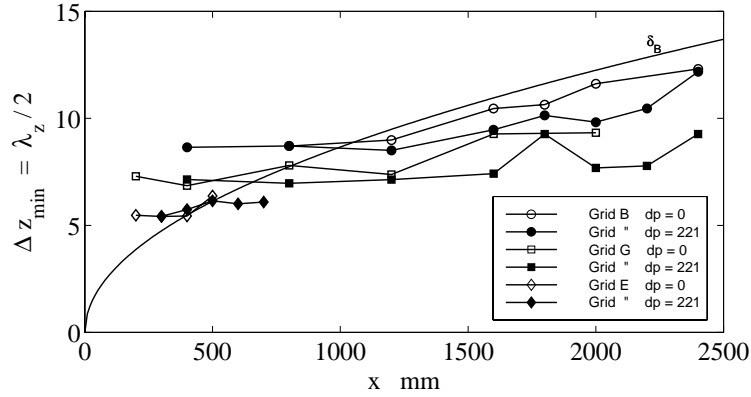


Figure 4.47: Evolution of the spanwise scale of the streaks for all cases are plotted together with the Blasius boundary layer thickness evolution. Same data as in figure 4.46.

the free stream turbulence, on the disturbance structure inside the boundary layer.

In figure 4.46 the evolution of the spanwise scales of the streaks from all three grids are shown. The minimum values of the correlation coefficient ( $R_{uu}$ ) were determined by fitting a third order polynomial to the measured data and the zero passage of  $R_{uu}$  by fitting a second order polynomial. In figure 4.46a) we see the largest increase of the spanwise scale compared to the other free stream turbulence intensities in b) and c). If a discrepancy between the no suction- and suction case should be pointed out a tendency towards slower growing spanwise scale in the suction case compared to the no suction case may be observed. The spanwise scale of the streaks seems to decrease with increasing free stream turbulence intensities according to figure 4.46. As can be seen in figure 4.46d) the zero passage is an equally good measure of the spanwise scale as the minimum value of the correlation coefficient. The zero passage may be hard to interpret physically but is easier to determine from an experimentalist's point of view. All ratios of the minimum value of the correlation coefficient and the zero passage of the present data collapse at a value of  $1.68 \pm 0.23$ .

In figure 4.47 the evolution of the spanwise scales of the streaks are plotted again (same data as in figure 4.46) together with the Blasius boundary layer thickness evolution. This figure allows a direct comparison between all cases and confirm previous studies, see e.g. Matsubara & Alfredsson (2001), that the spanwise scale seems to adapt to the boundary layer thickness for low  $Tu$ -levels without suction.

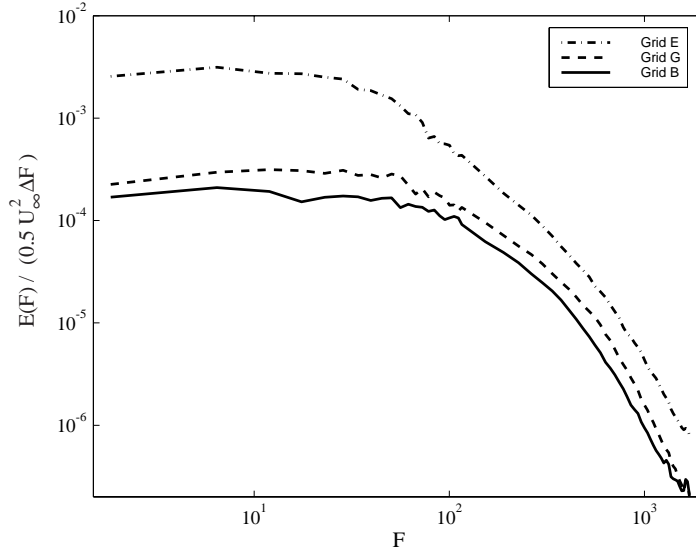


Figure 4.48: Energy spectra from the three different grids at  $x=400$  mm.

In figure 4.48 the energy spectra are plotted for the three different grids. From this figure one can observe that the energy distribution is higher for all frequencies with increasing  $Tu$ -level. According to the observations done here it seems that the wider the energy spectra that is introduced into the boundary layer is, the smaller is the preferred spanwise scale.

#### 4.3.3. The wall-normal velocity fluctuation

So far only the streamwise velocity fluctuation component has been considered and it has been shown to be strongly damped when suction is applied compared with the no suction case. In figure 4.49 both HW-data (X-probe) a) and LDV-data b) of the wall-normal velocity fluctuation are shown. The wall-normal distance has been chosen to be dimensional for direct comparison between the no suction and suction case. The peculiar peak observed in the HW-data inside the boundary layer is a measurement error due to unsteady velocity gradients when using X-probes (see paper 2 of the present thesis). The difference in  $v_{rms}$  measured by the X-probe is a direct consequence of a much smaller amplitude of the streaks in the suction case. According to figure 4.49 it seems that the  $v_{rms}$ -profile does not change when suction is applied even though the mean normal velocity is highly increased. The LDV-data in figure b) shows the early decay of the wall-normal fluctuation component (note that the boundary layer

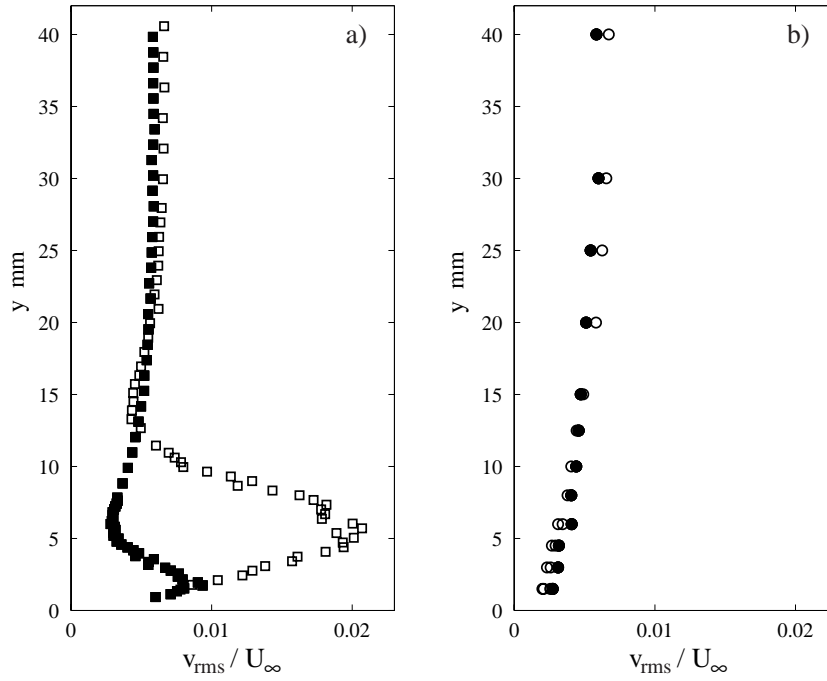


Figure 4.49: X-probe versus LDV measurements in boundary layers influenced by free stream turbulence. a) HW-measurements, ( $\square$ ) no suction and ( $\blacksquare$ ) with suction. b) LDV-measurements, ( $\circ$ ) no suction and ( $\bullet$ ) with suction. Measurements with no suction applied are performed at  $x = 1800$  mm and when suction applied at  $x = 2400$  mm.

thicknesses are approximately 11.6 and 5 mm in the no suction and suction case, respectively) all the way to the surface where it finally becomes zero.

## CHAPTER 5

### Summary

In the present work a successful experimental set-up to establish the asymptotic suction boundary layer in a wind tunnel is reported. A new test plate with a porous surface material has been constructed and a leading edge with a short region of non-zero pressure gradient has been designed. The mean flow development from the leading edge of the plate is shown to be in good agreement with a theoretical boundary layer analysis and when the asymptotic suction region is reached there is an excellent agreement between the theoretical and experimental boundary layer profiles.

The main interest of the study is to investigate the effect due to suction on disturbance development inside the boundary layer. The stability equations for modal disturbances are derived where the wall normal mean velocity modifies the standard Orr-Sommerfeld equation. The effect of this component as well as the change in mean velocity profile is discussed, and it is shown that the main effect is due to the profile change. A model problem with flow in a channel with porous walls with suction and blowing, respectively, is also studied.

TS-waves are generated in the experiment through a spanwise slot and the development of the waves over the plate without suction is shown to be in good agreement with standard stability theory and previous experiments. The same conclusion can be drawn for the asymptotic suction boundary layer although in that case the waves are strongly damped. The correspondence of the streamwise amplitude profiles and the phase velocity is good, but the decay factor predicted by linear stability theory is slightly overestimated compared to the experimental results.

A comprehensive study of the disturbance development of free stream turbulence induced disturbances was also made. Direct comparisons between the no suction (Blasius) and suction cases were made. In the no suction case the results were similar to earlier work, showing a linear growth of the disturbance energy in the downstream direction until spot formation occurs. However in the suction case the disturbance amplitude have been shown to reach a saturation level, which is proportional to free stream turbulence level. We also find that transition is inhibited for all cases with suction. The spanwise scale of the streaks is maintained when suction is applied compared with the no suction case, and this despite a twofold boundary layer thickness reduction. The

saturation of the disturbance amplitude in the boundary layer indicates that the growth is inhibited and maybe that the dynamics of the streaks become different in the suction case. Further theoretical studies of non-modal growth of streaky structures in the asymptotic boundary layer may give further information on the interpretation of the present results.

## APPENDIX A

### Inaccurate determination of the shape factor

In most experimental work the authors are willing to share their estimates of the wall (plate) positions relatively their probe and usually to give an absolute error from the estimation. What they forget is that this error effects the calculation of the characteristic length scales to a larger extent than expected. If the wall position is given with some error the displacement thickness is not more accurate than this error as a first approximation. This effects the shape factor which often is used as a measure of how Blasius like the actual boundary layer is and it is not rare to find the exact value of 2.59. Another quantity that can cause problem is the free stream velocity which of course also effects the values of the characteristic length scales.

Therefore the following analysis can be useful in order to give a feeling about how sensitive the calculation of the shape factor really is.

#### A.1. Effect of inaccurate determination of the wall position

Starting from the definition of the displacement thickness

$$\delta_1 = \int_{y_w}^{\infty} \left(1 - \frac{u^*(y)}{U_\infty}\right) dy,$$

where  $y_w$  is the position of the wall, we assign  $y_w$  a small positive value ( $\hat{\varepsilon}$ ) above the plate which then results in the following calculated displacement thickness due to the inaccuracy of the wall position ( $\delta_1^{cw}$ )

$$\begin{aligned} \delta_1^{cw} &= \int_{\hat{\varepsilon}}^{\infty} \left(1 - \frac{u^*(y)}{U_\infty}\right) dy = \int_0^{\infty} \left(1 - \frac{u^*(y)}{U_\infty}\right) dy - \int_0^{\hat{\varepsilon}} \left(1 - \frac{u^*(y)}{U_\infty}\right) dy \\ &= \delta_1^{real} - \int_0^{\hat{\varepsilon}} \left(1 - \frac{u^*(y)}{U_\infty}\right) dy. \end{aligned}$$

Here the *real*-value denotes the exact theoretical value. The second integral ( $I_2$ ) can be estimated by assuming that the velocity is proportional to the wall-normal distance close to the wall according to  $u^*(y) = \frac{u^*(\hat{\varepsilon})}{\hat{\varepsilon}}y$  which gives

$$I_2 = \left[ y - \frac{u^*(\hat{\varepsilon})}{\hat{\varepsilon}U_\infty} \frac{y^2}{2} \right]_0^{\hat{\varepsilon}} = \left( \hat{\varepsilon} - \frac{u^*(\hat{\varepsilon})}{2U_\infty} \hat{\varepsilon} \right)$$

and finally

$$\delta_1^{cw} = \delta_1^{real} + \left( \frac{u^*(\hat{\varepsilon})}{2U_\infty} - 1 \right) \hat{\varepsilon}. \quad (\text{A.1})$$

The same approach can be made with the calculated momentum loss thickness ( $\delta_2^{cw}$ ), which results in

$$\delta_2^{cw} = \delta_2^{real} + \frac{u^*(\hat{\varepsilon})}{2U_\infty} \left( \frac{u^*(\hat{\varepsilon})}{2U_\infty} - \frac{1}{2} \right) \hat{\varepsilon}. \quad (\text{A.2})$$

Now, it is not a strict assumption to say that  $\frac{u^*(\hat{\varepsilon})}{U_\infty} \sim 1\%$  implying that  $u^*(\hat{\varepsilon}) \ll U_\infty$  which applied on equations (A.3) and (A.2) gives

$$\begin{aligned} \delta_1^{cw} &\approx \delta_1^{real} - \hat{\varepsilon} \\ \delta_2^{cw} &\approx \delta_2^{real} \end{aligned}$$

and correspondingly the calculated shape factor ( $H_{12}^{calc}$ ) as

$$H_{12}^{cw} = \frac{\delta_1^{real} - \hat{\varepsilon}}{\delta_2^{real}} = H_{12}^{real} - 7.5 \frac{\hat{\varepsilon}}{\delta} \quad (\text{A.3})$$

when Blasius like profile is assumed. A correct presentation of the shape factor for a Blasius profile at  $U_\infty = 5$  m/s,  $x = 150$  mm and  $y_w = \pm \hat{\varepsilon} = \pm 0.02$  mm should therefore read  $H_{12} = 2.59 \pm 0.05$ .

## A.2. Effect of inaccurate determination of the free stream velocity

A similar analysis can be made by assuming a small error ( $\hat{\varepsilon}$ ) in determining the free stream velocity. By substituting the free stream velocity with the true ( $T$ ) velocity  $U_\infty^T = (1 + \hat{\varepsilon})U_\infty$  and by assuming  $\hat{\varepsilon} \ll 1$  and a Blasius like profile we get the following expression of the calculated displacement thickness due to inaccurate free stream velocity ( $\delta_1^{cf}$ )

$$\begin{aligned}
\delta_1^{cf} &= \int_0^\delta \left( 1 - \frac{u^*(y)}{(1+\tilde{\varepsilon})U_\infty} \right) dy \approx \int_0^\delta \left( 1 - (1-\tilde{\varepsilon})\frac{u^*(y)}{U_\infty} \right) dy \\
&= \delta_1^{real} + \tilde{\varepsilon} \int_0^\delta \frac{u^*(y)}{U_\infty} dy = \delta_1^{real} + \tilde{\varepsilon} \int_0^\delta \left( \frac{u^*(y)}{U_\infty} - 1 + 1 \right) dy \\
&= \delta_1^{real} - \tilde{\varepsilon}\delta_1^{real} + \tilde{\varepsilon}\delta = \delta_1^{real}(1 + 1.9\tilde{\varepsilon}). \tag{A.4}
\end{aligned}$$

For the momentum loss thickness with the same assumptions and after neglecting all second order  $\tilde{\varepsilon}$  terms we get

$$\begin{aligned}
\delta_2^{cf} &= \int_0^\delta \frac{u^*(y)}{(1+\tilde{\varepsilon})U_\infty} \left( 1 - \frac{u^*(y)}{(1+\tilde{\varepsilon})U_\infty} \right) dy = \dots \\
&= \delta_2^{real}(1 - 2\tilde{\varepsilon}) + \tilde{\varepsilon}\delta - \tilde{\varepsilon}\delta_1^{real} \approx \delta_2^{real}(1 - 2.91\tilde{\varepsilon}). \tag{A.5}
\end{aligned}$$

The corresponding shape factor ( $H_{12}^{cf}$ ) based on equations (A.4) and (A.5) then read

$$\begin{aligned}
H_{12}^{cf} &= \frac{\delta_1^{real}(1 + 1.9\tilde{\varepsilon})}{\delta_2^{real}(1 - 2.91\tilde{\varepsilon})} \approx H_{12}^{real}(1 + 1.9\tilde{\varepsilon})(1 + 2.91\tilde{\varepsilon}) \\
&\approx H_{12}^{real}(1 + 4.8\tilde{\varepsilon}), \tag{A.6}
\end{aligned}$$

which for 0.5% error of the free stream velocity, i.e.  $\tilde{\varepsilon} = 0.005$ , will result in an absolute error of  $\pm 0.03$  of the shape factor.

## APPENDIX B

### Active turbulence generating grid

Free stream turbulence (FST) is usually generated with the use of grids, consisting of circular or square bars. The scale and intensity of the FST is related to the geometry of the grid, as for instance the mesh width ( $M$ ) and the solidity, where a higher solidity gives a higher turbulence level. In order to generate different FST intensities without changing the set-up in the test section an active grid was developed. The grid is active in the sense that it ejects secondary fluid jets into the fluid upstream, i.e. counterflow injection. A thorough study on such an active grid was carried out by Gad-El-Hak & Corrsin (1974) where both coflow and counterflow injection was compared with the zero injection case. They show through a simple analysis that in the zero injection case the FST intensity is proportional to the square root of the coefficient of static pressure drop over the grid. Even though an expression of this coefficient may be derived for the injection case the relation to the FST intensity could not be derived. Gad-El-Hak & Corrsin (1974) concluded that the effects of injection are simply too many and complicated. One would have to consider e.g. the effects on the boundary layers around the grid elements, the turbulence levels near the jet exits, and the stability of the system of jets. The experimental investigation revealed that coflow injection reduces the rod wake width, hence lowered the effective solidity, and reduces the static pressure drop across the grid. This in turn leads to a smaller turbulence level at a prescribed distance downstream. In contrary, the counterflow injection increases the effective solidity with increasing jet strength and consequently gives a larger static pressure drop across the grid resulting in larger FST levels. The effective solidity was visualized by means of hydrogen bubble flow technique. The authors claim that the counterflow injection generates higher turbulence energy as well as larger scales, both events being associated with the instability of the jet system.

#### B.1. Design

The active grid was built to be placed in the test-section of the MTL-windtunnel at KTH. The grid consists of a rectangular frame with dimension  $1.2 \times 0.8$  (width  $\times$  height, identical with the test-section dimensions). Each side of this frame is separated from the others and consists of a brass pipe with an outer diameter of 15 mm (wall thickness = 1 mm) and has two inlets for secondary air

in order to reduce the pressure drop inside the grid. A total amount of 33 brass pipes, 20 vertically and 13 horizontally, were then soldered to the frame. These pipes has a diameter ( $d_p$ ) of 5 mm (wall thickness 0.9 mm) and are located to give a mesh width  $M=50$  mm (square) which corresponds to a geometrical solidity ( $S_g$ ) of 0.19. The jet orifices have a diameter of 1.5 mm and are in the present set-up directed upstream. The orifices are concentrated to the middle section of the grid with a total amount of 254 (12 horizontally  $\times$  12 and 11 vertically  $\times$  10, see figure B.1 for an illustration of the grid geometry). The secondary air is supplied to the grid through flexible rubber tubing connected to the inlets at the frame. The air is driven by a modified vacuum cleaner (1 kW) and the jet strength was regulated by a transformer. In the present study three injection rates are used, denoted as  $P = 0$  (no injection), 100 and 200 V, where  $P$  is the voltage supplied to the vacuum cleaner. A fine screen was positioned on the downstream side of the frame in order to improve the homogeneity of the flow.

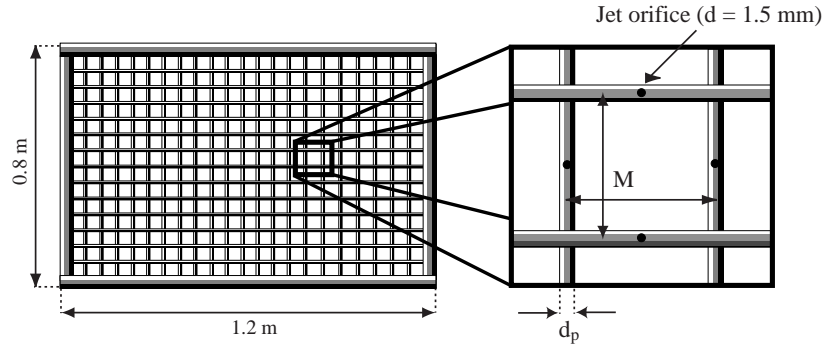


Figure B.1: Active grid with main measures.

## B.2. Characteristic data of the active grid

### B.2.1. Turbulence decay

Downstream of the grid the turbulence decays and the typical power-law decay can be described according to

$$Tu = \frac{u_{rms}}{U_\infty} = C(x - x_0)^b, \quad (\text{B.1})$$

where  $x_0$  is a virtual origo, the constant  $C$  and exponent  $b$  are parameters to be determined through curve fit to experimental data.

In figure B.2 the downstream development of the turbulence intensity ( $Tu$ ), of the active grid is shown. The different injection rates are plotted together

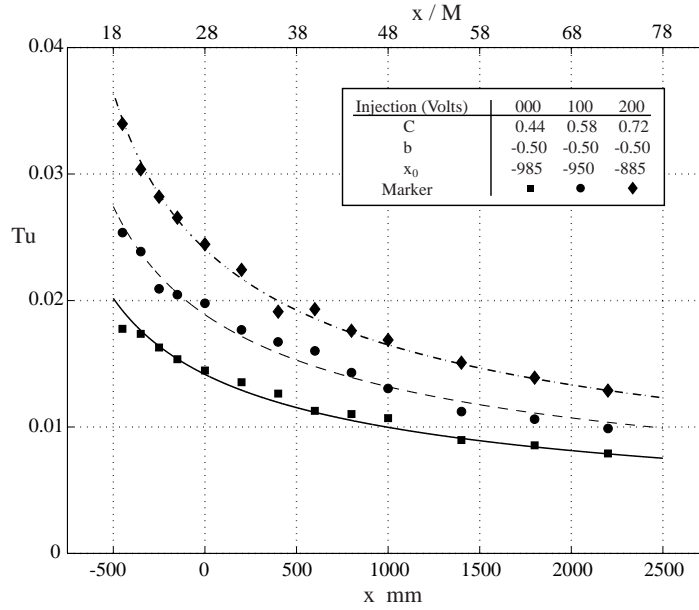


Figure B.2: Turbulence decay for different injection rates. The curves are fitted to experimental data according to equation B.1 for a given  $b = -0.5$ .

with the zero injection case for comparison. The grid distance upstream the leading edge was fixed at  $x = -1400$  mm corresponding to  $28M$  from the leading edge of the plate. The curve fits are done for  $Tu$  with equation B.1 with  $b = -0.5$ , which can be shown to be the actual value of  $b$  for fully isotropic turbulence decay. The virtual origin has been determined consistently by taking the intersection point with the  $x/M$ -axis when  $1/Tu^2 = x/M$  is plotted. A new virtual origin was determined for all three cases and are given in figure B.2 together with the value of the constant  $C$ . This figure clearly shows the increase of  $Tu$  with increasing injection rate for all downstream positions from the grid position.

In figure B.3 the isotropy measure  $v_{rms}/u_{rms}$  is plotted as a function of the downstream distance. The figure shows a nearly isotropic turbulence for all three cases at  $x = -400$  mm downstream the active grid, which is in agreement with the rule of thumb that  $20M$  is needed to establish a nearly isotropic turbulence behind a grid. All three cases have an isotropy measure above 0.9 and the highest  $Tu$  seem to achieve the highest degree of isotropy. According to Groth & Johansson (1988) several investigations have reported that the turbulence behind a grid retains a small degree of anisotropy over a very large downstream

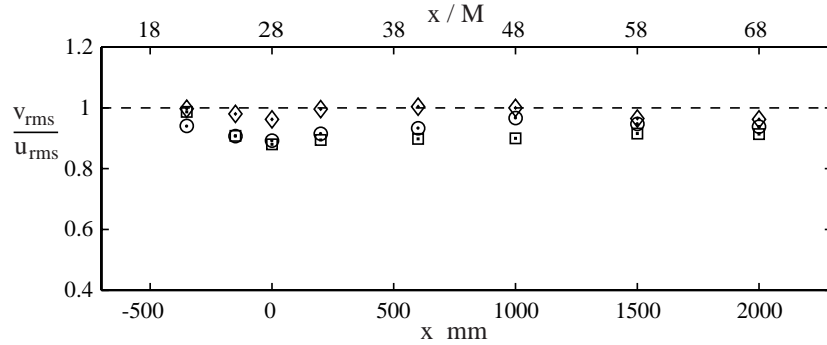


Figure B.3: The isotropy measure  $v_{rms}/u_{rms}$  as a function of the downstream distance. ( $\square$ )  $P = 0$  V, ( $\circ$ )  $P = 100$  V, and ( $\diamond$ )  $P = 200$  V.

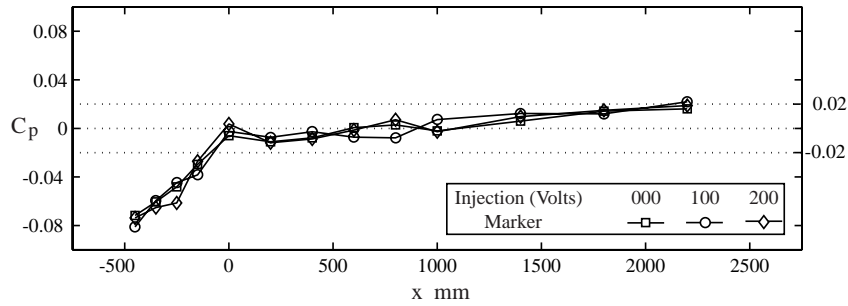


Figure B.4: Pressure distribution vs the downstream distance for different injection rates.

distance (up to  $400M$ ). They report fast return to a nearly isotropic state and explains that the main source for a persisting anisotropy may be large-scale anisotropic turbulence on the upstream side of the grid and that the return to isotropy depends on the macroscale (i.e. integral scale) Reynolds number.

The measurements on the active grid were carried out in connection with a flat plate boundary layer experiment and a large effort was taken to get a zero pressure gradient on the plate (starting at  $x = 0$  mm). This gives rise to a small acceleration in front of the plate. However as can be seen from the pressure coefficient ( $C_p$ ) plotted versus the downstream distance in figure B.4 the mean flow condition stays the same despite the injection from the grid. Since the injection give rise to a larger blockage the rotational speed of the wind-tunnel

fan is increased to compensate for this until the same velocity, measured with a Prandtl tube at a reference position, is achieved. This indicates that the increase of  $Tu$  with increasing injection is real, i.e. it is not due to a mean velocity decrease.

B.2.2. *Turbulence scales*

In addition to the turbulence intensities generated by the grid, the FST scales are of interest. In a turbulent flow the scales ranges from the smallest Kolmogorov scale (which can be determined from the turbulence decay) to the largest geometrically allowed.

The smallest energetic timescale is called the Taylor microscale ( $\lambda_t$ ) and this scale can be estimated directly from the autocorrelation function. Also the the integral (macro) timescale ( $\Lambda$ ) can be obtained from the autocorrelation and is defined as

$$\Lambda = \int_0^\infty R_{uu}(\tau) d\tau, \tag{B.2}$$

where  $R(\tau)$  is the autocorrelation function defined as

$$R_{ij}(\tau) \equiv \frac{\overline{u_i(t)u_j(t')}}{\overline{u_i(t)u_j(t)}},$$

with  $\tau = t' - t$ . Through Taylor's hypothesis (frozen turbulence approximation) the length scales can then be determined and should agree with scales determined from two point spatial correlation functions. This hypothesis holds for  $u/U_\infty \ll 1$  and states that  $u(t) \approx u(x/U)$ . It is hard to estimate the Taylor lengthscale from spatial correlation measurements since this needs a well resolved correlation coefficient curve for small separations. Therefore the timescale is usually determined and the use of Taylor's hypothesis is used to convert to a length scale.

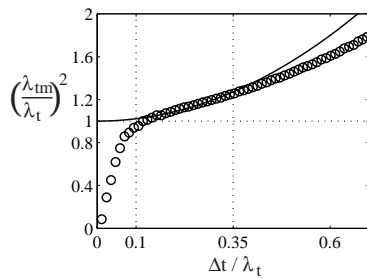


Figure B.5: The function of equation B.4 (solid line) is plotted together with expression B.3 ( $\circ$ ) for determination of  $\lambda_t$ .

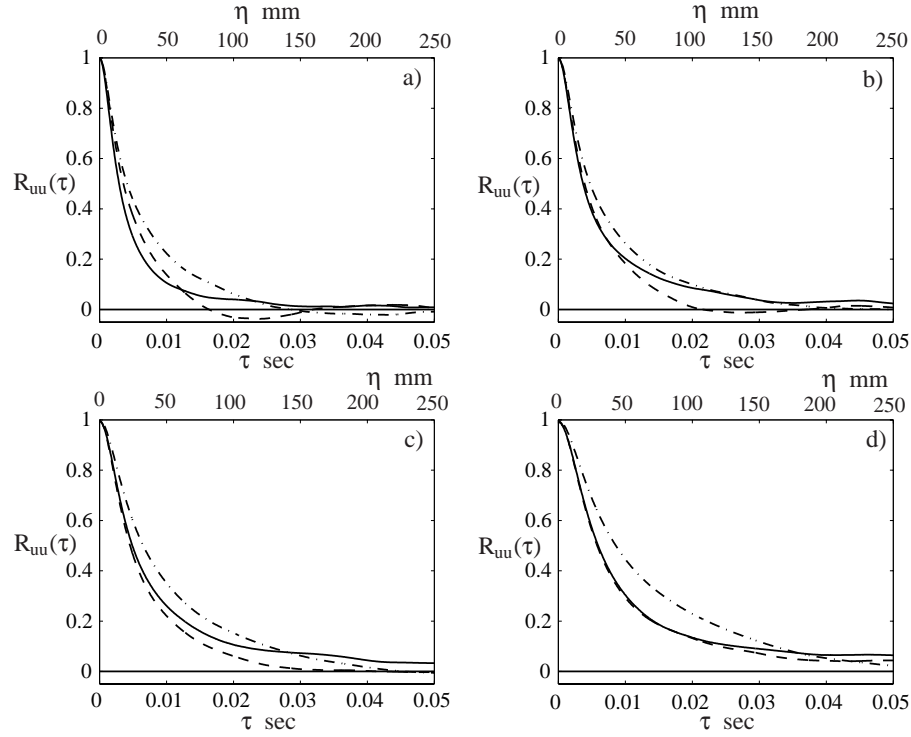


Figure B.6: Autocorrelation comparison between different injection rates and for different downstream positions. a)  $x = -350$  mm, b)  $x = 0$  mm, c)  $x = 1000$  mm, and d)  $x = 2000$  mm. (solid)  $P = 0$  V, (dashed)  $P = 100$  V, and (dash-dotted)  $P = 200$  V.

The Taylor microscale can be defined as

$$\lambda_t^2 \equiv 2 \frac{\overline{u^2}}{(\partial u / \partial t)^2}.$$

This expression is derived through Taylor series expansion of the correlation coefficient function (see e.g. Hinze (1975) or Tennekes & Lumley (1997)) and was used here to determine the Taylor length scale. The same procedure as Hallbäck *et al.* (1989) was used with the exception of approximating the time derivative of the signal with  $\Delta u / \Delta t$ . First the measured (denoted by subscript  $m$ ) time scale is computed according to

$$\lambda_{tm}^2 = 2 \frac{\overline{u^2}}{(\Delta u / \Delta t)^2} \quad (\text{B.3})$$

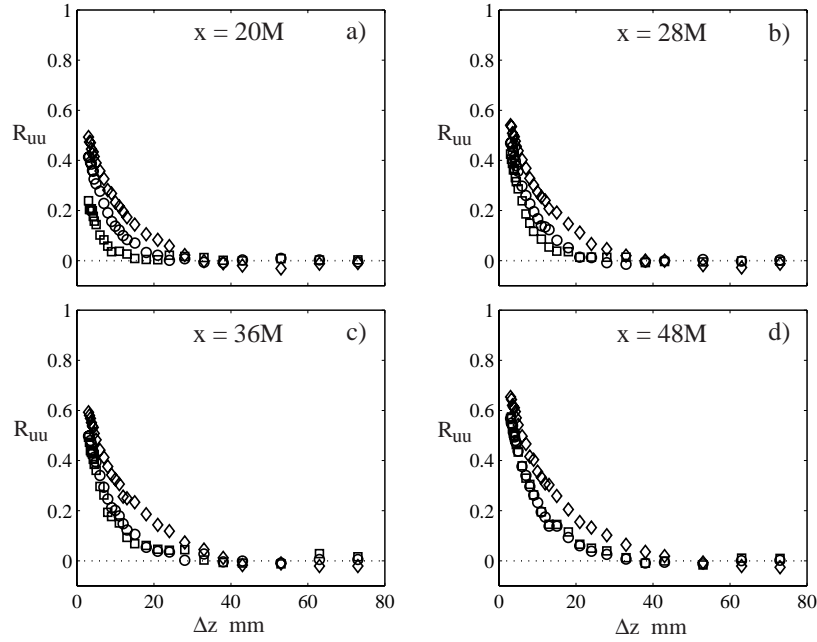


Figure B.7: Spatial correlation comparison between different injection rates and for different downstream positions. a)  $x = -400\text{ mm}$ , b)  $x = 0\text{ mm}$ , c)  $x = 400\text{ mm}$ , and d)  $x = 1000\text{ mm}$ . ( $\square$ )  $P = 0\text{ V}$ , ( $\circ$ )  $P = 100\text{ V}$ , and ( $\diamond$ )  $P = 200\text{ V}$ .

for decreasing  $\Delta t$  (i.e. increasing sampling frequency) and then the expression

$$\left(\frac{\lambda_{tm}}{\lambda_t}\right)^2 = 1 + \beta \frac{\Delta t}{\lambda_t} \quad (\text{B.4})$$

is fitted to data in the region  $0.1 < \Delta t/\lambda_t < 0.35$ , which was suggested by Hallbäck *et al.* (1989) (for increasing downstream distance the lower limit is though shifted towards higher values).  $\lambda_t$  is then accurately obtained and in figure B.5 the data and the curve fit are shown. Hallbäck *et al.* (1989) reported that for very small  $\Delta t$  the effect of electrical noise and insufficient resolution in the AD-converter gives a too low value of the microscale which can be observed in figure B.5 for low  $\Delta t$  values.

The autocorrelation function is shown in figure B.6 for the three different injection cases at four different downstream positions. The autocorrelation is calculated from a 60 sec long time signal sampled at a frequency of 25 kHz. In the figure  $\eta$  is the corresponding spatial separation obtained using Taylor's hypothesis. There is a relatively small difference between the three cases,

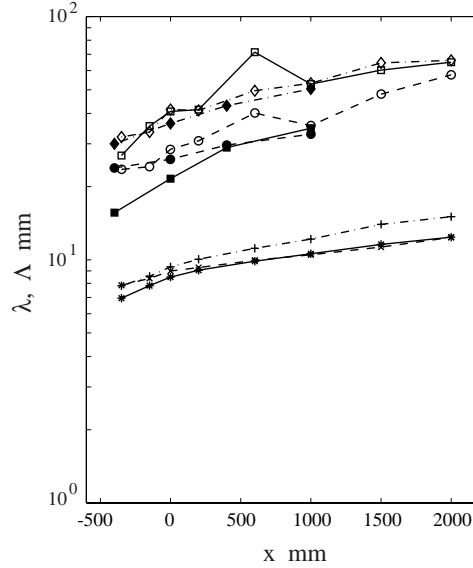


Figure B.8: The Taylor ( $\lambda$ ) and the Integral ( $\Lambda$ ) lengthscale evolution. ( $\square, *$ )  $P = 0$  V, ( $\circ, \times$ )  $P = 100$  V, and ( $\triangle, +$ )  $P = 200$  V. ( $*$ ,  $\times$ ,  $+$ ) denotes  $\lambda$  and filled markers of  $\Lambda$  are from spatial correlation measurements and unfilled from the autocorrelation.

although a tendency for the highest injection rate to be correlated over the longest times. It is however clear that a typical correlation time increases with downstream distance for all three cases. Similar results are obtained from spatial (in the spanwise direction) correlation measurements using two hot-wires. Results from such measurements are shown in figure B.7. At  $x = 40M$  the correlation functions clearly show that the scales increase with increasing injection, whereas further downstream the differences between the three cases decrease. It is also seen that the correlation extends over larger distances when  $x$  increases which is in accordance with the results obtained from the autocorrelation function.

In figure B.8 the downstream evolution of  $\lambda$  and  $\Lambda_{t,z}$ , respectively, are plotted. For the calculation of  $\Lambda$  through expression B.2 the above integration limit was truncated at  $\tau = 0.1$  sec for the autocorrelation and  $\Delta z = 70$  mm for the spatial correlation. From the timescale to the length scale Taylor's hypothesis was used. The integral length scales obtained from the spatial correlation is slightly smaller than the one obtained from the autocorrelation, which is in agreement with theoretical results for isotropic turbulence. The lengthscales are seen to grow in the downstream direction and the Taylor lengthscales seem

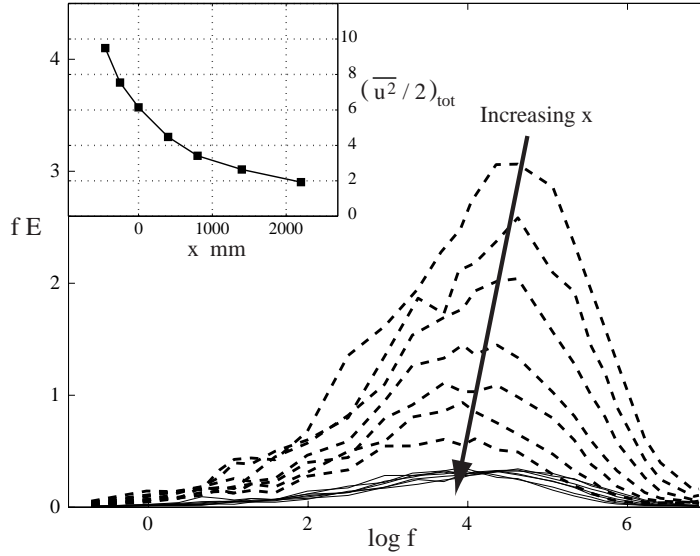


Figure B.9: Energy spectra at different downstream positions ( $x = [-450 -250$   $0$   $400$   $800$   $1400$   $2200]$  mm) for the zero injection case.

to increase slightly with increasing injection which is in agreement with Gad-El-Hak & Corrsin (1974).

### B.2.3. Energy spectra

The energy spectra gives a good overview of the turbulent scales for the different injection rates. If the energy distribution over the frequencies are the same it is most likely that they also share the same energetic scales, i.e. turbulent lengthscales. In figure B.9 the energy ( $f \cdot E$ ) is plotted versus the frequency ( $\log(f)$ ) (dashed-line) for the no-injection case. It shows clearly that the main energy content moves towards lower frequencies with downstream distance, indicating an increase (in size) of the integral lengthscales (most energetic scale). The solid lines represents the total energy when normalized to unity for all positions. In the top left corner of this figure the total kinetic energy ( $(\overline{u^2}/2)_{tot} = \int_0^\infty f E d(\log f)$ ) is plotted versus the downstream distance and can be compared with the  $Tu$  decay plotted in figure B.2.

The energy spectra (normalized to make the total kinetic energy equal to unity) for all three injection rates are compared in figure B.10 at different downstream positions. This figure shows that the variation of the energy distribution is small for the different injection rates, although a slight shift towards lower frequencies can be seen for increasing injection. It is also clearly seen that the

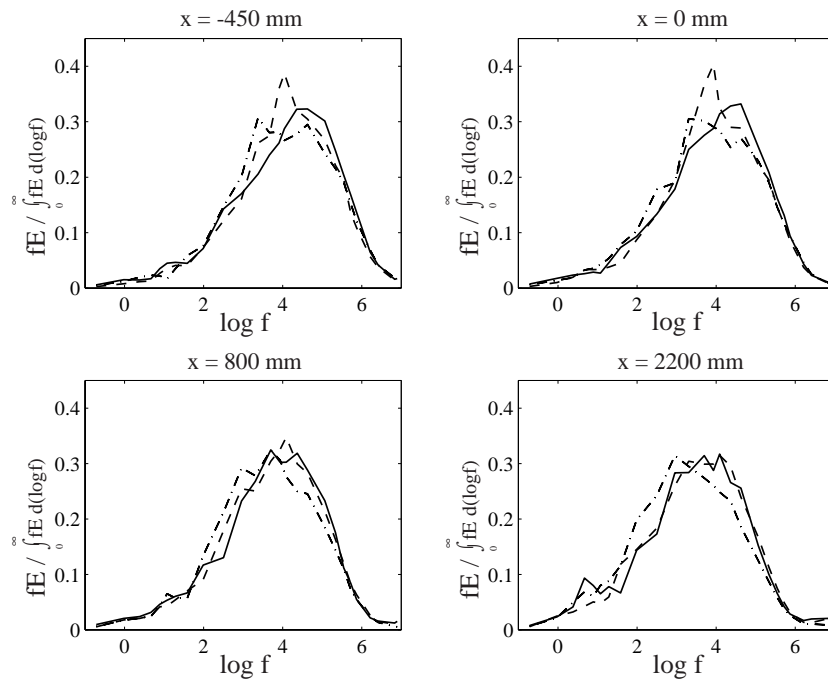


Figure B.10: Energy spectras at different downstream positions for all three injection rates. (solid)  $P = 0$  V, (dashed)  $P = 100$  V and (dash-dotted)  $P = 200$  V.

maxima in the distributions move towards lower frequencies with downstream distance. A similar increase in the turbulence scales was observed in figure B.8.

## Acknowledgment

First of all I would like to thank my supervisor Prof. Henrik Alfredsson for his encouragement, valuable advices and for giving me the opportunity to be absorbed in fluid dynamics.

Secondly, I would like to thank Dr. Johan Westin who has shared his knowledge in the area and helped me out during the experiments.

I wish to thank Dr. Nils Tillmark and all colleagues in the lab at the Department of Mechanics for making the workplace "laminar" and pleasant. Special thanks goes to Dr. Masaharu Matsubara who was my first tutor in experimental work, Dr. Carl Häggmark for taking time to explain many basic things for a novice, Dr. Ardeshir Hanifi for showing his interest and for helpful discussions, Dr. Ola Widlund for his ideas and comments on the practical use of CFX, and Lic. Fredrik Lundell for interesting discussions and practical advices.

I also want to thank Marcus Gällstedt and Ulf Landén for all help and ideas during the plate construction and Marcus for making the leading edge. Dr. Alessandro Talamelli is thanked for introducing me to the world of running and all discussions and stimulation on the running tracks around Stockholm.

Finally I want to thank my family for all their support, especially Annika for her love and understanding.

Funding by the Swedish Research Council (VR) is acknowledged. The Department of Machine Elements and the Department of Aeronautics are acknowledged for their collaboration of measuring the roughness and performing the load test of the porous material, respectively.

## References

- ANDERSSON, P., BRANDT, L., BOTTARO, A. & HENNINGSON, D. S. 2001 On the breakdown of boundary layer streaks. *J. Fluid Mech.* **428**, 29–60.
- CRABTREE, L. F., GADD, G. E., GREGORY, N., ILLINGWORTH, C. R., JONES, C. W., KÜCHEMANN, D., LIGHTHILL, M. J., PANKHURST, R. C., ROSENHEAD, L., SOWERBY, L., STUART, J. T., WATSON, E. J. & WHITHAM, G. B. 1963 *Laminar boundary layers*. Oxford University Press.
- DRAZIN, P. G. & REID, W. H. 1981 *Hydrodynamic stability*. Cambridge University Press.
- ELOFSSON, P. 1998 Experiments on oblique transition in wall bounded shear flows. PhD thesis, Royal Institute of Technology, TRITA-MEK Tech. Rep. 1998:05.
- FASEL, H. & KONZELMANN, U. 1990 Non-parallel stability of a flat-plate boundary layer using the complete Navier-Stokes equations. *J. Fluid Mech.* **221**, 311–347.
- GAD-EL-HAK, M. & CORRISIN, S. 1974 Measurements of the nearly isotropic turbulence behind a uniform jet grid. *J. Fluid Mech.* **62**, 115–143.
- GREGORY, N. 1961 Research on suction surfaces for laminar flow. *Boundary Layer and Flow Control II*, 924–957.
- GROTH, J. & JOHANSSON, A. V. 1988 Turbulence reduction by screens. *J. Fluid Mech.* **197**, 139–155.
- GUSTAVSSON, C. 2000 Development of three-dimensional disturbances in boundary layers with suction. Master Thesis at the Luleå University of Technology.
- HAINS, F. D. 1967 Stability of plane Couette-Poiseuille flow. *Phys. Fluids* **10**, 2079–2080.
- HAINS, F. D. 1971 Stability of plane Couette-Poiseuille flow with uniform crossflow. *Phys. Fluids* **14**, 1620–1623.
- HAJ-HARIRI, H. 1988 Transformations reducing the order of the parameter in differential eigenvalue problems. *J. Comp. Phys.* **77**, 472–484.
- HALLBÄCK, M., GROTH, J. & JOHANSSON, A. V. 1989 A reynolds stress closure for the dissipation in anisotropic turbulent flows. *Seventh Symposium on Turbulent Shear Flows 17-2*, 17.2.1–17.2.6.
- HINZE, J. O. 1975 *Turbulence*. McGraw-Hill book company.
- HOCKING, L. M. 1975 Non-linear instability of the asymptotic suction velocity profile. *Quart. J. Mech. Appl. Math.* **28**, 341–353.

- JACOBS, R. G. & DURBIN, P. A. 2001 Simulations of bypass transition. *J. Fluid Mech.* **428**, 185–212.
- JOHANSSON, A. V. & ALFREDSSON, P. H. 1982 On the structure of turbulent channel flow. *J. Fluid Mech.* **122**, 295–314.
- JOSLIN, R. D. 1998 Aircraft laminar flow control. *Annu. Rev. Fluid Mech.* **30**, 1–29.
- KENDALL, M. J. 1985 Experimental study of disturbances produced in a pre-transitional laminar boundary layer by weak free stream turbulence. *AIAA Paper* **85-1695**.
- KLINGMANN, R. G. B., BOIKO, A. V., WESTIN, K. J. A., KOZLOV, V. V. & ALFREDSSON, P. H. 1993 Experiments on the stability of tollmien-schlichting waves. *Eur. J. Mech., B/Fluids* **12(4)**, 493–514.
- LANDAHL, M. T. 1980 A note on an algebraic instability of inviscid parallel shear flows. *J. Fluid Mech.* **98**, 243–251.
- LUCCINI, P. 2000 Reynolds number independent instability of the boundary layer over a flat surface: optimal perturbations. *J. Fluid Mech.* **404**, 289–309.
- LUNDELL, F. 2000 Streak breakdown and transition control in wall-bounded flows. TRITA-MEK Tech. Rep. 2000:06. Licentiate Thesis at the Royal Institute of Technology.
- MACMANUS, D. G. M. & EATON, J. A. 2000 Flow physics of discrete boundary layer suction-measurements and predictions. *J. Fluid Mech.* **417**, 47–75.
- MATSUBARA, M. & ALFREDSSON, P. H. 2001 Disturbance growth in boundary layers subjected to free-stream turbulence. *J. Fluid Mech.* **430**, 149–168.
- MORKOVIN, M. V. 1969 *The many faces of transition*. In *Viscous Drag Reduction*, Plenum Press.
- MYOSE, R. Y. & BLACKWELDER, R. F. 1995 Control of streamwise vortices using selective suction. *AIAA J.* **33(6)**, 1076–1080.
- ORSZAG, S. A. & PATERA, A. 1983 Secondary instability in wall-bounded shear flows. *J. Fluid Mech.* **128**, 347–385.
- ÖSTERLUND, J. M. 1999 Experimental studies of zero pressure-gradient turbulent boundary layer flow. PhD thesis, Royal Institute of Technology, TRITA-MEK Tech. Rep. 1999:16.
- PFENNINGER, W. & GROTH, E. 1961 Low drag boundary layer suction experiments in flight on a wing glove of an F-94A airplane with suction through a large number of fine slots. *Boundary Layer and Flow Control* **II**, 981–999.
- POLL, D. I. A., DANKS, M. & DAVIES, A. J. 1992*a* The effect of surface suction near the leading edge of a swept-back wing. *First European Forum on Laminar Flow Technology* pp. 278–293.
- POLL, D. I. A., DANKS, M. & HUMPHREYS, B. E. 1992*b* The aerodynamic performance of laser drilled sheets. *First European Forum on Laminar Flow Technology* pp. 274–277.
- POTTER, M. C. 1966 Stability of plane Couette-Poiseuille flow. *J. Fluid Mech.* **24**, 609–619.
- RESHOTKO, E. 2001 Transient growth: A factor in bypass transition. *Phys. Fluids* **13(5)**, 1067–1075.

- REYNOLDS, G. A. & SARIC, W. S. 1986 Experiments on the stability of the flat-plate boundary layer with suction. *AIAA J.* **24**(2), 202–207.
- RHEINBOLDT, W. 1956 Zur Berechnung stationärer Grenzschichten bei kontinuierlicher Absaugung mit un stetig veränderlicher Absaugengeschwindigkeit. *J. Rational Mech. Anal.* **5**, 539–604.
- ROSS, J. A., BARNES, F. H., BURNS, J. G. & ROSS, M. A. 1970 The flat plate boundary layer. part 3. comparison of theory and experiments. *J. Fluid Mech.* **43**, 819–832.
- SARIC, W. S. 1994 Low-speed experiments: requirements for stability measurements. *In: Transition, Experiments, Theory and Computations*, Eds. T. C. Corke, G. Erlebacher and M. Y. Hussaini, Oxford.
- SCHLICHTING, H. 1979 *Boundary layer theory*. McGraw-Hill book company.
- SCHMID, P. J. & HENNINGSON, D. S. 2001 *Stability and transition in shear flows*. Springer-Verlag New York, Inc.
- SCHUBAUER, G. B. & SKRAMSTAD, H. K. 1948 Laminar boundary layer oscillations and transition on a flat plate. *Technical Report Rep. 909*, NACA.
- SHEPPARD, D. M. 1972 Hydrodynamic stability of the flow between parallel porous walls. *Phys. Fluids* **15**, 241–244.
- TAYLOR, G. I. 1971 A model for the boundary condition of a porous material. part 1. *J. Fluid Mech.* **49**, 319–326.
- TENNEKES, H. & LUMLEY, J. L. 1997 *A first course in turbulence*. The MIT Press.
- WESTIN, J. 1997 Laminar-turbulent boundary layer transition influenced by free stream turbulence. PhD thesis, Royal Institute of Technology, TRITA-MEK Tech. Rep. 1997:10.

Paper 1

1



# Growth and breakdown of streaky structures in boundary layer transition induced by free stream turbulence

By M. Matsubara<sup>†‡</sup>, A.A. Bakchinov<sup>\*</sup>, J.H.M. Fransson<sup>†</sup> and P.H. Alfredsson<sup>†</sup>

<sup>†</sup>Department of Mechanics, Royal Institute of Technology (KTH), S-100 44 Stockholm, Sweden

<sup>‡</sup>Institute of Fluid Science, Tohoku University, Sendai, 980-8577, Japan

<sup>\*</sup>Present address, Thermo and Fluid Dynamics, Chalmers, S-412 96 Göteborg, Sweden

Laminar-Turbulent Transition 2000, *Proc. IUTAM Symp. Laminar-Turbulent Transition*, Sedona, Sept. 13-17, 1999 (eds. Fasel, H.F. & Saric, W.S.), pp. 371-376, Springer.

Freestream turbulence is maybe the most important source to force by-pass transition in boundary layer flows. The present study aims at describing the initial growth of streamwise oriented disturbances in the boundary layer and relate this growth to recent theories of non-modal growth of such disturbances, but also to lay the ground for a predication model for free stream turbulence induced transition. It is shown that the initial growth is linear and proportional to the free stream turbulence energy. The spanwise scale of the disturbance does not change in the downstream direction and is probably determined by the scale of the free stream turbulence.

---

## 1. Introduction

It is known from both flow visualization and hot-wire measurements that a boundary layer subjected to free stream turbulence (FST) develops unsteady streaky structures with high and low streamwise velocity (for a review see Kendall, 1998). This leads to large amplitude, low frequency fluctuations inside the boundary layer although the mean flow is still close to the laminar profile. Figure 1 shows a visualization of a typical boundary layer transition induced by free stream turbulence. It is apparent that the free stream turbulence gives rise to longitudinal structures in the flow with a relatively well defined spanwise scale. The streaks are subsequently seen to develop a streamwise waviness of relatively short wave length, which develops into turbulent spots. Quantitative measurements of this scenario, especially growth rate and

scales of the longitudinal streaks, are important to obtain accurate physical modeling of these processes and they are also needed for development of a reliable prediction method.

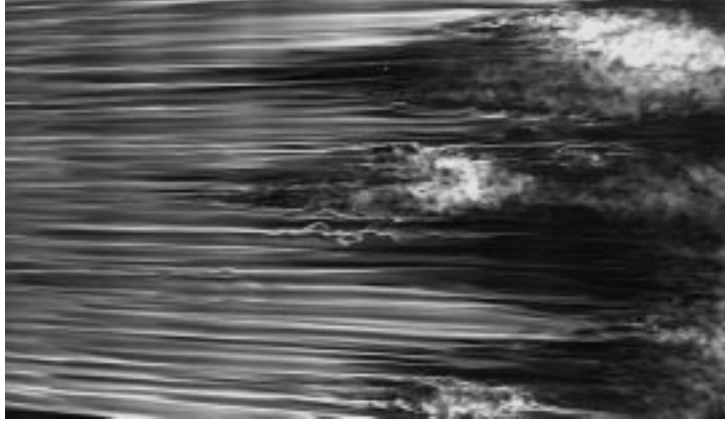


Figure 1: Flow visualization of streaky structures in boundary layers affected by free stream turbulence. Flow direction is from left to right.  $Tu=2.2\%$ ,  $U_\infty=6$  m/s.

Several experimental studies have recently investigated transition under the influence of free stream turbulence. Kendall (1985) observed low-frequency fluctuations in the boundary layer that grows in linear proportion to  $x^{1/2}$  (i.e. proportional to the laminar boundary layer thickness,  $\delta$ ). He also observed the occurrence of elongated streamwise structures with narrow spanwise scales (in the following denoted streaky structures). Also Westin et al. (1994) made detailed measurements of a laminar boundary layer disturbed by free stream turbulence and showed among other things that the Blasius profile was only slightly modified, despite  $u_{rms}$  levels of about 10 % inside the boundary layer before breakdown. They also confirmed that the growth of  $u_{rms}$  was proportional to  $x^{1/2}$ . In a theoretical analysis of non-modal growth in boundary layer flow, Luchini (1996,1997) found that if optimal perturbations were used, i.e. perturbations that maximize the energy growth, the energy growth was proportional to  $x$  (or equivalently the streamwise disturbance velocity increased as  $x^{1/2}$ ). In his analysis the spanwise wave number ( $\beta$ ) was kept constant and at a given  $x$  the optimal growth was obtained when  $\beta\delta=0.45$ . This would suggest that the average spanwise spacing of streaks would increase as  $x^{1/2}$  in the downstream direction, however in a physical experiment the spanwise scale is strongly influenced by the scale of the free stream turbulence.

The present investigation focuses on the streamwise and spanwise scaling of the streaky structure in boundary layer flow which is subjected to free stream turbulence. The experiments were made in the MTL wind tunnel at KTH where a 2 m long test plate was mounted horizontally in the test section. The free stream turbulence was generated by grids of various size placed at the start of the test section. Three different grids were used to generate turbulence levels ( $Tu$ ) in the range 1.4 to 6.7% at the streamwise position of the plate leading edge, and the free stream velocity was in the range 2 to 14 m/s. One of the grids is active, i.e. the grid consists of pipes with small orifices directed upstream from which air is injected into the flow. By varying the flow rate the turbulence level in the test section can be changed without significantly changing the turbulence scale. A traversing system allows movements along the test section and normal to the plate. At the end of the sting a small traverse was mounted which allows one probe to be moved in the spanwise direction, whereas another probe was fixed to the sting, so that the two probes were located at the same distance from the wall. This enables measurements of the spanwise correlation which in turn makes it possible to calculate two dimensional spectra (using Taylor's hypothesis in the streamwise direction).

## 2. Results

A contour map of the spanwise correlation of the streamwise velocity fluctuations in a plane normal to the stream direction is shown in figure 2. At  $y=4$  mm, which corresponds to the middle of the boundary layer, the minimum value of the correlation is less than -0.3 while in the outside of the boundary layer ( $y > 10$  mm) the correlation never becomes negative. In the boundary layer, the spanwise separation at the minimum correlation is about 12 mm, independent of the distance from the wall. This result and the observation of low frequency fluctuations in the velocity signal indicate the existence of unsteady streaky structures in the boundary layer.

The spanwise correlation measurements with two hot wires can be used to obtain two-dimensional power spectra in the streamwise and spanwise directions by Fourier transformation. Two-dimensional wave-number spectra obtained at  $y/\delta=0.5$  are shown in figure 3. The peak of the spectrum in figure 3a is located at the streamwise wavenumber  $\alpha=0$  and the spanwise wavenumber  $\beta=0.25$  mm<sup>-1</sup>, which shows the longitudinal streaky character of the disturbance.

The spectrum at a position further downstream as shown in figure 3b does not change if the streamwise wavenumber is scaled with  $\delta^*$  ( $\delta^*$  is the displacement thickness which is proportional to  $x^{1/2}$ ) and the spanwise wavenumber is kept dimensional. It is worth noticing that the energy density is scaled with  $x^{3/2}$ , which shows that the total disturbance energy is proportional to  $x$ . The energy growth is in accordance with the result of Luchini (1997), however the constancy of the most amplified spanwise wave number is in contrast with the

theory. The spectral distribution with this scaling was found to be similar also at other free stream velocities.

Figure 4 shows the transition Reynolds number as function of the free stream turbulence level for several different grids, including the active grid. Also included in the graph is a curve proportional to  $Tu^{-2}$ . The transitional Reynolds number is determined at the position where the intermittency  $\gamma$  was estimated as 0.5. The agreement between the curve and the measured transition points is remarkable.

Figure 5 shows data from the same measurements as in figure 4. In figure 5a the streamwise disturbance energy ( $E = (u_{rms}/U_\infty)^2$ ), measured at  $y/\delta^*=1.4$ , is plotted as function of  $Re_x$ . A typical curve shows an initial nearly linear growth, after which it reaches a maximum and then asymptotes to a constant level. The maximum is closely related to the point of  $\gamma=0.5$ , i.e. at this point the flow alternatively consists of laminar portions and turbulent spots. The higher the  $Tu$ , the smaller the  $Re_x$ , for which the maximum occurs. Figure 5b shows the maximum value of each curve which slightly decreases with the peak Reynolds number. This is consistent with the idea that when  $Re_x$  increases the disturbance threshold for breakdown will decrease. Figure 5c shows the

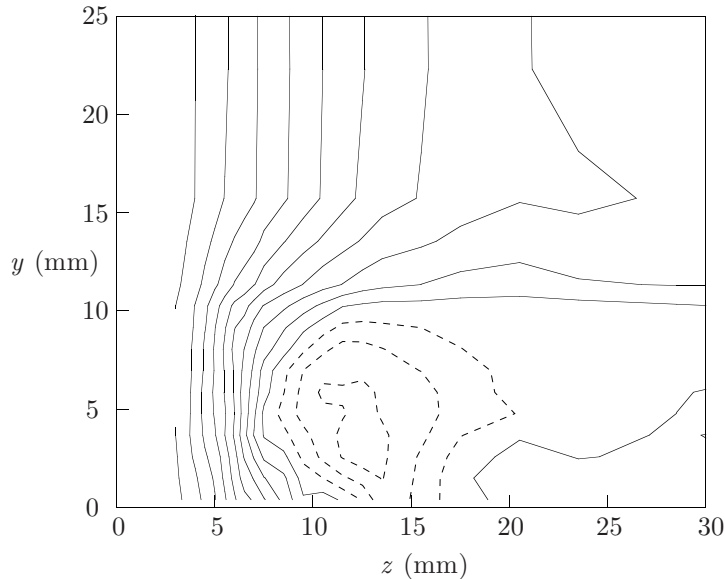


Figure 2: Contour map of spanwise correlation in  $yz$ -plane. Dashed lines represent negative contours. Number of points in  $y$  are 15, in  $z$  are 26.  $Tu=1.5\%$ .  $U_\infty=5$  m/s.  $x=1600$  mm.

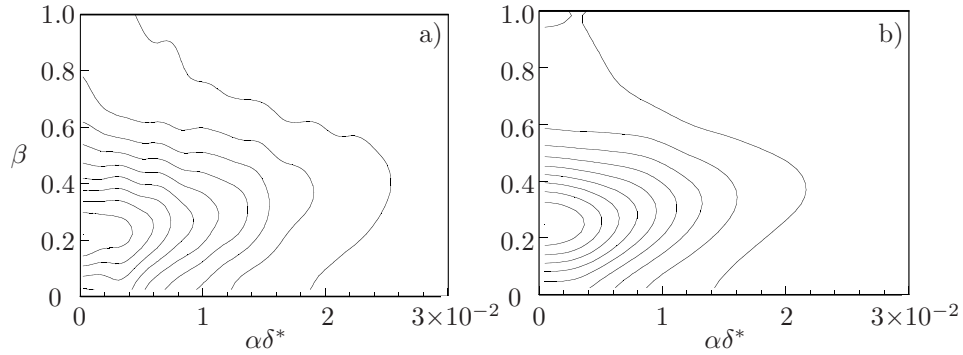


Figure 3: Two dimensional wave number spectra.  $Tu=1.5\%$ .  $U_\infty=5$  m/s. (a)  $x=200$  mm.  $u_{rms}=0.14$  m/s. (b)  $x=800$  mm.  $u_{rms}=0.26$  m/s.

square root of the slope of the linear region for all the curves in figure 5a and it can be seen that this quantity is proportional to  $Tu$  (or equivalently the slope is proportional to the energy of the FST). This strongly indicates

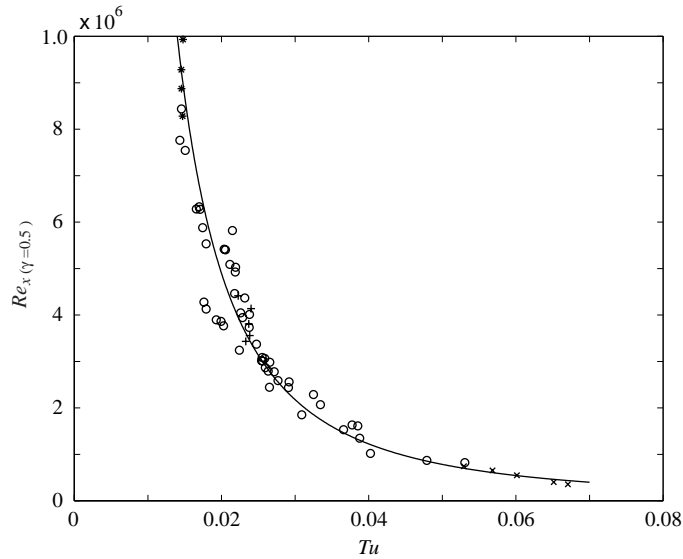


Figure 4: Transitional Reynolds number (defined from  $\gamma=0.5$ ) as function of free stream turbulence level. Open circles denotes measurements with the active grid, other symbols are various passive grids.

that there is a linear response between the free stream disturbances and the disturbance amplitude in the boundary layer. This result and an assumption that the breakdown occurs at a nearly constant level of the disturbances in the boundary layer lead to a simple transition criterion, i.e. that the transition Reynolds number is proportional to  $Tu^{-2}$  as shown in figure 5a. In figure 5d the measured points are plotted where the  $x$ -axis has been scaled with the interpolated  $x$ -value for which  $E=0.01$ . As expected all points fall nicely onto one curve, however the most interesting feature is that a line fitted through the points will cross the abscissa at some positive value of  $x$ . This shows that there is a receptivity process after which the disturbance starts to grow linearly.

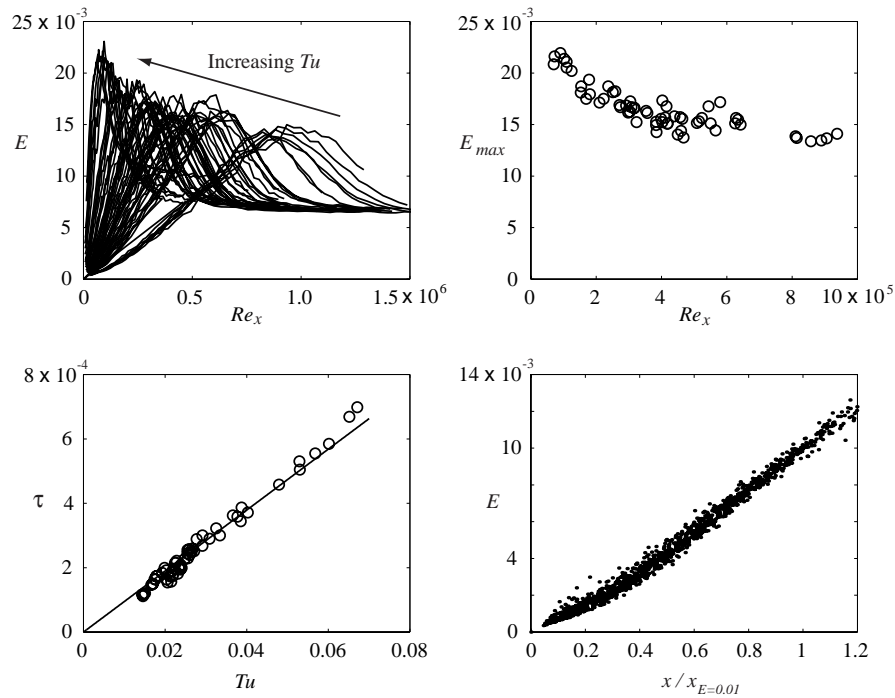


Figure 5: (a) Streamwise turbulent energy as function of  $Re_x$  for various free stream turbulence levels. Measurements are made at  $y/\delta^*=1.4$ , (b) the maximum value of  $E$  as function of its  $Re_x$ . Same data as in previous figure, (c) Slope of line as function of  $Tu$ . (d) Measured points in (a) where horizontal axis is scaled with the position where  $E=0.01$ .

### 3. Conclusions

The present study shows through detailed measurements that the structure of a laminar boundary layer which is affected by free stream turbulence develops longitudinal structures. The amplitude of the disturbance increases as  $x^{1/2}$ . Two-point measurements also give quantitative spatial data showing that the spanwise size of the disturbance does not grow in the downstream direction but probably is given already by the receptivity process. The transition Reynolds number seems to decrease as  $Tu^{-2}$  which is in accordance with the model proposed by Andersson, Berggren, & Henningson (1999). Correspondingly the growth of the disturbance energy was shown to be proportional to  $Tu^2$ .

### Acknowledgment

This research is partly financed through TFR, the Swedish Research Council for Engineering Sciences. Dr Matsubara was supported by JSPS Research Fellowships for Young Scientists. Dr Bakchinov was supported through a Göran Gustafsson post-doc position.

### References

- Andersson, P., Berggren, M. & Henningson, D.S. 1999 Optimal disturbances and bypass transition in boundary layers. *Phys. Fluids* **11**, 134–150
- Kendall, M. J. 1985 Experimental study of disturbances produced in a pre-transitional laminar boundary layer by weak free stream turbulence. AIAA Paper 85-1695.
- Kendall, M. J. 1998 Experiments on boundary-layer receptivity to free-stream turbulence. AIAA paper 98-0530.
- Luchini, P. 1996 Reynolds-number-independent instability of the boundary layer over a flat surface. *J. Fluid Mech* **327**, 101–115.
- Luchini, P. 1997 Reynolds number independent instability of the boundary layer over a flat surface. Part 2: Optimal perturbations. (preprint).
- Westin, K. J. A., Boiko, A. V., Klingmann, B. G. B., Kozlov, V. V. & Alfredsson, P. H. 1994 Experiments in a boundary layer subjected to free-stream turbulence. Part 1. Boundary layer structure and receptivity. *J. Fluid Mech.* **281**, 193–218.



## Paper 2

2



# Errors in hot-wire X-probe measurements induced by unsteady velocity gradients

By Jens H.M. Fransson and K. Johan A. Westin

Department of Mechanics, Royal Institute of Technology (KTH), S-100 44  
Stockholm, Sweden

Accepted for publication in *Experiments in Fluids*.

Errors in hot-wire X-probe measurements due to unsteady velocity gradients are investigated by a comparison of hot-wire and LDV-measurements (Laser Doppler Velocimetry). The studied flow case is a laminar boundary layer subjected to high levels of free stream turbulence, and the hot-wire data shows a local maximum in the wall-normal fluctuation velocity inside the boundary layer. The observed maximum is in agreement with existing hot-wire data, but in conflict with the present LDV-measurements as well as existing results from numerical simulations. An explanation to the measurement error is suggested in the paper.

---

## Introduction

It is well known that strong spatial mean velocity gradients can distort measurements obtained by hot-wire X-probes if the size of the probe can not be considered small as compared to the flow structures in question. In some cases correction procedures can be applied with success, for example Cutler & Bradshaw (1991) applied a linear correction procedure to correct X-probe measurements of the spanwise velocity component in a boundary layer<sup>1</sup>. In a recent paper by Talamelli *et al.* (2000) errors observed when measuring the wall-normal component in a boundary layer was thoroughly investigated using a special probe which allowed a continuous variation of the relative displacement of the two wires of the probe. Both first and second order correction terms could be estimated, and successful corrections of the mean normal velocity ( $\overline{V}$ ) as well as the turbulent shear stress ( $\overline{uv}$ ) were shown.

The free stream turbulence (FST) induces unsteady streaky structures of high and low streamwise velocity inside the boundary layer (for more details, see e.g. Westin 1997, Matsubara & Alfredsson 2001). This can be observed as a large amplitude low-frequency fluctuation primarily in the streamwise

---

<sup>1</sup>In the present paper the streamwise, wall-normal and spanwise directions are denoted by  $x$ ,  $y$  and  $z$ , and the corresponding velocities with  $U$ ,  $V$  and  $W$ .

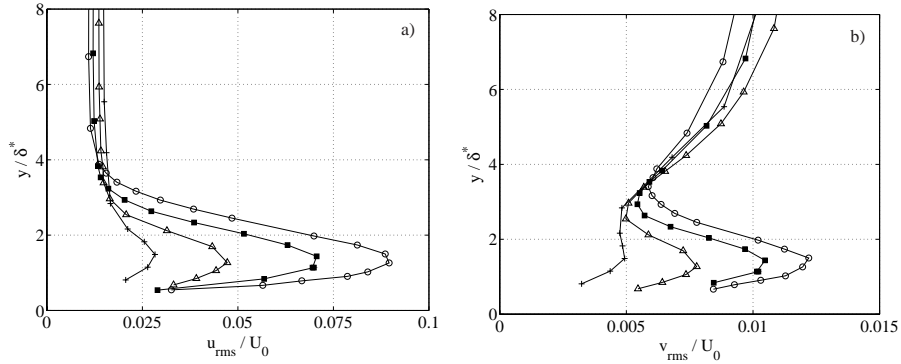


Figure 1: Profiles of a)  $u_{rms}$  and b)  $v_{rms}$  in the pseudo-laminar boundary layer at  $Tu = 1.5\%$  ( $U_0 = 8$  m/s). The different  $x$ -positions are 100 mm ( $R = 400$ ) (+), 250 mm ( $R = 630$ ) ( $\Delta$ ), 500 mm ( $R = 890$ ) (■) and 800 mm ( $R = 1120$ ) (○).

component (see figure 1). However, most available measurements of the wall-normal fluctuations (Arnal & Juillen 1978, Roach & Brierley 1992 and Westin 1997), which are all obtained using X-wire probes, also reveal a local maximum in  $v_{rms}$  inside the boundary layer. This is in contradiction to both large eddy and direct numerical simulations (Voke & Yang 1995, Rai & Moin 1991 and Jacobs & Durbin 2001), which have not been able to reproduce this peak in  $v_{rms}$ . In addition to that, theoretical studies based on the concept of nonmodal disturbance growth (often denoted transient growth, see e.g. Andersson *et al.* 1999) do not predict any spatial amplification of the wall-normal disturbance energy.

To clarify this discrepancy between experimental results and computations it was decided to compare measurements with hot-wire anemometry (HWA) and Laser Doppler Velocimetry (LDV) in a laminar boundary layer subjected to FST (sometimes denoted a pseudo-laminar boundary layer). In addition to experimental results, an explanation to the observed measurement error is suggested.

### Experimental and evaluation techniques

The experiments were carried out in the MTL wind tunnel at KTH. The results shown in figure 1, which in the following will be denoted the “old” data, were measured on a 4 m long flat plate with a turbulence level of 1.5% at the leading edge. For more details about the experimental set-up and the grid generated turbulence, see Westin *et al.* (1994). The so-called “new” results shown in

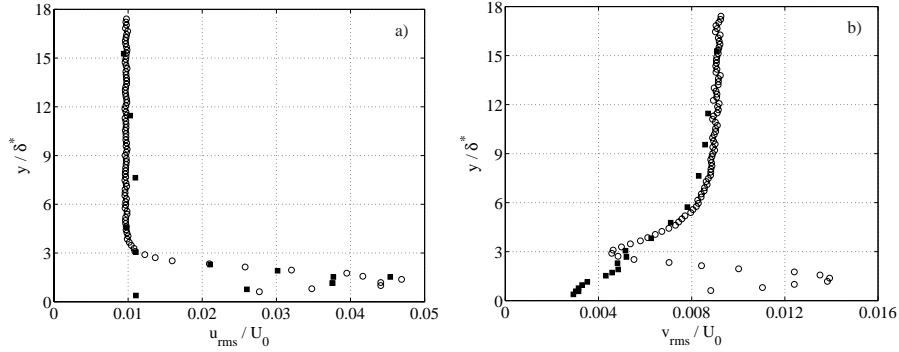


Figure 2: Profiles of a)  $u_{rms}$  and b)  $v_{rms}$  in the pseudo-laminar boundary layer at  $Tu = 1.5\%$  ( $U_0 = 4.5$  m/s) and  $x = 700$  mm ( $R = 790$ ).  $\circ$  HWA-data;  $\blacksquare$  LDV-data.

figure 2 were obtained on a slightly different 6 m long flat plate, but otherwise the two experimental set-ups were similar.

In the HWA-technique an X-probe was used to measure the streamwise and wall-normal velocity components operating in CTA mode. The probe was made of  $2.5 \mu\text{m}$  platinum wires and had a measurement volume less than  $1 \text{ mm}^3$  (side length  $\leq 1$  mm) for the new data (figure 2). The old data (figure 1) was taken with a smaller probe with a wire separation of 0.5 mm. The calibration was done at different angles and flow velocities, and two fifth-order polynomials were fitted to the calibration data, giving  $U$  and  $V$  as functions of the obtained voltage pair (E1,E2).

In the LDV-measurements an integrated one dimensional laser-optics unit was used, including a 10 mW He-Ne laser of wavelength 632.8 nm. A beam expander was mounted to the lens to reduce the measurement volume, which can be approximated as an ellipsoid with axes lengths 0.14 mm and 2.4 mm. To be able to measure the wall-normal component close to the wall the probe has to be inclined. This causes an error which in the present case was estimated to be less than 0.2%. To provide a uniform seeding smoke from a smoke generator was injected downstream of the test section in the closed-loop wind tunnel.

The LDV-data presented are residence time weighted, i.e. each particle is weighted with its transit time. The LDV-unit only allows fixed bandwidths to be changed by the user, and the choice influences the background noise level in the measured data. In the present flow case with a dominant mean flow direction along  $x$  it was possible to choose a more narrow (and better suited) bandwidth for the wall-normal component than for the streamwise one. In the present study two different bandwidths were used for the measurements of

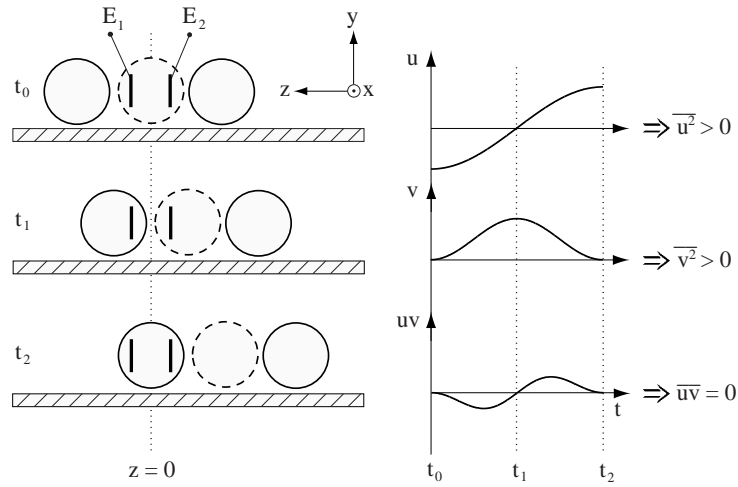


Figure 3: Illustration of the moving high- and low-velocity streak in relation to the stationary X-probe. By assuming a positive wall-normal velocity component ( $E_1 > E_2$ ) the effect of the moving streaks on the Reynolds stresses is illustrated.

the streamwise component. However, to compensate for the background noise the  $u_{rms}$ -profile is corrected by subtracting an appropriate constant noise level which was chosen in order to fit the free stream values to the corresponding HWA-data.

## Results and discussion

Due to the presence of the wall the  $V$ -fluctuations in the free stream are damped when approaching the wall (see e.g. Hunt & Graham 1978). In figure 1b and 2b the damping can be seen also outside the boundary layer edge (which is located at  $y/\delta^* \approx 3$ ). Inside the boundary layer both the HWA and the LDV predict a large amplitude peak in the  $u_{rms}$ , and after the correction of the LDV-data to obtain a correct rms-level in the free stream both methods showed a maximum amplitude inside the boundary layer of approximately 4.5% (see figure 2a).

When comparing the  $v_{rms}$ -profiles the two measurements agree quite well in the damped region outside the boundary layer edge, but closer to the wall it is evident that the HWA-data generates a virtual maximum. The LDV-data is damped all the way down to the wall, which is in agreement with DNS-data (see e.g. Rai & Moin 1991 and Jacobs & Durbin 2001). It is also interesting to note that the relative magnitude of the erroneous peak in  $v_{rms}$  is larger in figure 2b than in 1b, i.e. the larger probe size in the new measurements results in larger errors.

The explanation to the virtual maximum in  $v_{rms}$  obtained with HWA can be understood if one considers that the disturbances in the pseudo-laminar boundary layer is dominated by longitudinal streaks with high and low streamwise velocity. This is illustrated with solid and dashed circles in figure 3. Since the  $V$ -component is obtained from the voltage difference between the two wires, a spanwise gradient in  $U$  will be erroneously detected as a wall-normal component. Depending on the sign of  $\partial U/\partial z$  and the direction of the movement of the streaks four different scenarios are possible of which one is shown in figure 3. The outcome of the other three is similar. It can be seen that the off diagonal element  $\overline{uv}$  in the Reynolds stress tensor becomes zero, while there are non-zero contributions to both  $u_{rms}$  and  $v_{rms}$ . Since in this simplified illustration both  $v_{rms}$  and  $\overline{uv}$  should be zero, it is clear that the error due to unsteady spanwise gradients primarily will appear in measurements of the wall-normal fluctuation level.

In the present study only laminar boundary layers subjected to FST have been considered, which is a case where the described error becomes clearly visible due to the very small level of wall-normal fluctuations. However, the same gradient effect will distort measurements also in other cases. For example in the near-wall region of a turbulent boundary layer  $u$ -velocity streaks are common, and  $v_{rms}$ -profiles obtained with HWA in this region are certainly overestimated. The smaller spanwise scales in the turbulent boundary layer as compared to the pseudo-laminar one further enhances the effect of the measurement error.

## Acknowledgments

The authors would like to thank Prof. Henrik Alfredsson for valuable comments and ideas.

## References

- Andersson, P., Berggren, M., and Henningson, D.S. (1999). Optimal disturbances and bypass transition in boundary layers. *Phys. Fluids*, 11:134-150.
- Arnal, D., and Juillen, J. C. (1978). Contribution expérimentale à l'étude de la receptivité d'une couche limite laminaire, à la turbulence de l'écoulement general. ONERA Rapport Technique No 1/5018 AYD.
- Cutler, A. D. and Bradshaw, P. (1991). A crossed hot-wire technique for complex turbulent flows. *Exp. Fluids*, 12:17-22.
- Hunt, J. C. R. and Graham, J. M. R. (1978). Free-stream turbulence near plane boundaries. *J. Fluid Mech.*, 84:209-235.
- Jacobs, R. G. and Durbin, P. A. (2001). Simulations of bypass transition. *J. Fluid Mech.*, 428:185-212.

- Matsubara, M. and Alfredsson P. H. (2001). Disturbance growth in boundary layers subjected to free-stream turbulence. *J. Fluid Mech.*, 430:149-168.
- Rai, M. M. and Moin, P. (1991). Direct numerical simulation of transition and turbulence in a spatially evolving boundary layer. AIAA-91-1607-CP.
- Roach, P. E. and Brierley, D. H. (1992), The influence of a turbulent freestream on zero pressure gradient transitional boundary layer development. Part I: Test cases T3A and T3B. In *Numerical Simulation of Unsteady Flows and Transition to Turbulence*, pages 319-347. Cambridge Univ. Press.
- Talamelli, A., Westin, K. J. A., and Alfredsson, P. H. (2000). An experimental investigation of the response of hot-wire X-probes in shear flows. *Exp. Fluids*, 28:425-435.
- Voke, P. R. and Yang, Z. (1995). Numerical study o bypass transition. *Phys. Fluids*, 7(9):2256-2264.
- Westin, K. J. A. (1997). *Laminar-turbulent boundary layer transition influenced by free stream turbulence*. PhD thesis, Dept. of Mechanics, The Royal Institute of Technology, Stockholm, Sweden.
- Westin, K. J. A., Boiko, A. V., Klingmann, B. G. B., Kozlov, V. V., and Alfredsson, P. H. (1994). Experiments in a boundary layer subjected to freestream turbulence. Part I. Boundary layer structure and receptivity. *J. Fluid Mech.*, 281:193-218.